ABSTRACT

Title of Dissertation:	QUANTITATIVE STUDY OF LONGITUDINAL RELAXATION (T_1) CONTRAST MECHANISMS IN BRAIN MRI
	Xu Jiang, Doctor of Philosophy, 2017
Dissertation directed by:	Professor, Steven M. Anlage, Department of Physics, University of Maryland-College Park Principle Investigator, Jeff H. Duyn, National Institutes of Health Staff Scientist, Peter van Gelderen, National Institutes of Health

Longitudinal relaxation (T_1) contrast in MRI is important for studying brain morphology and is widely used in clinical applications. Although MRI only detects signals from water hydrogen (^{1}H) protons (WPs), T_1 contrast is known to be influenced by other species of ^{1}H protons, including those in macromolecules (MPs), such as lipids and proteins, through magnetization transfer (MT) between WPs and MPs. This complicates the use and quantification of T_1 contrast for studying the underlying tissue composition and the physiology of the brain.

MT contributes to T_1 contrast to an extent that is generally dependent on MT kinetics, as well as the concentration and NMR spectral properties of MPs. However, the MP spectral properties and MT kinetics are both difficult to measure directly, as the signal from MPs is generally invisible to MRI. Therefore, to investigate MT kinetics and further quantify T_1 contrast, we first developed a reliable way to

indirectly measure the MP fraction and their exchange rate with WPs, with minimal dependence on the spectral properties of MPs. For this purpose, we used brief, high-power radiofrequency (RF) NMR excitation pulses to almost completely saturate the magnetization of MPs. Based on this, both MT kinetics and the contribution of MPs to T_1 contrast through MT were studied. The thus obtained knowledge allowed us to subsequently infer the spectral properties of MPs by applying low-power, frequency-selective off-resonance RF pulses and measuring the offset-frequency dependent effect of MPs on the WP MRI signal. A two-pool exchange model was used in both cases to account for direct effects of the RF pulse on WP magnetization.

Consistent with earlier works using MRI at low-field and post-mortem analysis of brain tissue, our novel measurement approach found that MPs constitute an up to 27% fraction of the total ^{1}H protons in human brain white matter, and their spectrum follows a super-Lorentzian line with a T_2 of 9.6±0.6 μs and a resonance frequency centered at -2.58±0.05 ppm, at 7 T. T_1 contrast was found to be dominated by MP fraction, with iron only modestly contributing even in the iron-rich regions of brain.

QUANTITATIVE STUDY OF LONGITUDINAL RELAXATION (T_1) CONTRAST MECHANISMS IN BRAIN MRI

by

Xu Jiang

Dissertation submitted to the Faculty of the Graduate School of the
University of Maryland, College Park, in partial fulfillment
of the requirements for the degree of
Doctor of Philosophy
2017

Advisory Committee:
Professor Steven M. Anlage, Chair
Professor Yang Tao, Dean's Representative
Dr. Jeff H. Duyn
Dr. Peter van Gelderen
Professor Wolfgang Losert
Professor Rajarshi Roy

Acknowledgements

I would like to thank my two research advisors, Dr. Jeff H. Duyn and Dr. Peter van Gelderen, and my academic advisor Prof. Steven M. Anlage, for their generous support and extensive help, throughout the journey of my doctoral study.

Contribution

Chapter 2: This work was published in Magnetic Resonance in Medicine, under the title of "Rapid measurement of brain macromolecular proton fraction with transient saturation transfer MRI" (1). Xu Jiang performed the measurements with Dr. Peter van Gelderen. Xu Jiang is the second author of this paper and has secondary contribution in this work.

Chapter 3: This work was published in Neuroimage, under the title of "Effects of magnetization transfer on T_1 contrast in human brain white matter" (2). Xu Jiang performed the measurements with Dr. Peter van Gelderen. Xu Jiang is the second author of this paper and has secondary contribution in this work.

Chapter 4: Xu Jiang performed the measurements together with Dr. Xiaozhen Li and Dr. Emily Leibovitch, did the data analysis and data interpretation, and wrote most of the manuscript, which was accepted as a conference abstract in ISMRM 23th Annual Meeting & Exhibition, under the title of "Study of Bound Proton T_2 and Magnetization Transfer using Pulsed MT" (3). Xu Jiang is the first author and has primary contribution in this work.

Chapter 5: Xu Jiang performed the measurements, did the data analysis and data interpretation, and wrote most of the manuscript, which was accepted as a conference abstract in ISMRM 24th Annual Meeting & Exhibition, under the title of "Measurement of the Resonance Frequency of Macromolecular Protons in Brain" (4). Xu Jiang is the first author and has primary contribution in this work.

Chapter 6: Xu Jiang performed the measurements with Dr. Peter van Gelderen, did the data analysis and data interpretation, and wrote most of the manuscript, which is

accepted for publication in Magnetic Resonance in Medicine, under the title of "Spectral characteristics of semi-solid protons in human brain white matter at 7 T". Xu Jiang is the first author and has primary contribution in this work.

Chapter 7: Xu Jiang performed the measurements with Dr. Peter van Gelderen, did the data analysis and data interpretation, and wrote most of the manuscript, which was submitted as a conference abstract to ISMRM 25th Annual Meeting & Exhibition, under the title of "Combination of MT and R_2^* measurements to distinguish between contributions of semisolids and iron to R_1". Xu Jiang is the first author and has primary contribution in this work.

Table of Contents

Appendix: Curriculum Vitae

List of Figures

(grey band), they differentially affect the short T_2 MP (blue band). **B**: For MP (T_2 = 70μs), magnetization (black) after a composite inversion pulse and the latter's energy (red) depend strongly on pulse duration **C:** Effect of MT pulse on M as a function of T_2. Nearly complete saturation (M~0) is achieved for MP, while WPs are minimally affected. **D**: Calculated MP (dashed lines) and WP (solid lines) magnetization following inversion, as function of (TI) time, for two extreme cases: no MP saturation (green), and complete MP saturation (blue). Parameters for this simulation were taken from mean 7 T values of Table 3.2. Perfect WP inversion was assumed.. 66

List of Abbreviations

CEST	chemical exchange saturation transfer
CSF	cerebrospinal fluid
CT	X-ray computed tomography
EPI	echo planar imaging
FS	fractional saturation
GM	grey matter
IR	inversion recovery
IRB	internal review board
MGRE	multi gradient echo
MPs	macromolecular protons
MRI	magnetic resonance imaging
MT	magnetization transfer
MTR	magnetization transfer ratio
NMR	nuclear magnetic resonance
PD	proton density
PET	positron emission tomography
$R_1 (=1/ T_1)$	longitudinal relaxation rate constant
$R_2 (=1/ T_2)$	transverse relaxation rate constant
RF	radiofrequency
SAR	specific absorption rate
SD	standard deviation
SL	super-Lorentzian
SR	saturation reconvery
T_1	longitudinal relaxation time constant
T_2	transverse relaxation time constant
TR	repetition time
WM	white matter
WPs	water protons

Chapter 0: Basics of magnetic resonance imaging (MRI) and relaxation

Magnetic resonance imaging (MRI) is widely used in both scientific research and clinical applications for *in vivo* brain imaging. In the past 40 years (5), tremendous achievements have been made on the use of MRI for measurement of brain physiological parameters, detection of brain functional activity, diagnosis of various brain diseases, and other applications. Compared to other *in vivo* imaging modalities, such as X-ray computed tomography (CT) and positron emission tomography (PET), MRI provides superior contrast between soft tissues, such as grey matter (GM) and white matter (WM). (In MRI, the contrast between two regions is defined as their difference in image intensity averaged within each region, divided by the sum of their respective averaged intensities.) However, previous studies have shown that a certain type of MRI contrast often contains contribution from multiple factors, such as the longitudinal relaxation time constant (T_1), the transverse relaxation time constant (T_2), and hydrogen (^{1}H) proton density. This makes it challenging to use MRI for studying the brain physiology and tissue composition. The purpose of this dissertation is to quantitatively understand T_1 relaxation, which is important for brain research and clinical diagnosis (to be discussed in detail in Chapter 1).

Chapter 0 begins by introducing the principles of MRI, in Section 0.1. The origin of intrinsic T_1 relaxation in MRI is discussed in Section 0.2. Section 0.3 compares MRI with CT and PET for *in vivo* brain imaging.

0 .1 *Principles of MRI*

The principle of MRI is based on manipulation and measurement of the magnetic moments of ^{1}H proton nuclear spins, which are abundant in human brain, and can be polarized in a strong magnetic field $\vec{B_0} \equiv B_0\hat{z}$ ($\vec{B_0}$ is assumed to be in the $\hat{z}$ direction). The polarization of the ^{1}H proton spins creates an ensemble magnetization $\vec{M}$, which is aligned with the orientation of $\vec{B_0}$ in equilibrium. When $\vec{M}$ is perturbed (to be discussed later in this section) from its equilibrium, there will be a net torque $\vec{N} = \vec{M} \times \vec{B_0}$ applied on $\vec{M}$ and it will undergo precession, with a Larmor frequency of $\omega_0 = \gamma B_0$, as shown in Fig. 0.1. Over time, the longitudinal component of $\vec{M}$ relaxes to its equilibrium, which is referred to as longitudinal (T_1) relaxation, and the transverse component of $\vec{M}$ relaxes to 0, which is referred to as transverse (T_2) relaxation. Taking into account the longitudinal and transverse relaxation, the equation of motion for the ensemble magnetization $\vec{M}$ can be expressed as follows:

$$\frac{d\vec{M}}{dt} = \gamma \, \vec{M} \times \vec{B_0} + \frac{(M_0 - M_z)\hat{z}}{T_1} - \frac{M_x\hat{x} + M_y\hat{y}}{T_2} \qquad (\,0.1\,)$$

which is referred to as the Bloch equation. The term with T_1 is the spin lattice (or longitudinal) relaxation (to be discussed in detail in Section 0.2), the term with T_2 is the spin spin (or transverse) relaxation, M_0 is the magnetization at equilibrium, and $\vec{M} = M_x\hat{x} + M_y\hat{y} + M_z\hat{z}$. The transverse relaxation is induced by the local variations in $\vec{B_0}$ across the spin population, leading to different precession frequencies for different spins. Over time the vector sum of the transverse magnetization of the spin population decays, which is assumed to have an exponential form as shown in Eqs. 0.2 & 0.3, with a time constant of T_2. T_2 relaxation will be discussed in detail later in this section.
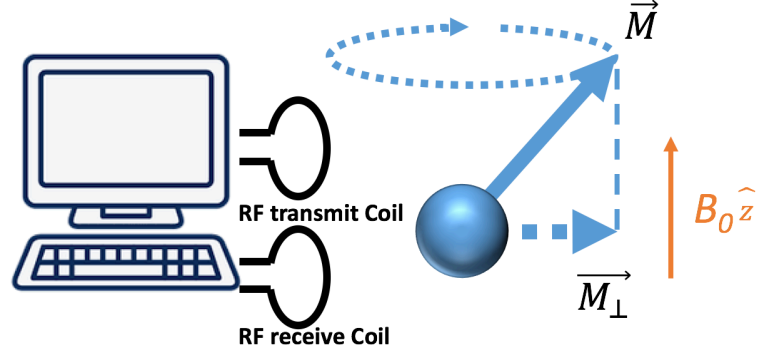
Figure 0.1 Schematic representation of the MRI process. Precession of the magnetization $\vec{M}$ in a magnetic field $B_0\hat{z}$; the magnetization $\vec{M}$ is perturbed from its equilibrium, by RF pulses generated using an RF transmit coil; MRI measurement is performed by measuring the change of magnetic flux induced by the rotation of the transverse component of $\vec{M}$, $\vec{M_\perp}$, using an RF receive coil; the computer controls the hardware, including the RF transmit coil and RF receive coil.

Solving Eq. 0.1 gives:

$$M_x(t) = e^{-t/T_2}(M_x(0)\cos\omega_0 t + M_y(0)\sin\omega_0 t) \qquad (0.2)$$

$$M_y(t) = e^{-t/T_2}(M_y(0)\cos\omega_0 t - M_x(0)\sin\omega_0 t) \qquad (0.3)$$

$$M_z(t) = M_z(0)e^{-t/T_1} + M_0(1 - e^{-t/T_1}) \qquad (0.4)$$

In an MRI measurement, an RF pulse $\vec{B_1}(t) = B_1(\cos\omega_0 t\,\hat{x} - \sin\omega_0 t\,\hat{y})$ is

generated using an RF transmit coil and perturbs $\vec{M}$ from its equilibrium (Fig. 0.1). This

effect can be understood in a rotating reference frame, with an angular velocity of $-\omega_0\hat{z}$.

The unit vectors $\hat{x}'$, $\hat{y}'$ and $\hat{z}'$ along the x'-, y'- and z'-axis of the rotating frame can be

written in terms of the unit vectors $\hat{x}$, $\hat{y}$ and $\hat{z}$ in the inertial (laboratory) frame:

$$\hat{x}' = \cos\omega_0 t\,\hat{x} - \sin\omega_0 t\,\hat{y} \qquad (0.5)$$

$$\hat{y}' = \sin\omega_0 t\,\hat{x} + \cos\omega_0 t\,\hat{y} \qquad (0.6)$$

$$\hat{z}' = \hat{z} \qquad (0.7)$$

The time derivative of any vector $\vec{A}'$ in the rotating frame can be written in terms

of its corresponding value in the inertial (laboratory) frame $\vec{A}$, as following:

3

$$\frac{d\vec{A}'}{dt} = \frac{d\vec{A}}{dt} + \omega_0 \hat{z} \times \vec{A} \qquad (0.8)$$

With the presence of the RF pulse, the torque on $\vec{M}$ is $\vec{M} \times (\vec{B_0} + \vec{B_1}(t)) = \vec{M} \times (\vec{B_0} + B_1 \hat{x}')$, based on Eq. 0.5. In the rotating reference frame, according to Eq. 0.8 and the precession term in Eq. 0.1, the equation of precession for $\vec{M}'$ can be written as:

$$\frac{d\vec{M}'}{dt} = \frac{d\vec{M}}{dt} + \omega_0 \hat{z} \times \vec{M} = \gamma \vec{M}' \times B_1 \hat{x}' \qquad (0.9)$$

As can be seen from Eq. 0.9 (similar to the precession term in Eq. 0.1), $\vec{M}'$ undergoes precession, with an angular velocity of $\omega_1 \hat{x}' \equiv \gamma B_1 \hat{x}'$, under the influence of the RF pulse $B_1 \hat{x}'$, in the rotating reference frame. The angle of rotation for $\vec{M}'$, $\Delta\theta$, is determined by the RF pulse amplitude B_1 and pulse duration t_d:

$$\Delta\theta = \gamma B_1 t_d = \omega_1 t_d \qquad (0.10)$$

The effect of the RF pulse on $\vec{M}'$ is illustrated in Fig. 0.2.
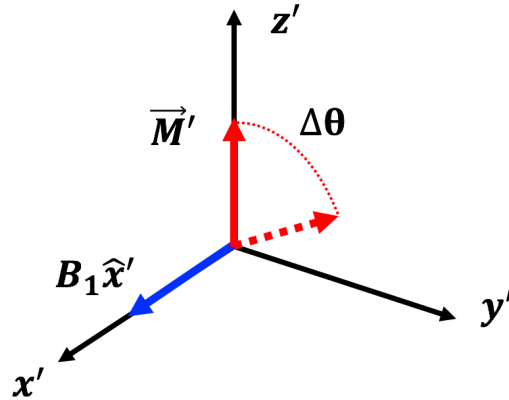
Figure 0.2 Precession of magnetization $\vec{M}'$ under the influence of an RF pulse $B_1 \hat{x}'$, in the rotating reference frame; the angle of rotation for $\vec{M}'$, $\Delta\theta$, is determined by the RF pulse amplitude B_1 and pulse duration t_d, through Eq. 0.10.

As can be seen from Eq. 0.4, the longitudinal magnetization $M_z(t)$ relaxes exponentially back to M_0, with a rate of $R_1 = 1/T_1$. Fig. 0.3 shows the simulated recovery of the longitudinal magnetization $M_z(t)$, following an inversion of the

longitudinal magnetization (rotation of the equilibrium magnetization $M_0\hat{z}$ by 180^0 around $\hat{x}'$) using an RF pulse. By monitoring signal recovery of $M_z(t)$ at variable post-inversion delay time t, and fitting to Eq. 0.4, T_1 can then be determined.
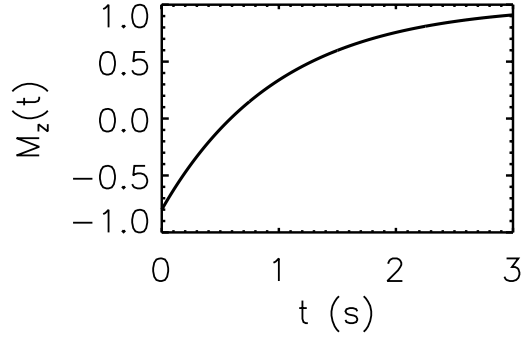
Figure 0.3 Simulated recovery of the longitudinal magnetization $M_z(t)$ following an inversion; $M_z(0)$ is assumed to be -0.8 and T_1 is assumed to be 1 s^{-1}.

Measurement of the MRI signal is performed by flipping the longitudinal magnetization into the transverse plane using RF pulses generated by an RF transmit coil, followed by measuring the change of magnetic flux induced by the rotation of the transverse component of $\vec{M}$, $\overrightarrow{M_\perp}$, using an RF receive coil, as shown in Fig. 0.1. However, the ^{1}H proton spins experience different local magnetic fields on top of the main magnetic field $B_0\hat{z}$, and thus have different Larmor frequencies. Therefore, their precessions will eventually be out of phase and their ensemble transverse magnetization $\overrightarrow{M_\perp}$ decays to zero, as illustrated in Fig. 0.4. T_2 is an important time constant, and its magnitude relative to the time scale of MRI measurements, which is on the order of milliseconds, determines if a certain species of ^{1}H protons is detectable in MRI. WP T_2 in brain is on the order of 10-100 ms, while for MPs it is on the order of 10-100 μs, due to their difference in magnetic environment. Therefore, MRI signals merely contain direct

contribution from WPs, and MPs are invisible in MRI and only contribute to MRI signals indirectly.
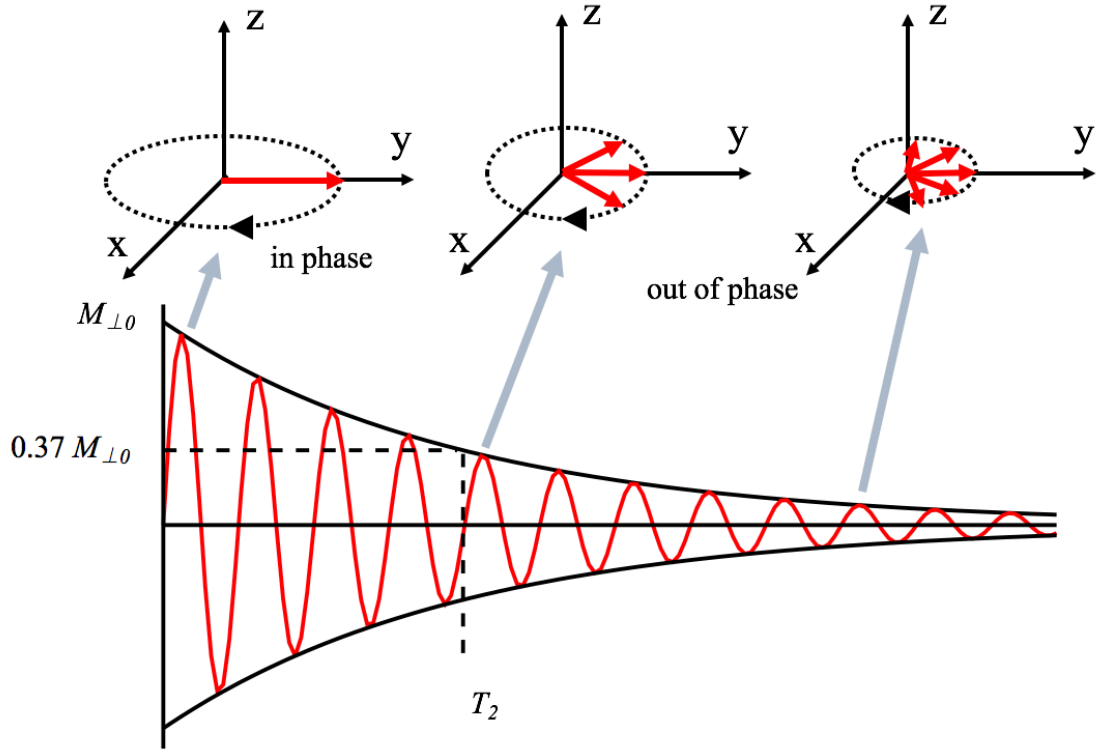
Figure 0.4 Illustration of T_2 relaxation. The red arrows in the top three sub-figures show that the spins are initially in phase and later become out of phase, and therefore the vector sum of their transverse magnetization decays to zero eventually (the black curve in the bottom sub-figure). The red curve shows the signal measured by RF coils, where the oscillation is induced by the precession of the magnetization.

The RF pulses used in MRI often have to be applied several times for an acquisition of an MRI image (refer to (6) for details of MRI image acquisition). In practice, the repetition time (TR) between the acquisition RF pulses is often shorter than T_1, as it is limited by the total available image acquisition time. In this case, following an acquisition RF pulse, instead of recovering back to its equilibrium M_0, $M_z(t)$ relaxes to $M_z(TR) = M_z(0)e^{-TR/T_1} + M_0(1 - e^{-TR/T_1})$ according to Eq. 0.4, for the following signal acquisition. Consequently, the acquired image contrast will depend on TR/T_1.

Therefore, T_1 relaxation has unintended effects on all MRI images acquired with finite TRs, and understanding T_1 is important for interpreting image contrast.

Besides T_1, other factors, such as ^{1}H proton density (PD) and T_2, may also have unintended effects on an MRI measurement. PD in a certain region of brain tissue determines the equilibrium magnetization, M_0, and thus influences the transverse magnetization $M_\perp$ (Fig. 0.1), which is the direct source of MRI signal. And T_2 may also have effects on $M_\perp$, especially when T_2 is comparable with the time scale of the image acquisition, as illustrated in Fig. 0.4. Therefore, an MRI image often contains contribution from multiple factors. For example, a T_1 relaxation image measured using magnetization-prepared rapid gradient-echo (MP-RAGE) sequence (7,8) also contains unintended contribution from PD, and therefore the measured image is often referred to as T_1 "weighted" MP-RAGE image.

0.2 The origin of the intrinsic T_1 relaxation in MRI

The longitudinal relaxation (T_1) of ^{1}H proton magnetization in a magnetic field can be understood on the basis of Boltzmann statistics and quantum mechanics. A ^{1}H proton, which possesses a spin of 1/2, undergoes Zeeman splitting in a magnetic field, B_0, and the two energy levels for quantum states $|\downarrow\rangle$ and $|\uparrow\rangle$ are $E_\downarrow = +\hbar\omega_0/2$ and $E_\uparrow = -\hbar\omega_0/2$ respectively, with $\omega_0 = \gamma B_0$ as the Larmor frequency and γ as the gyromagnetic ratio.

Besides the main magnetic field B_0, a spin also experiences additional magnetic field from its neighboring spins and atoms, which are referred to as the lattice in the following text. The effects of the lattice magnetic field can be represented by a small perturbation potential V. According to Fermi's golden rule # 2, the transition rate for a spin from initial quantum state $|i\rangle$ to final quantum state $|f\rangle$ is then

$$P_{fi} = \frac{2\pi}{\hbar} |\langle f|V|i\rangle|^2 \delta(E_f - E_i) \qquad (0.11)$$

Each transition of a spin from $|i\rangle$ to $|f\rangle$ induces the lattice to change its state from

$|i_l\rangle$ to $|f_l\rangle$, with the subscript l denoting a quantum state for the lattice. For simplicity,

we assume the lattice also has two quantum states $|-\rangle$ to $|+\rangle$. The energy difference

between $|i_l\rangle$ to $|f_l\rangle$ should be the same as the energy difference between $|f\rangle$ and $|i\rangle$,

according to the conservation of energy. Using s_+ and s_- to represent the occupation

numbers of states $|+\rangle$ and $|-\rangle$, with energy levels of E_+ and E_- respectively, we then

have $E_+ - E_- = E_\downarrow - E_\uparrow = \hbar\omega_0$. These two lattice states, $|+\rangle$ and $|-\rangle$, can be assumed

to be in equilibrium, since the relaxation within the lattice is faster than the relaxation

between a spin and the lattice (9,10), and therefore s_+ and s_- are two constants, related

by $s_+/s_- = \exp(-\hbar\omega_0/kT)$, according to the Boltzmann statistics. Thus, the rate of

change in the number of spins in states $|\downarrow\rangle$ and $|\uparrow\rangle$ can be expressed respectively as:

$$\frac{dN_\downarrow}{dt} = P_{\downarrow\uparrow}N_\uparrow s_- - P_{\uparrow\downarrow}N_\downarrow s_+ \qquad (0.12)$$

$$\frac{dN_\uparrow}{dt} = P_{\uparrow\downarrow}N_\downarrow s_+ - P_{\downarrow\uparrow}N_\uparrow s_- \qquad (0.13)$$

where N denotes the numbers of spins. Due to the symmetry between $|i\rangle$ and $|f\rangle$ in Eq.

0.11, it can be found that $P_{\downarrow\uparrow} = P_{\uparrow\downarrow}$, which is further redefined as P in the following text.

The rate of change of the net polarization $\Delta N = N_\uparrow - N_\downarrow$ can then be written as the

following equation:

$$\frac{d(\Delta N)}{dt} = PN(s_- - s_+) - P\Delta N(s_+ + s_-) \qquad (0.14)$$

where $N = N_\uparrow + N_\downarrow$ is the total number of spins. When the system is in equilibrium, the

left hand side of Eq. 0.14 equals zero, and the equilibrium net polarization is $(\Delta N)^{eq} =$

$N(s_- - s_+)/(s_+ + s_-)$. With T_1 defined as $1/(P(s_+ + s_-))$, Ep. 0.14 can be rewritten as:

$$\frac{d(\Delta N)}{dt} = \frac{(\Delta N)^{eq} - \Delta N}{T_1}$$ (0.15)

This equation is generally true, whether or not the system is in equilibrium ($\Delta N = (\Delta N)^{eq}$). Non-equilibrium ($\Delta N \neq (\Delta N)^{eq}$) can be created by irradiating photons with a common energy of $\hbar \omega_0$ to induce transition from $|\uparrow\rangle$ to $|\downarrow\rangle$. The photons correspond to the RF pulses with angular frequency of ω_0 classically, as discussed in Section 0.1. Eq. 0.15 explains the origin of the intrinsic T_1 relaxation, which applies to a uniform spin bath of ^{1}H protons. The typical value for intrinsic T_1 of water is ~1 s, and for macromolecules of brain tissue, it is on the order of hundreds of milliseconds (11,12), shorter than that of water. This difference is attributed to the stronger coupling between MPs in the semisolid macromolecules of brain tissue (12,13), than that of WPs in the water, which exhibit Brownian motion. In Section 1.2, we will further discuss the apparent T_1 relaxation when multiple species of ^{1}H protons are present.

0 .3 Comparison with X-ray computed tomography (CT) and positron emission tomography (PET)

Besides MRI, X-ray computed tomography (CT) and positron emission tomography (PET), are also widely used for *in vivo* brain imaging. Compared to CT (14,15), MRI provides better contrast between soft tissues, including WM and GM in brain. CT also induces a risk of cancer for patients, because of the exposure to the higher energy of ionizing radiation. PET has high specificity to the injected radiotracer (16,17) , which can specifically label a physiological process, such as glucose metabolism, receptor binding potential, amino acid transport, and protein synthesis (16,18–21). However, PET scans usually have lower resolution than CT and MRI, and due to their

specificity only to the radiotracers, they often lose anatomical contrast (22), providing

poor distinction between WM and GM.

Chapter 1: Longitudinal relaxation (T_1) contrast in brain MRI and toward quantitative understanding of the underlying mechanisms

This chapter provides an overview on the previous understanding of T_1 contrast in brain MRI and introduces our approach to quantitatively study the T_1 contrast mechanisms. The first section reviews the significance and previous studies of T_1 contrast and magnetization transfer (MT) associated with macromolecular ^{1}H protons (MPs). Section 1.2 explains the needs for studying the contribution of MT to T_1 contrast, through a two-pool exchange model. The last section summarizes this dissertation and our approaches to quantifying MT and the T_1 contrast mechanisms in brain MRI.

1 .1 Overview of the significance and previous studies of longitudinal relaxation (T_1) contrast and MT in brain MRI

T_1, as the relaxation time constant of the longitudinal magnetization of ^{1}H protons in a magnetic field, is affected by the interactions of ^{1}H protons with their surroundings (6). T_1 contrast is one of the most important MRI contrasts for studying brain morphology, such as distinction and segmentation between different types of brain tissues, including grey matter (GM), white matter (WM), and cerebrospinal fluid (CSF). It is widely used for diagnosis in clinical applications (23–25). T_1 contrast is dependent on tissue composition, such as local concentration of proteins, lipids, and water, and their exchange of magnetization, through magnetic dipolar coupling and chemical exchange (26,27). In addition, paramagnetic and ferromagnetic molecules can contribute to longitudinal relaxation as well, including endogenous (intrinsic) iron and deoxyhemoglobin (28–30),

and exogenous (injected) contrast enhancement agents, such as Gadolinium diethylenetriaminepentacetate (Gd-DTPA) (31) and Feridex (32).

The distinct contrast of T_1 relaxation between GM and WM has been attributed to their differing content of myelin (12,13,30,33), which is a laminated membrane structure surrounding the axon of a neuron (34) and is primarily composed of macromolecules (35), including proteins and lipids. In the brain of a healthy adult, macromolecules contribute up to 30% of the total ^{1}H protons, in WM (36). In contrast, in GM, this fraction was reported to be around 16% (36). [1]H protons in these macromolecules (MPs), which are invisible in MRI due to their short T_2 (refer to Section 0.1 for an explanation), exhibit rapid T_1 relaxation (37–39) and can accelerate T_1 relaxation of MRI-visible ^{1}H protons from water (WPs), through magnetization transfer (MT), which refers to the exchange of magnetization between WPs and MPs. This occurs through magnetic dipolar coupling and chemical exchange (40–42). Therefore, study of T_1 relaxation may be helpful for determination of myelin content in brain (33) and also provide insight into MT (43–45).

It has been reported that MT between the two ^{1}H proton pools of water and macromolecules leads to the bi-exponential evolution of the longitudinal magnetization of WPs (46–49). This bi-exponential relaxation has been studied and used to quantify MP fraction and MT (45,50). However, due to the difficulty in direct detection of MPs in MRI owing to MPs' short T_2, the role of MPs in MT and their contribution to T_1 relaxation has been poorly understood and is usually approximated in MRI experiments. An often used assumption is that the magnetization of MPs is unaffected by the RF pulses (45,50), which is generally not correct.

Ignoring the bi-exponential recovery also leads to limited reproducibility of T_1 quantification, as has been reported in the literature (49,51–53). As a result, it limits the generalizability of using T_1 to quantify brain myelination, and affects the accuracy of tissue segmentation.

MT generally contributes to T_1 contrast to some extent, and this contribution differs by the different longitudinal magnetization levels of WPs and MPs created by RF pulses (54), which in many cases are sensitive to both the characteristics of the RF pulses and the spectral properties of WPs and MPs, including the lineshape, resonance frequency and T_2. The spectral properties are important, since they define the response of WPs and MPs to an RF pulse (26), and further affect the MT between WPs and MPs (see Section 1.2 for detailed discussion). Therefore, the spectral properties of MPs, including their lineshape, T_2, and resonance frequency, are critical for quantification of MP fraction, and further for estimation of how MPs contribute to the bi-exponential T_1 relaxation through MT. However the MP spectrum is difficult to measure directly, not only owing to MPs' extremely short T_2 as mentioned above, but also due to complications from MT, and chemical exchange saturation transfer (CEST) effects (27,55).

Most previous direct measurements of the MP spectrum have been performed with NMR spectrometers on *ex vivo* brain tissue samples and various membrane model systems, including myelin extracts and lecithin. These have shown that MPs have complex lineshapes with varying widths and resonance frequencies (35,56–60). However, due to the difference in physical environment between fixed and live tissues, the use of these results to interpret *in vivo* studies is difficult (61,62).

On the other hand, most *in vivo* conventional MT studies rely on an assumed lineshape for the MP spectrum, often a super-Lorentzian (SL) (Eq. 1.1) line centering on the water resonance (26,41,63), since data collected within the limited *in vivo* scanning time does not support fitting of a general lineshape.

$$g(F, T_2, A) = A \sqrt{\frac{2}{\pi}} \int_0^{\frac{\pi}{2}} \frac{T_2}{|3\cos^2\theta - 1|} exp\left(-2\left(\frac{2\pi F T_2}{3\cos^2\theta - 1}\right)^2\right) sin\theta d\theta \qquad (1.1)$$

Here, A is a scaling factor, F is the frequency of the applied RF pulse, and T_2 is the transverse relaxation time constant. The SL lineshape as shown in Eq. 1.1 is an integration of Gaussians over a uniform distribution of orientation θ, which is the angle between the lipid bilayer surface and the main magnetic field $\vec{B_0}$. The Gaussian is considered appropriate to describe the lineshape of MPs induced by the dipolar interaction of semisolid macromolecules (64).

However, this has been found to be inaccurate (65,66). For example, a lineshape that contains more parameters to fit than SL, has been reported to better represent MP spectrum than SL (65). In addition, some studies reported the MP spectrum to be shifted by about -3 ppm relative to the WP resonance (35,66–69), which, if ignored, can induce significant error for certain MT related applications, such as chemical exchange saturation transfer (CEST) (27,66) and arterial spin labeling technique (67,69).

Besides the contribution from MPs through MT, T_1 contrast was shown to be dependent on the concentration of iron, which is superparamagnetic (28–30). In iron-rich regions of brain, such as basal ganglia, iron concentration was found to account for 10-20% variation of T_1 (29), complicating the application of T_1 to study MP content and the quantification of MT between WPs and MPs.

This dissertation details our work on the quantitative study of MT between WPs and MPs, and to further quantify the relative contribution of MPs and iron to T_1 relaxation. The properties of MPs in brain MRI, including their relative fraction, exchange rate with WPs, T_2, lineshape, and resonance frequency, which proves difficult to measure as explained above, and have been less investigated in the past, are extensively studied in the works described in this dissertation.

1.2 *Towards understanding of the T_1 contrast mechanisms*

As discussed in the previous section, T_1 has been found to correlate with both MP and iron. However, quantification of respective roles of MP and iron in T_1 has proven difficult. Quantification is not only confounded by the exchange between MPs and WPs through MT, but also attributed to our limited knowledge of the properties of MPs, such as their relative fraction in tissue and their NMR spectral properties. MP fraction determines to what extent MPs contribute to MT and further to T_1. On the other hand, MP spectral properties define how MPs respond to an RF pulse. These complications necessitate a simulation-based approach that uses a simplified model to represent MT in brain tissue. The model should capture the kinetics of MT, in order to accurately establish the contributions from relevant parameters, such as the relative fractions of MPs and WPs, their respective intrinsic T_1's, and their MT exchange rates.

Previous studies have often assumed a simplified two-pool exchange model to interpret MT phenomena in biological tissue (70). Even with the presence of multiple species of ^{1}H protons, including WPs (71,72) and MPs (40,70), this two-pool exchange model can be used quite successfully for the quantification of MT in brain tissue. While four-pool models have also been investigated and may provide a more accurate

description of the complexity of exchange processes in brain tissue, including the myelin layers, interstitial water and axonal water (73–75), their precision is generally limited because of the increased number of unknown parameters.

The two pool model can be schematically shown in Fig. 1.1.
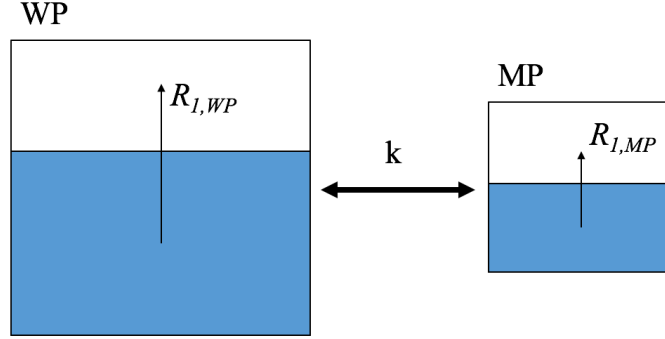
Figure 1.1 Two-pool exchange model for MT. WP and MP represent water ^{1}H proton and macromolecular ^{1}H proton pools respectively. R_1 is the intrinsic longitudinal relaxation rate, k is the exchange rate between the two pools; for each pool, the shaded area represents the current longitudinal magnetization $M(t)$ and the whole square (including the shaded and the blank areas) is the equilibrium longitudinal magnetization $M(\infty)$, as shown in Eqs. 1.2 & 1.3.

Taking into account of the exchange between the longitudinal magnetizations of WP and MP pools, the z-components of the Bloch equations (Eq. 0.1) for the two pools can be rewritten as:

$$\frac{dM_{WP}(t)}{dt} = R_{1,WP}\big(M_{WP}(\infty) - M_{WP}(t)\big) - (k/(1-f))M_{WP}(t) + (k/f)M_{MP}(t) \quad (1.2)$$

$$\frac{dM_{MP}(t)}{dt} = R_{1,MP}\big(M_{MP}(\infty) - M_{MP}(t)\big) - (k/f)M_{MP}(t) + (k/(1-f))M_{WP}(t) \quad (1.3)$$

In these equations, $M_{WP}(t)$ and $M_{MP}(t)$ are the longitudinal magnetizations of the two pools, $M_{WP}(\infty)$ and $M_{MP}(\infty)$ are their longitudinal magnetizations at equilibrium, $R_{1,WP}$ and $R_{1,MP}$ are their intrinsic longitudinal relaxation rates, $f = M_{MP}(\infty)/(M_{MP}(\infty) + M_{WP}(\infty))$ is the relative fraction of MPs, and k is the MT exchange rate constant. We further define $k_{WM} \equiv k/(1-f)$ and $k_{MW} \equiv k/f$ as the MT exchange rate

constants relative to WP and MP pool sizes respectively. f is related to k_{WM} and k_{MW} through the following equation:

$$(1-f)k_{WM} = fk_{MW} \qquad (1.4)$$

This relation ensures that when the magnetization levels on the two pools are the same, namely $M_{WP}(t)/(1-f) = M_{MP}(t)/f$, the exchange terms (last two terms) in each of Eqs. 1.2 & 1.3 equal zero. In this case, there is no net magnetization exchange between the two pools, in agreement with the assumption that the magnetization exchange is driven by the difference in magnetization levels between the two pools.

Rewriting Eqs. 1.2 & 1.3 in terms of fractional saturations, $FS_{WP}(t) = 1 - M_{WP}(t)/M_{WP}(\infty)$ and $FS_{MP}(t) = 1 - M_{MP}(t)/M_{MP}(\infty)$, gives the following equations:

$$\frac{dFS_{WP}(t)}{dt} = -(R_{1,WP} + k_{WM})FS_{WP}(t) + k_{WM}FS_{MP}(t) \qquad (1.5)$$

$$\frac{dFS_{MP}(t)}{dt} = -(R_{1,MP} + k_{MW})FS_{MP}(t) + k_{MW}FS_{WP}(t) \qquad (1.6)$$

These equations can be rewritten as:

$$\frac{d\overrightarrow{FS}(t)}{dt} = \boldsymbol{R} * \overrightarrow{FS}(t) \qquad (1.7)$$

with:

$$\overrightarrow{FS}(t) = [FS_{WP}(t), FS_{MP}(t)] \qquad (1.8)$$

$$\boldsymbol{R} = \begin{bmatrix} -(R_{1,WP} + k_{WM}) & k_{WM} \\ k_{MW} & -(R_{1,MP} + k_{MW}) \end{bmatrix} \qquad (1.9)$$

The two orthogonal modes for $\overrightarrow{FS}(t)$ can be found by solving for the eigenvalues, $-\lambda_{1,2}$, and the corresponding eigenvectors, $\overrightarrow{A_{1,2}}$, of $\boldsymbol{R}$:

$$2\lambda_{1,2} = R_{1,WP} + R_{1,MP} + k_{MW} + k_{WM} \pm \sqrt{(R_{1,MP} - R_{1,WP}+k_{MW} - k_{WM})^2 + 4k_{MW}k_{WM}}$$

$$(1.10)$$

$$\overrightarrow{A_{1,2}} = \left[\begin{array}{c} 1 \\ \frac{(-\lambda_{1,2}+k_{WM}+R_{1,WP})}{k_{WM}} \end{array} \right] =$$

$$\left[\begin{array}{c} 1 \\ \frac{-R_{1,WP}+R_{1,MP}-k_{MW}+k_{WM}\mp\sqrt{(R_{1,MP}-R_{1,WP}+k_{MW}-k_{WM})^2+4k_{MW}k_{WM}}}{2k_{WM}} \end{array} \right] \qquad (1.11)$$

Here, λ_1 and λ_2 are fast and slow rate constants of two orthogonal modes for the fractional saturations, which present the antiparallel and parallel modes respectively, as can be seen from the corresponding eigenvectors $\overrightarrow{A_1}$ (the two elements of vector $\overrightarrow{A_1}$ have opposite signs) and $\overrightarrow{A_2}$ (the two elements of vector $\overrightarrow{A_2}$ are both positive), in Eq. 1.11.

Therefore, FS_{WP} and FS_{MP} experience bi-exponential evolutions as follows (46–49,76):

$$FS_{WP}(t) = 1 - \frac{M_{WP}(t)}{M_{WP}(\infty)} = a_1 e^{-\lambda_1 t} + a_2 e^{-\lambda_2 t} \qquad (1.12)$$

$$FS_{MP}(t) = 1 - \frac{M_{MP}(t)}{M_{MP}(\infty)} = \frac{a_1(-\lambda_1+k_{WM}+R_{1,WP})}{k_{WM}} e^{-\lambda_1 t} + \frac{a_2(-\lambda_2+k_{WM}+R_{1,WP})}{k_{WM}} e^{-\lambda_2 t}$$

$$(1.13)$$

$$a_{1,2} = \pm \frac{FS_{WP}(0)\left(R_{1,WP}+k_{WM}-\lambda_{2,1}\right)-FS_{MP}(0)k_{WM}}{\lambda_1-\lambda_2} \qquad (1.14)$$

where a_1 and a_2 are the amplitudes of the fast and slow components, to be determined in experiments. $FS_{WP}(0)$ and $FS_{MP}(0)$ are the initial saturation effects created by the preparation RF pulse on the two pools, WPs and MPs.

By monitoring longitudinal magnetization recovery of WPs following an RF pulse, λ_1, λ_2, a_1, a_2 can be determined from fitting Eq. 1.12 to the fractional saturation of WPs $FS_{WP}(t)$, measured at variable delay time t. This leads to a problem of solving for 6 unknowns: $FS_{WP}(0)$, $FS_{MP}(0)$, $R_{1,MP}$, $R_{1,WP}$, k_{WM}, and k_{MW}, with only 4 equations shown in Eqs. 1.10 & 1.14. To resolve this problem, at least two constraints need to be added to the system of equations, and due to the invisibility of MPs in MRI, assumptions are

usually made on $FS_{MP}(0)$ and $R_{1,MP}$. Previous work has used simplifying assumptions of equating $FS_{MP}(0)$ to either 1 (77) or 0 (35,45,50). Common assumptions for $R_{1,MP}$ include taking it as 1 s^{-1} or the same as $R_{1,WP}$ (41,63,70). These assumptions are not necessarily true and can lead to the wrong estimation of MP properties, such as underestimating MP fraction by assuming a wrong $R_{1,MP}$ (11).

To obtain reliable solutions to Eqs. 1.10 & 1.14 for robust estimation of the two-pool exchange model parameters, is the common starting point for all the works reported in this dissertation. This two-pool exchange model is further extensively applied to understand the MT between WPs and MPs under various experimental conditions, for determination of the spectral properties of MPs.

1.3 Outline of the dissertation.

This dissertation presents our work on quantitative understanding of the roles of MPs and iron in the mechanisms of T_1 contrast in brain MRI, and on determination of the spectral properties of MPs *in vivo*, for understanding the mechanisms of other MT-related applications, such as CEST (42) and magnetization transfer ratio (MTR) (41).

As discussed in Section 1.2, to determine two-pool exchange model parameters, including the MP fraction, at least two assumptions have to be made. In Chapter 2, we compare four different combinations of assumptions on values of $R_{1,WP}$, $R_{1,MP}$, $FS_{MP}(0)$, and $FS_{WP}(0)$, and demonstrate methods for rapid *in vivo* measurement of MP fraction in human brain.

In Chapter 3, $R_{1,MP}$ and $FS_{MP}(0)$ are estimated, based on experiments using high B_1 amplitude RF pulses that almost completely saturate MPs, and are further used to determine MP fraction and the exchanges rates between WPs and MPs. It is demonstrated

19

that, the B_1 amplitude of RF pulses used in this study is high enough to achieve near complete saturation on MPs, such that this saturation effect is invariant for a broad range of the reported T_2 for MPs. Therefore, the MP fraction and their exchange rate with WPs are measured without having to make assumptions on T_2 or $FS_{MP}(0)$. The bi-exponential behavior of longitudinal magnetization recovery of WPs and the contribution of MPs to T_1 through MT, are further analyzed.

With the application of the methods for quantifying MP fraction and MT kinetics described in Chapters 2-3, the work in Chapter 4 further attempts to determine MP T_2 by measuring B_1 (amplitude of the RF pulse) dependence of MP saturation effects created by RF pulses, and compare this T_2 value with Bloch equation simulation. A large range of B_1 for the RF pulses (B_1 ranged from 500 to 2000 Hz (1 Hz converts to 0.0235 μT) in this study) is needed to simulate the B_1 dependence of saturation effects on MPs, for robust fitting of T_2. This is enabled by performing the measurements on a marmoset brain *in vivo*, in which case higher RF power deposition induced by high B_1 and longer scanning time are allowed, compared to *in vivo* human studies.

Our work in Chapter 5 measures the average resonance frequency and T_2 of MPs in a fixed marmoset brain *ex vivo*. The resonance frequency is measured by using off-resonance RF pulses to saturate the MPs and WPs differentially, and then determine the offset frequency dependence of saturation effects for both MPs and WPs, followed by super-Lorentzian fit to MPs and Lorentzian lineshapes fit to WPs to determine their respective resonance frequencies. MP fraction and MT kinetics are studied using methods described in Chapters 2-3. The respective saturation effects on the MPs and WPs by the off-resonance RF pulses are extracted based on the two-pool exchange model described

in Section 1.2. Further, MP T_2 is also measured following similar procedures to Chapter 4. Experiments are performed on a fixed marmoset brain sample, which allows for higher power deposition than *in vivo* studies, such that complete saturation on MPs can be achieved and $FS_{MP}(0)$ can be taken as 1.0 to simplify the fitting of the two-pool exchange model, as discussed in Section 1.2.

While Chapter 5 dealt with measuring the resonance frequency and T_2 for MPs, in Chapter 6, comprehensive study on MP spectral properties in performed *in vivo* on human brain, including determination of NMR lineshape, T_2 and resonance frequency, by using off-resonance low-power RF pulses to determine the offset frequency dependence of MP saturation effects, created by the off-resonance RF pulses. The use of low power for RF pulses ensures the saturation effect is linear with the intrinsic MP spectrum. The two-pool exchange model, as described in Section 1.2, are used to account for direct saturation effect on WPs, based on the MP fraction and exchange rates, measured using methods described in Chapters 2-3. The measured MP spectral properties can be used as predetermined knowledge in other applications of MT and CEST, to estimate the response of MPs to RF pulses.

In Chapter 7, we applied the methods described in Chapter 2-3 to measure $R_{1,WP}$ and correlate it with R_2^* as a surrogate of iron concentration, as well with putative iron concentrations derived from previously published histological measurements (78,79). $R_{1,WP}$ is found to linearly correlate with R_2^* and putative iron concentration respectively, consistent with previous report (33). Importantly, R_2^* can be used to reliably estimate $R_{1,WP}$ in iron-rich regions, to reduce the number of unknowns in Eqs. 1.10 & 1.14, and

facilitate the extraction of other two-pool exchange model parameters, including MP faction.

Finally, a summary of the thesis research is provided in Chapter 8.

Chapter 2: Rapid Measurement of Brain Macromolecular Proton Fraction with Transient Saturation Transfer MRI

As discussed in Chapter 1, the MRI-invisible MPs contribute to longitudinal relaxation of WPs, introducing a bi-exponentiality. By monitoring the magnetization level of WPs at variable delay times and fitting using a two-pool exchange model, the initial signal magnitude and relaxation rate constant for each of the bi-exponential components can be found, as described in Section 1.2. However, to further separate out the respective contribution from WPs and MPs, six parameters including the initial fractional saturation levels of MPs and WPs, their intrinsic longitudinal relaxation rates, and exchange rates, have to be determined, with only four equations available. Therefore, two parameters have to be fixed to allow for a solution. This chapter compares four different combinations of assumed values for the unknowns and propose methods for rapid measurement of relative fraction of MPs *in vivo* in human brain. This work is adapted from our manuscript published in *Magnetic Resonance in Medicine* (1).

2.1 *Significance and previous attempts to quantify MP fraction in vivo*

Although MRI almost exclusively measures the signal of water hydrogen protons (WPs), a substantial fraction ('f') of tissue hydrogen protons resides in molecules other than water, predominantly protein and lipid (here, for simplicity, these are categorically indicated by "macromolecular hydrogen protons" or MPs). While MPs are generally not directly visible because of their rapid transverse relaxation owing to restricted mobility, they can dramatically affect the MRI signal and the apparent longitudinal and transverse relaxation time constants (T_1 and T_2 respectively) through interaction with WPs.

23

In human brain, a relatively high fraction of MP ($f \sim 0.2\text{-}0.3$) is found in white matter (WM) (28,36,80–82), primarily because of its high content of myelin. Myelin, which is important for nerve conduction, is rich in proteins and lipids, and may contain up to 60% of MPs in white matter (35,59,83). Study of the effect of MPs on WP T_1 and T_2 relaxation therefore provides an opportunity to indirectly detect myelin loss (84).

One way to study myelin loss is through T_2 relaxation. In WM, T_2 relaxation has been shown to be multi-exponential, with the most rapid relaxation (shortest T_2) attributed to a pool of water trapped between the myelin layers, and strongly interacting with MPs in these layers (84,85). The size of this pool has been shown to correlate with brain myelin content (86). Similarly, the MPs in myelin are a strong contributor to T_1 relaxation (12), and in fact it has been argued that outside the iron-rich subcortical grey matter, f is the main determinant of T_1 (28,33,87,88). Thus, changes in f related to myelin loss may be sensitively detected by T_1-weighted techniques. Nevertheless, it should be realized that NMR relaxation processes are generally complex and that both changes in T_1 relaxation and T_2 relaxation may not be specific to changes in f. A further complication is a potential bias resulting from inter-compartmental exchange, which may lead to and underestimation of tissue myelin content (85).

Another approach to investigate variations or changes in brain myelination is by determining f through the classical MT experiment (89) in which radiofrequency (RF) irradiation is used to selectively reduce (saturate) the longitudinal magnetization of MPs and monitor the effect on the WP signal. This selectivity is based on the short T_2 of MPs, which has been found to be generally below 100 μs for proteins and lipids based on super-Lorentzian lineshapes (35).

To maximize the effect on WP saturation, most modern MT methods used for studying pathological changes in f in human brain use the so called "steady state approach", in which the MT effect is measured after long (relative to the T_1 of WP) continuous or repeated pulsed irradiation. However, while steady state approaches allow large saturation effects and provide good sensitivity, the loss of information about transient aspects of the MT process complicates interpretation and quantitative measurement of f, as the MT effects become strongly dependent of various parameters, including irradiation specifics, T_2 of the MP pool, and T_1 of both WP and MP pools. Mitigation of these issues is possible using so-called quantitative MT (qMT) techniques (54,63,90–93), which have shown promise in detecting myelin loss in multiple sclerosis and other neurological diseases (93–95). While rapid approaches may be possible (93), accurate qMT techniques are generally time-consuming and require collection of several reference datasets to mitigate confounds, such as variations in T_1 and RF amplitude.

An alternative to the steady-state approach, and a potentially faster way to measure f is to use of a "transient" MT approach which uses a single, brief irradiation pulse to differentially affect the longitudinal magnetization (M_z) of MPs and WPs (e.g. saturation of MP and inversion of WP magnetization) and monitors the equilibration process as a function of delay after the MT pulse. This approach was initially implemented on NMR spectrometers to study MT in tissue samples, and relied on direct measurement of signal from both the short T_2 MP pool and the longer T_2 WP pool (47,76,96–98). Combining this approach with a 2-pool model to fit to the MP and WP signal evolution allowed quantification of f as well as MT exchange rates. Subsequently, a number of studies has explored ways to use the transient MT approach to extract f without the need to detect the

MP signal, which would make the method amendable for use on clinical MRI scanners (44,74,91,99,100).

One of the outstanding issues with measurement of f using transient MT approaches is the difficulty in estimating MP T_1 (in the following referred to as $R_{1,MP}$, equal to the inverse of MP T_1), a parameter in the 2-pool model whose value significantly affects f. This is also an issue (possibly to a lesser extent) for steady state MT approaches, which typically assume $R_{1,MP}$ to be similar to $R_{1,WP}$ (around 1 s^{-1} in white matter). It has been pointed out however that actual values for $R_{1,MP}$ may be much higher, and that this would lead to an underestimation of f (11). To address this for the transient MT approach, we jointly analyzed MT and inversion recovery (IR) data from human brain using a 2-pool model of exchange and explored the validity of a number of simplifying assumptions. Based on this, we arrived at realistic estimates for $R_{1,MP}$ in human brain at 3 T and 7 T, allowing us to properly quantifying f from a transient MT experiment with a measurement time as short as 5 minutes.

2 .2 Two-pool exchange model and MRI measurements

Our method for quantifying f is based on the notion that in most brain regions outside the iron-rich sub-cortical grey matter (e.g. globus pallidus, caudate and red nuclei, and substantia nigra), longitudinal WP relaxation has a dominant contribution from MT with MP and that tissue contrast primarily results from variations in f (33). Thus, rather than assuming $R_{1,MP}$ and $R_{1,WP}$ to be equal, as has generally been done in the analysis of MT experiments, we allowed them to differ but assumed them to constant across the brain. We then performed pulsed, transient MT using a highly efficient MP saturation pulse, as well as inversion recovery (IR) to facilitate estimation of $R_{1,MP}$ and $R_{1,WP}$. For

this purpose MT and IR data were jointly analyzed with a 2-pool model of exchange, during which $R_{1,MP}$ and $R_{1,WP}$ values were determined that led to realistic values of MP saturation and allowed estimation of f. Additionally, we evaluated the feasibility of estimating f from MT data only by introducing additional constraints.

MRI Scanning

Experiments were performed on 3 T and 7 T Siemens MRI scanners (Erlangen, Germany; Skyra and Magnetom platforms respectively). Eleven subjects (6 female, ages 19-60, average 30) were scanned at both field strengths under an IRB-approved protocol to investigate the robustness in determining f. On 5 subjects at the 3 T only, a second scan was performed to assess test-retest reproducibility.
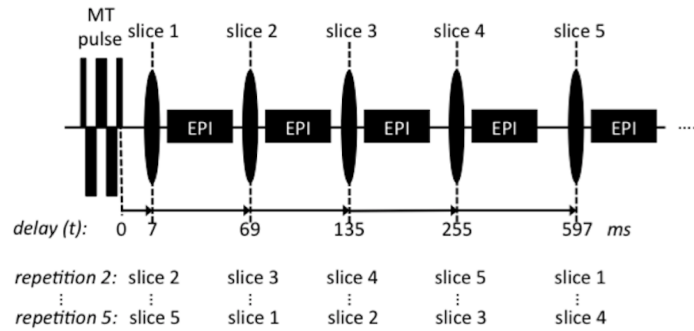
Figure 2.1 Image acquisition for the pulsed transient MT experiment. Five image slices are acquired at incrementally increasing delay times t after an MT pulse. By shifting the order of the slices in subsequent repetitions, all five delay times are sampled for each slice location.

Our transient MT experiment (Fig. 2.1) used a brief, T_2-selective composite RF saturation pulse (33,35,36) to saturate MP, after which multiple image slices at variable delay t were acquired with EPI. We first determined the appropriate RF pulse (in the following called "MT pulse") parameters to achieve optimal saturation characteristics, and then studied the feasibility to robustly extract f using a two-pool model of exchange.

27

The composite, phase modulated MT pulse had a constant B_1 amplitude of 19.6 μT and consisted of 17 sub-pulses of with nominal flip angles of 60°, -120°, 120°, -120° …, -120°, 60°. Its duration of 6 ms was sufficient to achieve a near optimal (about 90% of maximum, see below) saturation of MP, as judged from the delayed effect on the WP signal. This was based on initial experiments (n=6) that measured dependence of the saturation effect on increasing the MT pulse duration from 6 up to 11 ms (by adding -120°, 120° pulse segments). Numerical simulation of the effects of the 6 ms pulse (based on the Bloch equations), shown in Fig. 2.2, confirmed the efficient saturation of MPs assuming a Lorentzian lineshape with T_2 in the range of 20-400 μs. This range roughly covers the range of values reported in literature (35,58,59). A Lorentzian line shape was used in order to allow simulations using the time domain Bloch equations. In terms of the saturation effect of our MT pulse, the applied Lorentzian T_2 range is roughly equivalent to the T_2 range of 5-20 μs reported for super-Lorentzian MP lineshapes (40,54,60,63,70,101,102). At the same time, the pulse had an only minor (<10%) effect on T_2 species > 20 ms (WPs), as long as it was applied close enough (<500Hz) to resonance (Fig. 2.2). A simulation of the MP saturation as function of B_1 amplitude for a range of T_2 values in shown in Fig. 2.3a, demonstrating that MP saturation is nearly complete for the expected range of T_2 and B_1 values. At high B_1 amplitude, only minimal sensitivity of the saturation level to variations in B_1 amplitude is observed. This is further illustrated with the experimental data shown in Fig. 2.3b, confirming uniform MP saturation at high B_1.
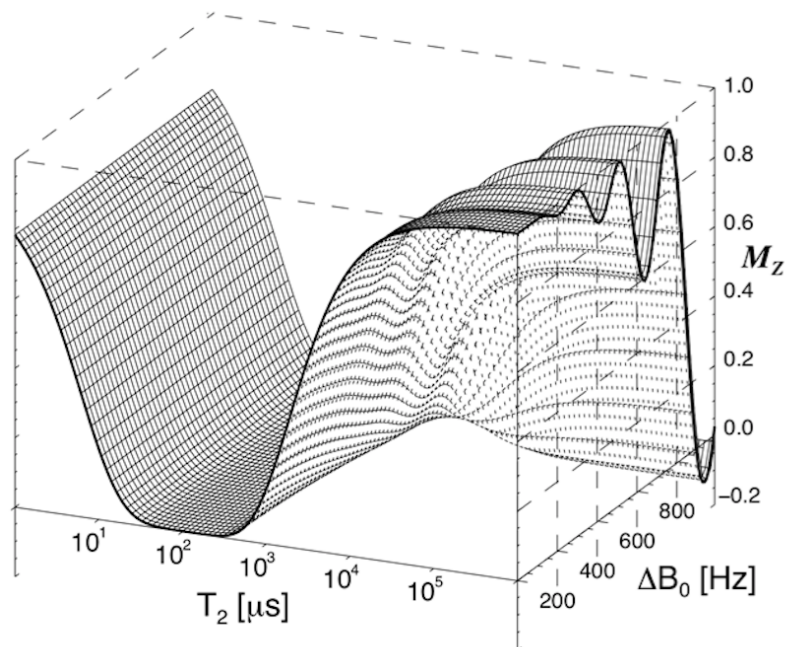
Figure 2.2 M_z after a 6 ms composite MT pulse, as function of T_2 and frequency offset (ΔB_0), based on simulation of the Bloch equations. The MT pulse effectively saturates spins with a T_2 in the range from 20 to 400 μs at all offset frequencies (for a Lorentzian lineshape). Long T_2 spins suffer only a small perturbation on resonance (< 5% for T_2 > 36 ms), with a larger effect for frequencies > 500 Hz.

The order of the five EPI slices acquired sequentially after each repetition of the MT pulse (Fig. 2.1) was cycled to allow time-efficient collection of the five delay times (103). Delay (t) values of 7, 69, 135, 255 and 597 ms were chosen to cover most of the saturation dynamics. EPI scan parameters were: echo spacing 0.77 ms, bandwidth 250 kHz, 45% ramp-sampling, matrix size 144x108, FOV 240x180 mm^2, SENSE rate 2, 2 mm slice thickness, 5.4 mm slice spacing (center to center), TE 30 ms (3 T) and 24 ms (7 T), TR = 3 s. The slice spacing was chosen relatively large to reduce potential MT effects of the excitation pulses (Fig. 2.9). Artifacts from scalp lipids were suppressed by acquiring every other repetition with a shifted EPI echo train (1.15 ms and 0.48 ms at 3 T and 7 T respectively), which resulted in a phase-inverted lipid signal. Addition of the two

29

repetitions allowed elimination of this lipid signal, assuming the T_2 is small compared to the applied shift in echo time. Twenty scan repetitions were performed at each slice location, taking a total scan time of 5 minutes. Four of the 20 repetitions were acquired without MT pulse to serve as reference signal.

IR scans were performed by replacing the MT pulse with a hyperbolic-secant inversion pulse (5.12 ms, 19.6 μT maximum B_1 amplitude, 830 Hz maximum frequency modulation, β = 1400 s^{-1} (104) with an adjustment of the amplitude to start at zero B_1). Delay times t (also called inversion times (TIs)) of 6, 69, 135, 282 and 1197 ms were used. The TR for these scans was 4 s, the number of repetitions was 18 for 3 T and 22 for 7 T. Again, four of the repetitions were acquired without inversion pulse to serve as reference signal to calculate the fractional saturation resulting from the MT (or IR) pulse.
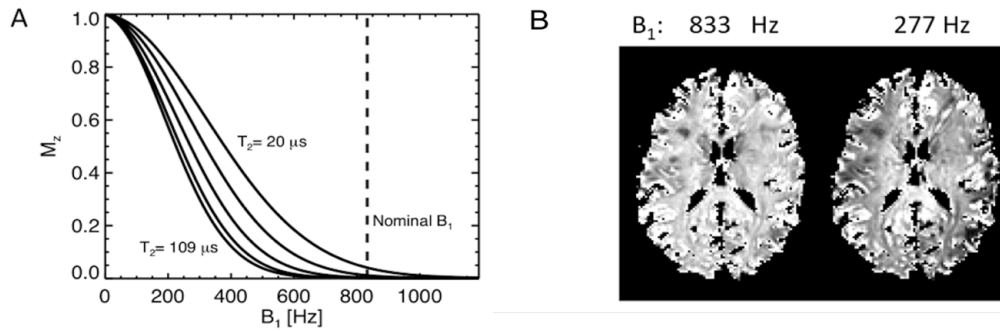
Figure 2.3 Robustness of transient MT approach to variations in B_1. A) Simulated MP saturation levels ($FS_{MP}(0)$) after a 6 ms MT pulse for (Lorentzian) MP T_2 values of 20, 32, 48, 72 and 109 μs. The curves for T_2's up to 400 μs fall between the 32 and 109 μs lines. The dashed line represents the nominal (brain-averaged) B_1 of 833 Hz used in the experiments. The plots show that MP magnetization is effectively saturated for a range of B_1 and T_2 values, reducing the sensitivity of the experiments to variations in B_1 amplitude. B) Experimental (7 T) demonstration of B_1 dependence of MP saturation. $FS_{MP}(0)$ was calculated with approach 1 from data at actual (833 Hz) B_1 and a strongly reduced (277 Hz) B_1. Incomplete MP saturation is only seen at strongly reduced B_1, in particular towards the edges of the brain where B_1 is lowest. The images were normalized to level in the SCC.

Two-pool exchange model

The extraction of f and other model parameters was based on fitting the delay-dependent signal to a two-pool model of MT (43,47,76,105). The same model was used for both preparation pulses (MT and IR pulses) albeit with different initial magnetization levels for the MP and WP pools. The calculations were based on the fractional saturation FS derived from the MT weighted signal S measured at delay t and reference signal S_{ref}:

$FS_{\text{WP}}(t) = \frac{S_{\text{ref}} - S(t)}{S_{\text{ref}}}$. For both WP and MP, $FS(t)$ can be written as the sum of 2 exponentials (47):

$$FS_{\text{WP}}(t) = ae^{-\lambda_1 t} + be^{-\lambda_2 t} \tag{2.1}$$

$$FS_{\text{MP}}(t) = a\left(1 - \frac{(\lambda_1 - R_{1,\text{WP}})}{k_{\text{MW}}}\frac{1-f}{f}\right)e^{-\lambda_1 t} + b(1 - \frac{(\lambda_2 - R_{1,\text{WP}})}{k_{\text{MW}}}\frac{1-f}{f})e^{-\lambda_2 t} \tag{2.2}$$

with:

$$2\lambda_{1,2}$$
$$= R_{1,\text{WP}} + R_{1,\text{MP}} + k_{\text{MW}}/(1-f)$$
$$\pm \sqrt{(R_{1,\text{MP}} - R_{1,\text{WP}})^2 + 2(R_{1,\text{MP}} - R_{1,\text{WP}})k_{\text{MW}}(1-2f)/(1-f) + k_{\text{MW}}^2/(1-f)^2}$$

$$\tag{2.3}$$

In these equations, $R_{1,MP}, R_{1,WP}$ are the longitudinal relaxation rates of both pools in the absence of exchange; k_{MW} and k_{WM} refer to the rates of change in FS_{MP} and FS_{WP} due to MT. These rates are the volume-fraction normalized equivalent of the often used cross-relaxation rate constant k, i.e. $k_{\text{MW}} = k/f$, and $k_{\text{WM}} = k/(1-f)$ (see e.g ref. (74)).

Both MT and IR data can be analyzed by this model, and Eq. 2.1 will fit with the same exponential rate constants (λ_1 and λ_2) but with different coefficients (a and b). After determining a, b, λ_1 and λ_2 from fitting of Eq. 2.1 to the experimental data, one can proceed with solving for $k_{\text{MW}}, f,$ $R_{1,MP}$ and $R_{1,WP}$ using Eq. 2.3, and the initial saturation levels $FS_{\text{WP}}(0)$ and $FS_{\text{MP}}(0)$ from Eqs. 2.1 and 2.2. This requires two additional pieces of information, as we have only four equations for 6 unknowns.

To solve this problem, and to investigate the possibility of omitting some of the data from the analysis in order to shorten the measurement protocol, four analysis approaches with different simplifying assumptions were evaluated. Briefly, four different combinations of parameters were fixed to (field specific) values common to all brain voxels: 1) $R_{1,MP}$ and $R_{1,WP}$; 2) $R_{1,MP}$ and $FS_{MP}(0)$; 3) $R_{1,MP}$, $R_{1,WP}$ and $FS_{MP}(0)$; 4) $R_{1,MP}$, $R_{1,WP}$, $FS_{MP}(0)$ and $FS_{WP}(0)$. The extracted values for k_{MW} and f were then compared between the four approaches, as well as their consistency across field strengths.

Global, fixed values for $R_{1,MP}$ and $R_{1,WP}$ under *approach 1* were estimated from joint analysis of MT and IR data. Fixing $R_{1,MP}$ and $R_{1,WP}$ was motivated by a previously proposed model of T_1 relaxation, in which MT between WP and MP is the dominant source of T_1 contrast (28,33,87,88). This model has been shown to accurately describe T_1 relaxation in most brain regions, perhaps with exception of iron-rich grey matter areas (e.g. globus pallidus, caudate and red nuclei, substantia nigra) (13). To estimate $R_{1,MP}$ and $R_{1,WP}$, first the MT and IR data were fitted jointly in every voxel with Eq. 2.1, resulting in one set of rate constants (λ_1 and λ_2) and two sets of amplitudes (a and b) for every voxel. Then $R_{1,MP}$ and $R_{1,WP}$ were varied to obtain reasonable values $FS_{MP}(0)$ values for both the MT and IR data. That is, for each combination of $R_{1,MP}$ and $R_{1,WP}$ values (within a realistic range), $FS_{MP}(0)$ for both the MT and IR experiments were calculated (together with corresponding values k_{MW} and f) in each voxel and the number of voxels with permissible values was used as a criterion to select $R_{1,MP}$ and $R_{1,WP}$ that best described the data. The permissible range was set as follows: $FS_{MP}(0)$ for both IR and MT experiments could not exceed 1.0 (i.e. complete saturation), while the value for IR data should be between 0.7 and 1.0 times that for MT (that is, the MP saturation after the inversion pulse

is somewhere between 70 and 100% of the saturation after the MT pulse). The data from all subjects was combined for this analysis, resulting in one global $R_{1,MP}$ and one global $R_{1,WP}$ value for each field strength.

Under *approach 2*, we used the fixed value for $R_{1,MP}$ found with approach 1, and as well as a fixed value for the $FS_{\mathrm{MP}}(0)$ for the MT experiment. Again, as in approach 1, one set of rate constants (λ_1 and λ_2) and two sets of amplitudes (a and b) extracted from the MT and IR data were used. The motivation of this approach was to evaluate the variation in $R_{1,WP}$, based on the notion that variation in $FS_{\mathrm{MP}}(0)$ for the MT experiment was constrained within a rather restricted range (between about 0.8 and 1.0, judged from simulations (see above) and experiments (see RESULTS, first paragraph).

Under *approach 3*, fixing both $R_{1,MP}$ and $R_{1,WP}$, as well as $FS_{\mathrm{MP}}(0)$ allowed omission of the IR data from the analysis. Now, only the MT data was fitted with Eq. 2.1, which represented only three degrees of freedom due to the dependence introduced between a, b, λ_1 and λ_2 by fixing the three parameters.

Finally, under *approach 4*, fixing a fourth parameter ($FS_{\mathrm{WP}}(0)$) obviated the need for measuring S_{ref} and reduced the 4 parameter model represented in Eq. 2.1 to a 3 parameter model:

$$S(t) = S_0 (1 - (a e^{-\lambda_1 t} + b e^{-\lambda_2 t})) \qquad (2.4)$$

where S_0 is a scaling factor for the signal level, λ_1 and λ_2 are defined as above, and two amplitudes a and b are now constants derived from the fixed average saturation levels of the two pools at $t = 0$ ($FS_{\mathrm{WP}}(0)$ and $FS_{\mathrm{MP}}(0)$). From the fitted parameters S_0, λ_1 and λ_2, both f and k_{MW} can be derived when applying Eq. 2.3 with fixed values for $R_{1,MP}$ and $R_{1,WP}$.

All fitting was performed on both a pixel-by-pixel basis and on the average signal in four region of interest (ROI): in white matter of the splenium of the corpus callosum (SCC), in grey matter in the globus pallidus (GP), the putamen (Put) and the head of the caudate nucleus (NC). The ROIs were manually selected directly on the EPI images using both the implicit T_2^* contrast and the T_1 contrast from the IR data. The SCC-ROI encompassed 33-86 voxels (average 61), the GP-ROI size was 18-110 (67), the Put-ROI 86-245 (150) and the NC-ROI 73-143 (103). Fitting was based on a simple and robust iterative grid search and refinement of the non-linear parameters to be optimized, in combination with linear least squares (LLS) optimization for the linear parameters (either a, b or S_0) (106). That is, for each choice of non-linear parameters, the linear parameters (amplitude factors) were estimated using LLS, and the residual was calculated. For each iteration, all combinations of parameters were tested in a search grid centered on the initial values. After selection of the best set (the one with the lowest residual), the step size was reduced to refine the search grid and next iteration was started using the current best fit as initial values. During joint fitting of MT and IR data, a single set of decay rates was used (λ_1 and λ_2) while the amplitudes (a, b) were allowed to be different to accommodate for the different saturation levels resulting from the MT and IR pulse. For both field strengths, average and standard deviation (SD) of the resulting parameter values was calculated. Results obtained from the ROI analysis were reported as averages and standard deviation over subjects. To investigate a potential bias related to magnetic field strength, differences of the results on the same subjects at the two field strengths were calculated for the SCC. The averages of the differences show a potential field related bias, while the SD of the differences reflects variability excluding inter subject

34

variations. Approach 1 was only used to analyze data from white matter, as the grey matter ROIs are known to be high in iron and as a result have an $R_{1,WP}$ substantially different from the global average. For the fixed $R_{1,WP}$ needed for approaches 3 and 4, the average over subjects of the values fitted in approach 2 were used instead.

To estimate the precision (reproducibility) of the fitted parameters under influence of noise in the input data, simulated noise was incrementally added to 3 T and 7 T model curves, based on the average parameters found for the SCC. The resulting simulated data were fitted for each noise realization and the SD of the extracted f and k_{MW} values were determined. The sensitivity of the fitted parameters to the variations in $R_{1,MP}$ and $FS_{MP}(0)$ is shown in Fig. 2.10. The plots were derived by recalculating the fitted parameters for a range of values for $R_{1,MP}$ and $FS_{MP}(0)$.

Image reconstruction and pre-processing

All image analysis was performed off-line using in-house IDL (Harris Geospatial Solutions, Boulder, CO, USA) based software and C code. The SENSE unfolding matrix, required for image reconstruction, was calculated from (multi–echo) GRE reference data acquired at the same slice position and resolution as the EPI data. This reference data were also used to derive field maps to calculate the geometric distortion corrections for the EPI. All resulting images in each scan session were spatially registered to the first volume to correct for in-plane motion. Through-plane motion was not corrected, as this proved difficult with the limited number of slices and large inter-slice gaps. Image registration included a fixed contrast adjustment to allow registration between reference, IR and MT data.

The addition of TE-shifted and non-shifted images for scalp lipid suppression was performed after calculating signal magnitude from the complex valued data; this proved sufficient and reduced problems with phase instabilities occasionally encountered at 7 T. However, for the IR scans, images acquired at the longest delay t required complex addition, due to the sign inversion of the longitudinal magnetization in some tissues. In this case, occasional manual phase adjustment was necessary. For earlier TIs, data were combined in magnitude mode and inverted (to reflect the negative polarity of the magnetization).

For both MT and reference data, signals were averaged over repetitions. In addition, for the reference signal (i.e. signal without inversion or MT), further averaging was performed over the acquisition with the different delay times to further improve image signal-to-noise ratio (SNR). Prior to multi-parametric fitting, voxels with a reference signal below 5% were eliminated, and signal intensities ($S(t)$) were converted to fractional saturation levels according to $FS_{\mathrm{WP}}(t) = \frac{S_{\mathrm{ref}} - S(t)}{S_{\mathrm{ref}}}$. With this normalization, MT and IR signals decay from 1 to 0 and 2 to 0 with increasing delay t respectively.

2 .3 Comparison of 4 different assumptions for model parameters extraction

At both 3 T and 7 T, saturation of MP with a single, 6 ms MT pulse led to a delay dependent reduction in WP signal. As expected, this reduction was strongest in white matter and reached a maximum of around 15-20% at a delay between 150 and 250 ms (see Figs. 2.4, 2.5). Fig. 2.4 shows the averages and SD of $FS_{\mathrm{WP}}(t)$ obtained for SCC at the two field strengths. The plots show high reproducibility over subjects, and furthermore indicate that the MT effect is more pronounced at 7 T. This is attributed to the slower T_1-relaxation at high field. Fig. 2.5 shows the difference in saturation level

between $t = 7$ ms and $t = 255$ ms, providing a model-free measure indicative of the MP fraction in human brain. Comparison of the fractional saturation levels ($FS_{WP}(0)$ in equations above) at $t = 255$ ms between the 6 ms and the 11 ms MT pulse (n=6) suggested effective saturation of macromolecular protons for the 6 ms pulse ($FS_{MP}(0) = 0.88 \pm 0.03$ and 0.93 ± 0.02 at 3 T and 7 T respectively, this assumed $FS_{MP}(0) = 1.0$ for the 11 ms pulse). These values were subsequently used for the extraction of k_{MW} and f with fitting approaches 2-4 (see Section 2.2).
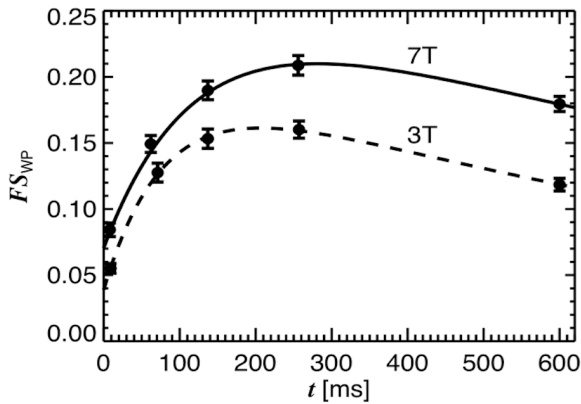
Figure 2.4 Fractional saturation of water protons (FS_{WP}) at delay time t after MT pulse, for both 3 T and 7 T experiments. FS_{WP} was averaged over ROI's in the splenium of the corpus callosum; error bars reflect the SD over subjects (n=11). Solid lines represent 2-pool model fit with subject-averaged parameters.
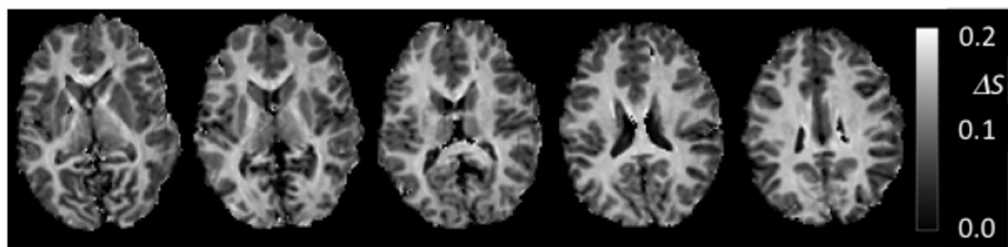
Figure 2.5 Fractional MT-related signal change ΔS (at 7 T) calculated from signal difference between images acquired at $t = 7$ ms and $t = 258$ ms ($\Delta S = \frac{S(t=7\text{ms})-S(t=258\text{ms})}{S(t=7\text{ms})}$).

Conjoint fitting of the IR and MT data using fitting approach 1 and 2 consistently produced maps of the four fitted parameters a, b, λ_1 and λ_2 as exemplified in Fig. 2.6. Estimation of appropriate $R_{1,MP}$ and $R_{1,WP}$ values common to all brain voxels with approach 1 resulted in estimates of 4.0 s^{-1} and 2.05 s^{-1} for $R_{1,MP}$ 3 T and 7 T, and 0.40 s^{-1} and 0.35 s^{-1} for $R_{1,WP}$ at 3 T and 7 T. These were the values used for approaches 3 and 4. At these values, the brain distribution of $FS_{WP}(0)$ derived from approach 1 (Fig. 2.7) showed minimal variation at both field strengths, with values ranging between 0.8 and 1.0, confirming the validity of fixing this parameter in approaches 3 and 4. Similarly, $R_{1,WP}$ (derived from approach 2) was rather uniform across the brain (Fig. 2.7), with exception of the subcortical grey matter regions.
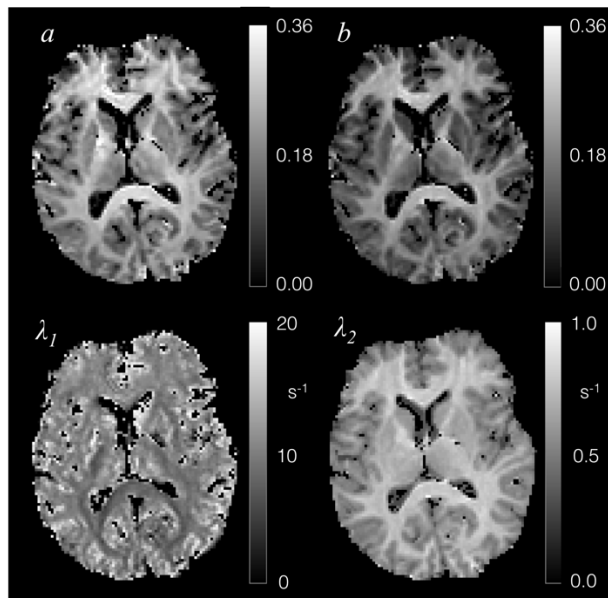
Figure 2.6 Single slice example of fitted parameters of the 2-pool model (Eq. 2.1) for 7 T data.

$FS_{MP}(0)$, approach 1 $R_{1,WP}$, approach 2
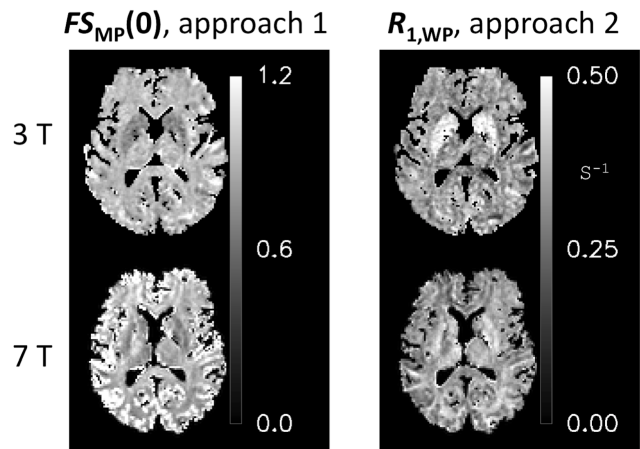
Figure 2.7   Variation in $FS_{MP}(0)$ and $R_{1,WP}$ over the brain, deduced with analysis approaches 1 and 2 respectively.

Approach: 1   2   3   4

f

k_{MW}
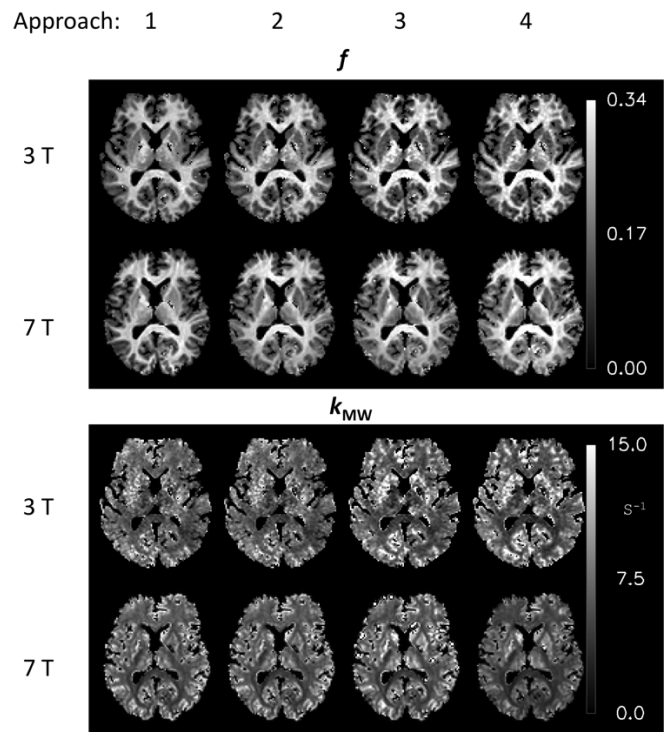
Figure 2.8 MP fraction f and exchange rate constant k_{MW} extracted with the four analysis approaches for 3 T and 7 T.
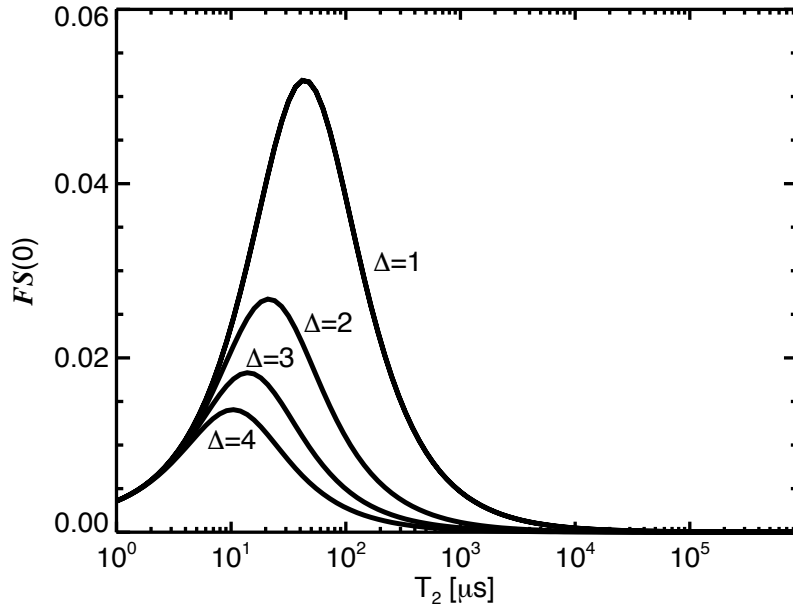
Figure 2.9 Simulation of effects of the slice excitation pulse on the MP saturation in neighboring slices as function of T_2. Considered are the four equally spaced slice excitations one to four slices removed from the measurement slice ($\Delta=1$ to 4). A small but significant effect is seen that is strongest in the nearest slice and diminishes quickly with increasing separation. The slices had a 5.4 mm center-to-center spacing, and a 2 mm thickness, resulting in 3.7 kHz frequency offset between slices. Some flexibility exists in minimizing these effects by judicially choosing slice selection parameters; in addition, since the same saturation effects are present in the reference scans without MT pulses, to first order approximation the small additional saturation from the excitation pulses will cancel out.

All approaches allowed reliable extraction of f and k_{MW} in most brain regions (Fig. 2.8, Table 2.1). Values for f were in the range of 5-30% across the brain, and in the range of 20-30% in white matter. Exchange rate constant k_{MW} varied in the range of 4-12 s^{-1}. Similar values for f were found between 3 T and 7 T, whereas values for k_{MW} were somewhat (5-20%) lower at 7 T (Table 2.1). Fit residuals (Table 2.1) indicate a somewhat more robust fit at 7 T; this is attributed to the lower $R_{I,MP}$ and consequently a larger available MT signal at the higher field strength. The average values for the WP exchange rate k_{WM} were 2.3 s^{-1} (3 T) and 1.9 s^{-1} (7 T). The SDs of the differences were similar to SDs of the data acquired at each field, suggesting the inter-subject variability is small

compared to the measurement induced SD and so these SDs are dominated by the reproducibility of the experiments. The observed differences between field strengths are not significant given the SDs of the data, with exception of the values for f and k_{MW} in approach 1. Analysis results of the grey matter ROIs are reported in Table 2.2. The $R_{1,WP}$ values for these regions resulting from analysis approach 2 are given in Table 2.3. Slice coverage in one subject did not allow creation of a GP ROI and this data was therefore not included in this part of the study. The average k_{MW} values in grey matter were higher than the value found in SCC white matter. However, it should be realized that the SD of the grey matter k_{MW} values was relatively high (up to 20%), and k_{MW} values themselves were not consistent between field strengths, suggesting they should be interpreted with caution.

The test-retest results (repeated scans at 3 T, n=5) indicated a 0.5% error for the ROI average f values in SCC, and a 5% error for the corresponding k_{MW} values at 3 T. Voxel-by-voxel test-retest analysis showed the error in f and k_{MW} in white matter to be around 0.015 and 1.1 s^{-1} respectively equivalent to 6% and 18% errors. The signal to noise ratio (SNR) in the (baseline) images was in the range of 200-400 at 7 T and 100-250 for 3 T. The image stability, based on the average variance in the SCC ROI over the repetitions within one scan series, was 2.9 ($\pm$0.4)% at 3 T and 1.7 ($\pm$0.4)% at 7 T. Omission of the IR data from approaches 1 and 2 strongly affected the fitting procedure, resulting in poor convergence and widely varying values for f and k_{MW}. This was not the case for approaches 3 and 4, in which the fixing of additional parameters improved fitting stability, and which led to similar results as approaches 1 and 2 (Fig. 2.8 and Table 2.1).

This indicates that IR data can be omitted from the analysis when fixing $R_{1,WP}$ and

$FS_{MP}(0)$ to values common to all brain pixels.

Table 2.1 Comparison of the four fitting approaches based on the 2-pool model, progressively fixing more parameters. Averages (Av) and SD (n=11) are shown for f and kMW for the SCC ROI, together with fit residue. The SD of the differences the 3 and 7 T data (diff) is an indication of the intra-subject reproducibility, the residue is reflects the fitting of the 2-pool model, which is the same for approaches 1 and 2 (both contain only 2 assumptions and therefore the same free fit of Eq. 2.1 to the data).

		Approach 1: Fixed $R_{1,MP}$, $R_{1,WP}$		Approach 2: Fixed $R_{1,MP}$, $FS_{MP}(0)$		Approach 3: + fixed $R_{1,WP}$		Approach 4: + fixed $FS_{WP}(0)$	
		Av	SD	Av	SD	Av	SD	Av	SD
f	3 T	0.262	0.012	0.274	0.014	0.287	0.021	0.282	0.022
	7 T	0.293	0.010	0.273	0.012	0.267	0.013	0.266	0.013
	diff	-0.031	0.008	0.002	0.015	0.020	0.022	0.016	0.023
k_{MW} [s^{-1}]	3 T	6.11	0.56	6.04	0.54	5.41	0.57	5.55	0.63
	7 T	5.01	0.29	5.13	0.32	5.30	0.45	5.30	0.46
	diff	1.09	0.66	0.91	0.68	0.12	0.75	0.25	0.81
Residue	3 T		1.7E-5			2.0E-5		1.8E-5	
	7 T		0.6E-5			0.5E-5		0.5E-5	

The estimated precision (the variability due to measurement noise) of the various

fitting results is shown in Table 2.4 for an input SNR (i.e. input to the fitting program) of

500. This estimate was derived from the stability of the SCC-ROI averaged signals over

repetitions, in combination with the effects of averaging over time and dividing by the

reference data. It was found that fitting errors simply scale (inversely) with SNR. The

test-retest errors for f and k_{MW} were consistent with the numbers shown in the Table 2.4.

The simulation shows that in spite of the high input SNR, the precision of k_{MW} is limited,

and the results need to be interpreted with some care.

Table 2.2 Results of three grey matter ROIs: Globus Pallidus (GP), Putamen (Put) and Head of the Caudate Nucleus (NC), shown as the average and SD over 10 subjects. The $R_{1,WP}$ used in approaches 3 and 4 was taken from the result of approach 2, as use of the global value for $R_{1,WP}$ is not suitable for these iron-rich regions.

	B_0	ROI	Approach 2: Fixed $R_{1,MP}$, $FS_{MP}(0)$		Approach 3: + fixed $R_{1,WP}$		Approach 4: + fixed $FS_{WP}(0)$	
			Av	SD	Av	SD	Av	SD
f	3	GP	0.172	0.010	0.176	0.012	0.172	0.013
		Put	0.124	0.009	0.125	0.010	0.122	0.010
		NC	0.113	0.005	0.113	0.006	0.111	0.008
	7	GP	0.181	0.013	0.185	0.015	0.182	0.015
		Put	0.122	0.014	0.126	0.017	0.124	0.016
		NC	0.114	0.011	0.116	0.015	0.114	0.013
$k_{MW}\,[\mathrm{s}^{-1}]$	3	GP	9.3	1.9	8.3	1.7	8.6	1.2
		Put	10.2	1.3	9.8	1.3	9.9	1.2
		NC	10.4	1.6	9.8	1.6	9.9	0.7
	7	GP	7.1	1.3	6.3	1.3	6.4	1.2
		Put	8.9	1.3	7.6	1.5	7.7	1.6
		NC	8.4	1.3	7.8	1.7	7.9	1.7

2 .4 Discussion and comparison with previous measurements of MP fraction

The experiments described in this work indicate the feasibility to measure the macromolecular proton (MP) fraction in human brain in scan times as short as 5 minutes. The measurement approach is based in instantaneous MP saturation, and analyzing the transfer of this saturation to WP as function of delay after the MT pulse using a 2-pool model of magnetization exchange.

The feasibility of this approach relies on the high (~90%) saturation efficiency of the composite MT pulse, as well as several simplifying assumptions, including the notion that R_1 relaxivity in human brain white matter is linearly dependent on MP fraction.

Strongly saturating MP while minimally (~10%) saturating WP is difficult to achieve with conventional MT approaches that use continuous off-resonance RF irradiation. A major advantage of the strong MP saturation achieved here is an excellent sensitivity in extracting f, owing to the large MT effect. In addition, strongly saturating MP reduces sensitivity to B_1 inhomogeneities as confirmed with simulations and experiments (Fig. 2.3). This property enabled reliable extraction of f, even at 7 T where B_1 inhomogeneity is substantial. In contrast, poorly designed MT pulses may show reduced saturation in areas with low B_1, which, if not accounted for, will cause f to be underestimated.

Another advantage of the type of MT pulse used here is its minimal affect on WP, by virtue of their long T_2 WP, even in the presence of off-resonance effects due to B_0 inhomogeneities. Sensitivity to the latter can be adjusted by changing the number of sub-pulses, while keeping pulse duration constant. The overall pulse energy (time integral of B_1 amplitude squared) determines the T_2 value below which MPs are fully saturated, while the combination of B_1 amplitude and number of sub-pulses determines the T_2 values above which WP magnetization is left untouched. Within the limits of the scanner hardware and allowable tissue heating, this gives sufficient flexibility to efficiently implement the pulsed MT approach at both 3 T and 7 T.

Quantifying f and k_{MW} with the 2-pool model fitting approach required simplifying assumptions which, in this study, involved fixing two or more parameters to values common to all brain voxels and all subjects (n=11). These parameters included $R_{1,MP}$, $R_{1,WP}$ and the saturation levels of MP and WP resulting for the direct effect of the MT pulse. Similar values for f and k_{MW} were obtained for different sets of parameter

combinations, and the similarity of the results between 3 T and 7 T supported the validity of this approach. Importantly, fixing 3 or more parameters (approaches 3 and 4, see METHODS) obviated the need for inclusion of IR data in the fitting process, reducing the measurement time to only 5 minutes. The use of four fixed parameters (approach 4) allows further scan time reduction as it removes the necessity of acquiring a reference scan without MT pulse.

The excellent precision of the MP-pool fraction estimate, as determined from simulations and the test-retest results, demonstrates the sensitivity of the proposed transient MT approach. This is further supported by the small SD over subjects of the difference of the measurements at 7 T and 3 T. The short, 5-minute scan time compares favorably to the more traditional steady-state qMT methods, which generally require longer scan times and may be difficult to perform at high field (7 T and above) due to the significant RF power deposition associated by conventional saturation approaches. In addition, in contrast to steady-state MT approaches, the transient MT approach proposed here is minimally sensitive to variations in $R_{1,WP}$, therefore obviating the need for additional IR experiments. This is because of the assumed relationship between f and λ_2, and the relative low saturation level of WP resulting from the pulsed saturation. Although resulting in a less direct measurement of f, the proposed method may be more practical than approaches based on direct detection of MP signal at very short TE (35,59,107,108), which suffer from limited sensitivity and are technically challenging.
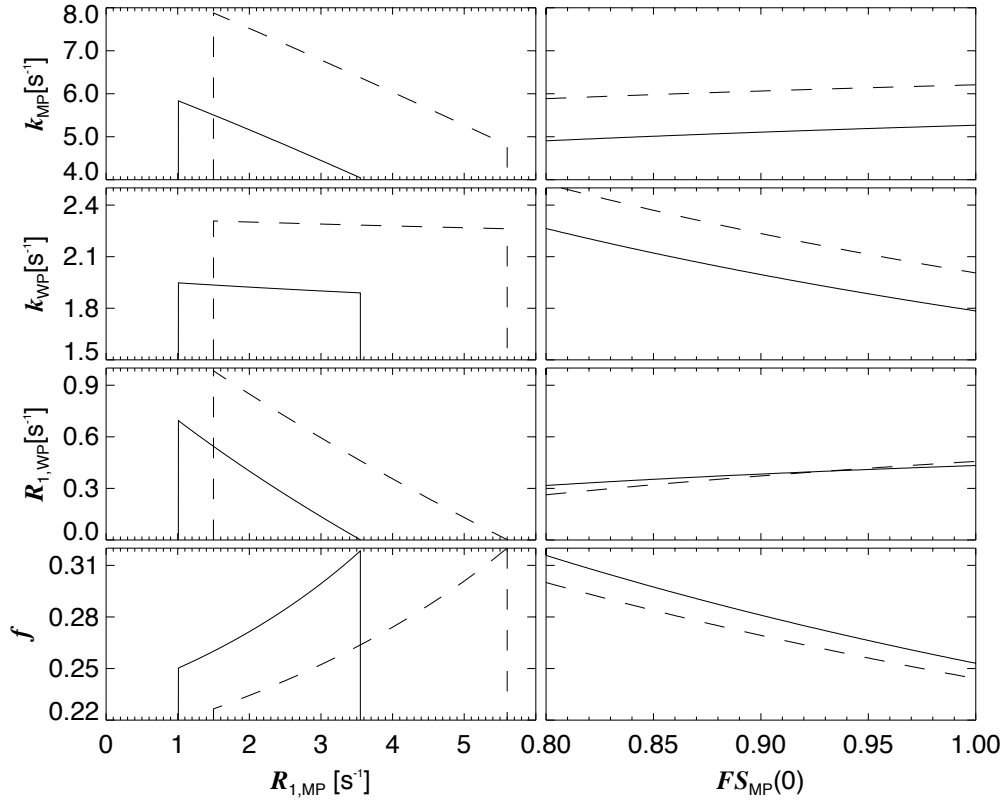
Figure 2.10 Simulated dependence of the extracted parameters (approach 2) on values assumed for $R_{1,MP}$ and $FS_{MP}(0)$, based on experimentally derived values for a, b, λ_1 and λ_2 (Eq. 2.1). The dashed lines are for 3 T data, the solid lines for 7 T. Actual (experimental) values were: $R_{1,MP}=$ 4.0 s^{-1} , $FS_{MP}(0)=0.88$ for 3 T and $R_{1,MP}=$ 2.05 s^{-1}, $FS_{MP}(0)=0.93$ for 7 T.

The white matter MP fractions reported here (f~15-25%) are substantially larger than the range of 9-16% found previously with quantitative MT methods (40,63,90,93,94,109). This may in part relate to methodological differences, for example the efficiency of the MT pulses used to saturate MP between the different methods. Nevertheless, our values seem reasonable considering the water content of white matter, which has been reported to be around 70% (28,36,80–82). Since the proton density of the 30% non-water fraction is at least similar to that of water (e.g. proton density of myelin is 35% higher than that of water (59), while in proteins it may be somewhat lower than in water), one would expect that the MP fraction in white matter to not be far below 30%.

This of course assumes that all of the saturated MPs participate in the MT process. As in white matter, the grey matter MP fractions found here are somewhat higher than estimates from qMT measurements: 8-9% for GP, 7% for Put, and 5.3-6.7 % for NC (63,90,110). On the other hand, the k_{WM} are similar to literature values (1.4-2 s^{-1}) (19). Compared to estimates based on the non-water content of tissue (23-26% for GP, 18-21% for Put and 17-19% for NC (28,36,80–82)), our MT-based estimates are somewhat low but not entirely unreasonable given the uncertainty in grey matter ^{1}H content.

In addition to differences in MP saturation levels, a reason for the relatively high values of f reported here as compared to much of the MT literature may be differences in assumed values for $R_{1,MP}$. Previous MT studies have generally assumed R_1 to be similar between MP and WP (e.g. around 1 s^{-1} at 1.5 T), and it has been pointed out that this value may be too low and lead to under-estimation of f (34). In the current work much higher values of 3.8 s^{-1} and 2 s^{-1} were estimated for $R_{1,MP}$ at 3 T and 7 T respectively, based on fitting of the 2-pool model to the MT and IR data. Since much of the R_1 relaxivity of WM is thought to originate from exchange with MP (12,33,88), such high values for $R_{1,MP}$ are not unexpected. A further indication that $R_{1,MP}$ may previously have been underestimated comes from the observation that fixing $R_{1,MP}$ to 1 s^{-1} during the fitting procedure indeed led to lower values of f: reductions of about 20% and 10% were estimated at 3 T and 7 T respectively (Fig. 2.10). However, under this condition, the fits led to inconsistent values for k and f between the two field strengths.

The finding of $R_{1,MP}$ being substantially higher than $R_{1,WP}$ is consistent with earlier analysis of the relationship between apparent R_1 and f based on of large collection of MRI brain data (33). Further support for a relatively high $R_{1,MP}$ comes from

measurements on membrane lipids in model systems, which have found values ranging from 1.6 s^{-1} to 4.6 s^{-1} for $R_{1,MP}$ at fields ranging from 8 to 1.4 T (37,56,111). Nevertheless, it should be realized that $R_{1,MP}$ is difficult to measure directly and dependent on experimental conditions (e.g. temperature). Thus, the precise value of $R_{1,MP}$ remains uncertain and likely is not uniform across and within molecular species: for example it may vary substantially between different lipids.

Table 2.3 The average and SD over ten subjects of the $R_{1,WP}$ values for the 3 grey matter ROIs following from approach 2 as used in approaches 3 and 4.

B_0	ROI	$R_{1,WP}$ [s^{-1}]	
		Av	SD
3	GP	0.505	0.035
	Put	0.466	0.018
	NC	0.449	0.016
7	GP	0.448	0.032
	Put	0.444	0.018
	NC	0.426	0.021

Table 2.4 Estimated precision for f and kMW for an (ROI-) SNR of 500 (for both saturation and reference scans), based on fitting of model data with simulated noise; the model data was based on average values found for f and kMW in the SCC (Table 2.1). The relative precision is given in parenthesis.

		Approach 1,2: Fixed $R_{1,MP}$, $FS_{MP}(0)$	Approach 3: + fixed $R_{1,WP}$	Approach 4: + fixed $FS_{WP}(0)$
f	3T	0.0081 (3%)	0.011 (4%)	0.0084 (3%)
	7T	0.0054 (2%)	0.0064 (2.5%)	0.0054 (2%)
k_{MP} [s^{-1}]	3T	0.32 (6%)	0.39 (7%)	0.25(5%)
	7T	0.22 (4%)	0.26 (5%)	0.17 (3%)

In order to be able to estimate k_{MW} and f without the use of IR data, we assumed $R_{1,WP}$ to be constant over the brain. This was motivated by the notion that much of T_1 relaxation in brain tissue is mediated by MT between MP and WP. Nevertheless, there

are other contributions to T_1 relaxation, most notably those from paramagnetic substances such as iron. In fact, in regions richest in iron such as the basal ganglia (concentration up to 0.2 mg/g (79)), $R_{1,WP}$ may increase by as much as 0.15 s^{-1} at 7 T (33). This was also observed in the results of analysis approach 2, in which $R_{1,WP}$ was allowed to vary (Fig. 2.6). Failure to take this into account will affect the values of k_{MW} and f: simulations indicate that it will bias their estimates by about 15% (data not shown). Thus, accurate determination of k_{MW} and f throughout all of the brain may require collection of additional data (e.g. T_2^*-weighted MRI (112)) from which the local concentration of iron can be inferred, and then used to adjust $R_{1,WP}$. Alternatively, $R_{1,WP}$ can be estimated using joint analysis of IR and MT data, as was done here with analysis approach 2. The resulting $R_{1,WP}$ values were indeed higher than the global values, consistent with the effect of iron on R_1 relaxivity (33).

The values for exchange rates k_{MW} and k_{WM} found here are somewhat lower than those reported in literature. For example, the value of ~2 s^{-1} for here for k_{WM} found here is somewhat below the range of 2.5-3.9 from previous studies (90,109,113). Again (as with f), a potential source for this discrepancy is the value used for $R_{1,MP}$ which we estimated higher than assumed previously. It is also interesting to compare the exchange rates found here with those from fitting of transient MT data to a 4-pool model in a previous study (74). This study reported on cross-relaxation time constants T_{CR}, a measure of exchange rates defined by $T_{CR} = k_{MW}^{-1} + k_{WM}^{-1}$. In SCC, T_{CR} representing exchange between MP in myelin to WP outside the myelin sheath (i.e. the water visible in our study) was reported to be at least 1280 ms and limited by exchange between water compartments within and outside the myelin sheath (74). A similar calculation based on a

3-pool exchange model for rat optic nerve data yields a T_{CR} of 890 ms (85). These values

compare to a value of about 600 ms calculated from Table 2.1. Thus, while our exchange

rates appear somewhat slower than reported in previous MT studies, they are higher than

those suggested by cross-relaxation studies that take into account a myelin water

compartment. Due to the short $T_2{}^*$ of myelin water, our measurements were dominated by

signal from axonal and interstitial water, and therefore could not account for the effect of

inter-compartmental water exchange on k_{WM}.

Although the fitting results suggest that both k_{MW} and f can be robustly estimated

with the proposed method, there are several factors that can affect the accuracy of the

estimated values. We will discuss a few of them, realizing that our list may be

incomplete.

First, it is possible that a sizeable fraction of MP is incompletely saturated, which

would lead to a commensurate underestimation of f. If not properly taken into account,

this can bias f and therefore also k_{MW}. From experiments with varying MT pulse

durations, in particular the comparison of the 6 ms saturation to the 11 ms pulse, it is

apparent that the longer pulse is only 10% more effective, suggesting these pulses

saturate the MP-pool nearly completely (if not, dependence on pulse duration should be

stronger). This notion of nearly complete saturation with the 6 ms pulse is only valid for

MP with $T_2 < 400$ µs, i.e. those that are relatively immobile; protons on freely rotating

end-groups of larger molecules are not included in the measured MP-fraction as they are

not efficiently saturated by the MT pulse. Fortunately, such mobile protons form only a

small fraction of the total MP pool, and will therefore not substantially affect the estimate

of f.

Secondly, a small error is introduced due of the incomplete signal recovery associated with the finite TR in our experiments. The TR of 3 s for the MT experiment was substantially longer than the effective T_1 in tissue, but not sufficiently long to ignore incomplete signal recovery: ideally this should be incorporated in the analysis model. Fortunately, because this issue affects both the MT and the reference data, simulations indicated that associated errors were small, i.e. lower than 2% for f and 7% for k_{WM} and k_{MW},. Nevertheless, when using the proposed method with a shorter TR to increase time efficiency, it may become necessary to account for incomplete signal recovery effects in the model equations.

Third, the precision of the exchange rates k_{MW} and k_{WM} estimate depends on the available signal differences and therefore on the size of the MP-pool. If the MP-pool fraction f is low, the precisions of k_{MW} and k_{WM} will be low too. This effect and possibly partial volume effects with CSF explain the brighter pixels towards the edge of the brain slices shown in Fig. 2.8, especially for the (lower SNR) 3 T images.

Fourth, the two-pool model applied here is a gross simplification and may cause significant systematic errors in the estimates of f and the exchange rates. For example, accurately representing magnetization transfer through multiple myelin layers and between white matter water compartments (e.g. intra-axonal versus interstitial) may require a many-pool model, or the modeling of a diffusion process. This problem may be exacerbated when the actual MP and WP R_1 strongly deviate from their assumed average values, or have a distribution that is not accurately represented by an average. The values of k_{MW} and f also depend somewhat on the measurement approach, and the extent to which TE and TR affect the visibility of the different water pools. For example, about

15% of WP in WM may be situated between the myelin layers (72,85,86) and only marginally visible at the long TEs used in our experiments. This biases f, because of an underestimation of WP volume. Similarly, limited visibility of WP between the myelin layers biases k_{MW}, as its determination, in our experiments, depends on mixing of the magnetization between the various WP pools.

Fifth, as indicated above, the assumption of single value of $R_{1,WP}$ and $R_{1,MP}$ for all brain tissues may not be valid, and lead to inaccuracies in k_{MW} and f. For example, in disease, $R_{1,WP}$ and $R_{1,MP}$ could change due to iron accumulation or changes in tissue molecular structure respectively; also, it is possible that pathological conditions could render k_{MW} too low to cause WP saturation levels sufficient for accurate quantification of f. It remains to be seen to what extent these issue arise in practice.

Our approach compares favorably with previous methods proposed for rapid measurement of f. An interesting comparison is with IR-based methods (47) which have the potential in providing improved sensitivity (compared to out MT approach) owing to a potentially 2-fold increase in initial saturation difference between MP and WP. However, this improvement may not be realized in practice due to the difficulty in inverting WP without substantial saturation of MP. In addition this MP saturation will be dependent on B_1 power, rendering the quantification of f sensitive to B_1 inhomogeneities. Alternatively, rapid measurement of f can be performed with a transient MT method based on a stimulated echo preparation (99): this approach however suffers from a 2-fold sensitivity reduction associated with stimulated echoes, and furthermore has substantial sensitivity to B_1 inhomogeneities.

In the presented experiments, only few slices were acquired, the number of which was tied to the number of delay times. One way to extend slice coverage is to move the selected set of slices with successive repetitions of the MT pulse, while shortening the MT repetition time. When keeping the slice repetition time (i.e. time between successive excitations of the same slice) constant, this should only minimally affect the sensitivity of the experiment, as the WP saturation caused by the MT pulse is a small fraction of the total magnetization. Alternatively, or additionally one can perform simultaneous multi-slice acquisitions, or acquire data in 3D fashion, where the excitation is performed over the entire brain and phase encoding is performed over the through-plane direction (perpendicular to the plane encoded by EPI). This would allow large brain coverage in clinically feasible scan times, in particular when reducing the number of delay times to three (or even two) by fixing an increasing number of model parameters. The practical benefits of these approaches are currently being investigated in our laboratory.

We implemented a rapid, transient MT approach to measure the fraction of macromolecular protons f. Because of its insensitivity to B_1 inhomogeneities, and its minimal RF power deposition, the approach can be readily applied at high field, where its sensitivity benefits substantially from the slower T_1 relaxation of macromolecular protons. Values of f in white matter, obtained by fitting the MT data to a 2-pool model, and assuming a dominant contribution of MT to longitudinal relaxation, were found to be about 50% higher than previous estimates. This is partly attributed to discrepancies in the estimates of R_1 of macromolecular protons, which was much higher here than reported previously.

Chapter 3: Effects of Magnetization Transfer on the T_1 Contrast of Human Brain White Matter

In most of the previous transient MT experiments reported in literature, the effect of RF pulses used for image acquisition on MP magnetization has been ignored or assumed negligible (45,50). However, this assumption is not generally valid. Here we take MP magnetization in consideration and present robust estimation of two-pool exchange model parameters, as introduced in Section 1.2. We do this by using RF pulses, whose amplitude is high enough (B_1=833 Hz) to almost completely saturate MPs, independent of the (unknown) T_2 of MPs. The two-pool exchange model parameters are then reliably determined and contribution of MPs to T_1 contrast through MT is quantified. This work is adapted from our manuscript published in *Neuroimage* (2).

3 .1 *The importance and previous studies on T_1 weighted contrast*

Longitudinal proton relaxation (also called T_1 relaxation) is one of the major MRI contrast mechanism used for studying brain morphology, and is widely used for clinical diagnosis. Resulting from the magnetic interaction of protons with their environment, it is dependent on tissue composition and structure, including the local concentration of proteins and lipids. Additional, and sometimes strong contributions may come from atoms and molecules with para- and ferromagnetic properties such as endogenous iron and deoxyhemoglobin, or injected contrast agents such as Gd-DTPA and Feridex.

T_1-weighted MRI techniques such as MP-RAGE (8) and inversion recovery (IR) fast spin echo (see e.g. (114–118)), both of which are based on signal recovery after instantaneous magnetization inversion, are being extensively used for the distinction

between brain tissue types, including the segmentation of grey matter, white matter, and CSF. The distinctly different T_1 relaxation between grey and white matter has been attributed on their different myelin content: myelin rich white matter contains an up to 30% fraction of proteins and lipids (36), whose largely invisible hydrogen (^{1}H) protons exhibit rapid T_1 relaxation (37–39) and, through magnetization transfer, accelerate T_1 relaxation of MRI-visible water ^{1}H protons (WP's). Thus, study of T_1 relaxation with inversion recovery may allow quantification of this magnetization transfer (MT) (43–45) and aid in determining brain myelin content (119), which has important neuro-scientific and clinical applications (25). MRI techniques such as MP2RAGE (7,120) and DESPOT1 (121) have recently been proposed and are increasingly being used for this purpose (122).

One of the outstanding issues with quantification of the T_1 time constant is the limited reproducibility of the various methods and the variation in T_1 estimates reported in literature (see e.g. (49,51)). While incompletely understood, this variability can be partly attributed to imperfect WP inversion, and a potential bi-exponential character of the relaxation that is not properly accounted for during analysis (49,51–53). As a result, generalizability of T_1 quantification results is rather limited, hampering the study of brain myelination, and affecting the accuracy of tissue segmentation.

The goal of the current work was to investigate the presence of bi-exponential longitudinal relaxation in human brain and its dependence on experimental parameters, including inversion pulse type and magnetic field strength. For this purpose, dedicated IR experiments were performed at 3 T and 7 T, as well as MT experiments in which non-water ^{1}H protons were selectively saturated by replacing the inversion pulse by an MT

pulse. Conjoint analysis using a two-pool model of MT showed that in white matter, T_1 relaxation is strongly dependent on the effect of the inversion pulse not only on WPs, but also on the non-water ^{1}H protons. In addition, we provide realistic estimates for the T_1 of these protons, an essential parameter for the interpretation and quantification of T_1 and MT data.

3 .2 *Two-pool exchange model*

Background

Myelin is an important contributor to T_1 contrast between brain regions (12). The mechanistic interpretation has been that ^{1}H protons on larger molecules (such as the proteins and lipids that are abundant in myelin) have short T_1 and this affects the T_1 of WPs by means of MT through mechanisms such as dipolar coupling and chemical exchange. This notion is corroborated by the fact that, in human brain, the relaxation rate R_1 $(=1/T_1)$ strongly correlates with (semi) solid (i.e. non-water) fraction (33,80,87). Similarly, study of MT effects with experiments that selectively affect (i.e. saturate) the (semi) solid proton fraction (from here onwards categorically, but somewhat incorrectly, indicated by macromolecular proton fraction, or MP fraction) have found a dominant effect in myelinated tissue, and such experiments have been used to measure myelin loss in diseases such as MS. Thus, MT is an important mechanism underlying T_1 relaxation in the human brain.

Study of T_1 relaxation *in-vivo* is typically performed with IR-type experiments (of which MPRAGE is an example) that measure recovery of the longitudinal magnetization (indicated with *M(t))* at one or more time-point(s) *t* after inversion of the WP magnetization by a radiofrequency (RF) inversion pulse. In pure liquids with only one

species of ^{1}H, $M(t)$ can generally be described by a single exponential function, characterized by time constant T_1. For the more complex situation of brain tissue, it has been suggested that $M(t)$ can be approximated by using a two-pool model of MT between WP and MP, which leads to bi-exponential behavior (46–49):

$$FS_{WP}(t) = 1 - \frac{M_{WP}(t)}{M_{WP}(\infty)} = a_1 e^{-\lambda_1 t} + a_2 e^{-\lambda_2 t} \qquad (3.1)$$

$$2\lambda_{1,2} = R_{1,WP} + R_{1,MP} + k_{MW} + k_{WM} \pm \sqrt{(R_{1,MP} - R_{1,WP} + k_{MW} - k_{WM})^2 + 4k_{MW}k_{WM}}$$

$$(3.2)$$

$$a_{1,2} = \pm \frac{S_{WP}(0)(R_{1,WP} + k_{WM} - \lambda_{2,1}) - S_{MP}(0)k_{WM}}{\lambda_1 - \lambda_2} \qquad (3.3)$$

$$(1 - f)k_{WM} = f k_{MW} \qquad (3.4)$$

Here, $M(t)$ is converted to fractional saturation $FS(t)$, which can range from 0-2. Indices WP and MP refer to water protons and macromolecular protons respectively. The fast (λ_1) and slow (λ_2) rate constants are determined by the intrinsic relaxation and exchange rates of the tissue, while the amplitudes (a_1 and a_2) depend on the conditions of the experiment, including the properties of the RF pulse. These equations broadly apply to any type of RF pulse, including imperfect inversions or MT pulses that selectively saturate the MP pool. The first order MT rate constants from WP to MP and *vice versa* are given by k_{WM} and k_{MW} respectively; these relate through the MP pool fraction f according to Eq. 3.4 (Because of this relation between the exchange rates, the model can be equivalently be described in terms of one of the two rate constants (k) and the MP-pool fraction (f)). $R_{1,WP}$ and $R_{1,MP}$ are relaxation rates in absence of exchange.

Importantly, the amplitudes of the two exponential functions (a_1 and a_2) are not only dependent on the effect of the RF pulse on WP, but also on MP. Because the latter (i.e. $FS_{MP}(0)$) is difficult to estimate (FS_{MP} is not directly visible), previous work has

used simplifying assumptions equating $FS_{MP}(0)$ to either 1 (77) or 0 (35). In the following, we will show that under practical conditions, the actual value of $FS_{MP}(0)$ can differ substantially from these values, and demonstrate the effect of $FS_{MP}(0)$ on the bi-exponential nature of the recovery curve. For this purpose, estimates of $FS_{MP}(0)$ were derived from joint analysis of recovery curves obtained with four different inversion pulses and one MT-type RF pulse (the latter referred to as "MT data"), as detailed in the next section. Qualitative estimates were also derived from simulations of the MT and inversion pulses with numerical solution of the Bloch equations (see section "simulations" below).

3.3 Estimating $FS_{MP}(0)$ experimentally

While λ_1, λ_2, a_1, a_2 can be directly determined from fitting of $FS_{WP}(t)$ in Eq. 3.1 to IR or MT data, estimation of $FS_{MP}(0)$ requires subsequently solving Eqs. 3.2 and 3.3, which represent 4 equations with the 6 unkowns: $FS_{WP}(0)$, $FS_{MP}(0)$, $R_{1,MP}$, $R_{1,WP}$, k_{WM}, and k_{MW}. To resolve this, at least two constraints need to be added to the system of equations. Here, this was done in a two-pronged, sequential analysis approach: 1) A voxel-wise analysis was performed which assumed $R_{1,MP}$ and $R_{1,WP}$ to be constant across the brain and determined their approximate values by constraining $FS_{MP}(0)$ to have realistic values for both IR and MT data; 2) Then a region-of-interest (ROI) analysis was performed which used $R_{1,MP}$ found from the global analysis and fine-tuned $R_{1,WP}$ using assumed $FS_{MP}(0)$ for the MT data, and then accurately determined $FS_{MP}(0)$ for the four different inversion pulses. Further details are provided below under "data analysis".

58

The rationale for assuming constant $R_{1,MP}$ and $R_{1,WP}$ is based on the above-mentioned the notion that in WM, the dominant source of T_1 contrast are variations in f, with the two having a close to linear relationship (11,12,28,33,80,123,124)

3.4 *MRI measurements*

Ten subjects participated in this study (ages 19-60, average 30.4, 6 female), after consenting into an IRB approved protocol. Subjects were scanned at both 3 T and 7 T scanners (Siemens, Erlangen, Germany; Skyra and Magnetom platforms respectively) using 32-channel receive arrays.

IR measurements were performed using and adiabatic pulse and 3 different composite pulses. The adiabatic pulse (indicated by 'A5.1') was a commonly used hyperbolic secant of 5.12 ms duration, 0.51 $(\mu T)^2$s energy, a B_1 modulation frequency of 833 Hz and a β of 1400 s^{-1} (104); for optimal inversion efficiency, its amplitude was adjusted to smoothly start and end at zero. The three composite inversion pulses (90^0_x-180^0_y-90^0_x) were designed to lead to different levels of $FS_{MP}(0)$ by varying their energy. For this purpose, pulse duration was varied between 1.2, 3.6 and 6.9 ms (pulses indicated by 'C1.2','C3.6' and 'C6.9' respectively; corresponding B_1's: 833, 278 and 145Hz, energies: 0.46, 0.15, and 0.08 $(\mu T)^2$s). The MT pulse consisted of a train of 17 hard pulses with angles 60°, -120°, 120°, -120°, …., -120°, 60°, a total length of 6 ms and a B_1 amplitude of 833 Hz.

Image data were acquired with single-shot EPI, sampling 5 slices consecutively after each RF inversion or MT pulse; cycling the slice order over 5 repetitions thus resulted in acquisition of 5 delay times for each slice (125). Slices of 2 mm thickness

were placed with 1.5 mm separation parallel to AC-PC line and encompassed the central part of the corpus callosum. The inversion delay (TI) values were 9, 71, 147, 283 and 1200 ms at 3 T and 7, 64, 145, 283 and 1200 ms at 7 T (defined as the time from the center of the inversion pulse to the center of the EPI excitation pulse). The delay times for the MT experiments were: 10, 72, 138, 258 and 600 ms for 3 T, and 8, 62, 137, 256 and 600 ms for 7 T. The times were chosen to preferentially sample the early part of the IR curve, within the constraint of the minimal slice TR set by the duration of the EPI readout. The image resolution was 144x108 with SENSE rate-2 acceleration, the field-of-view was 240x180mm. The echo time (TE) was 30 ms at 3 T and 24 ms at 7 T, the TR 4 s for the inversion experiments, and 3 s for the MT experiment. In order to suppress signals from scalp lipids, the TE was increased on even numbered repetitions. This increase amounted to 1.15 and 0.48 ms for 3 T and 7T respectively, resulting in a phase inversion of the lipid signal with respect to water (assuming a 3.5 ppm frequency difference between lipid and water). Summation of odd and even numbered images thus resulted in cancellation of lipid signal. Fourteen repetitions were acquired at 3 T and 18 at 7 T, the first 4 of which omitted the inversion (or MT) pulse and used to provide a reference signal to estimate $M_{WP}(\infty)$ in Eq. 3.1, and allow conversion of the measured signals to saturation levels ($FS_{WP}(t)$).

3.5 *Data processing and estimation of $R_{1,MP}$*

Pre-processing

Pre-processing included motion correction, averaging, polarity correction, and calculation of signal saturation levels. Prior to averaging repetitions, complex images were spatially registered to correct for motion. Only in-plane registration was performed,

as the small number of slices did not support through-plane motion correction. For the inversion data, polarity correction was applied to the magnitude signal based on the phase difference with the (un-inverted) reference image. This was a largely automatic procedure, however, in a small number of voxels manual signal polarity adjustment was required for the longest TI. The fractional magnetization level expressed in Eq. 3.1 was determined by dividing each inversion image by the corresponding reference image (i.e. data acquired without inversion pulse). This was done for all voxels where the reference signal exceeded 5% of maximum. Analogous analysis was performed for the MT data, however without performing the signal polarity adjustment. All processing was done in IDL (Exelsis Visual Information Solutions, Boulder, CO, USA).

Voxel-wise analysis

To derive estimates for $R_{1,WP}$ and $R_{1,MP}$, data from a single IR experiment (using the adiabatic pulse) was analyzed jointly with the MT data on a voxel-wise basis (Fig. 3.1). This was done for both field strengths and involved the following steps:

1. Jointly fit MT and IR data to Eq. 3.1, yielding one pair of decay rates (λ_1, λ_2) and two pairs of amplitudes (a_1, a_2) for each voxel.

2. Assuming global values for $R_{1,WP}$ and $R_{1,MP}$, calculate corresponding levels of $FS_{MP}(0)$ for IR and MT experiments for each voxel, based on decay rates and amplitudes found in step 1.

3. Adjust $R_{1,WP}$ and $R_{1,MP}$ and recalculate $FS_{MP}(0)$ to maximize the number of voxels with $FS_{MP}(0)$ values consistent with pre-determined constraints.

Global R_{1MP} and R_{1WP} estimation
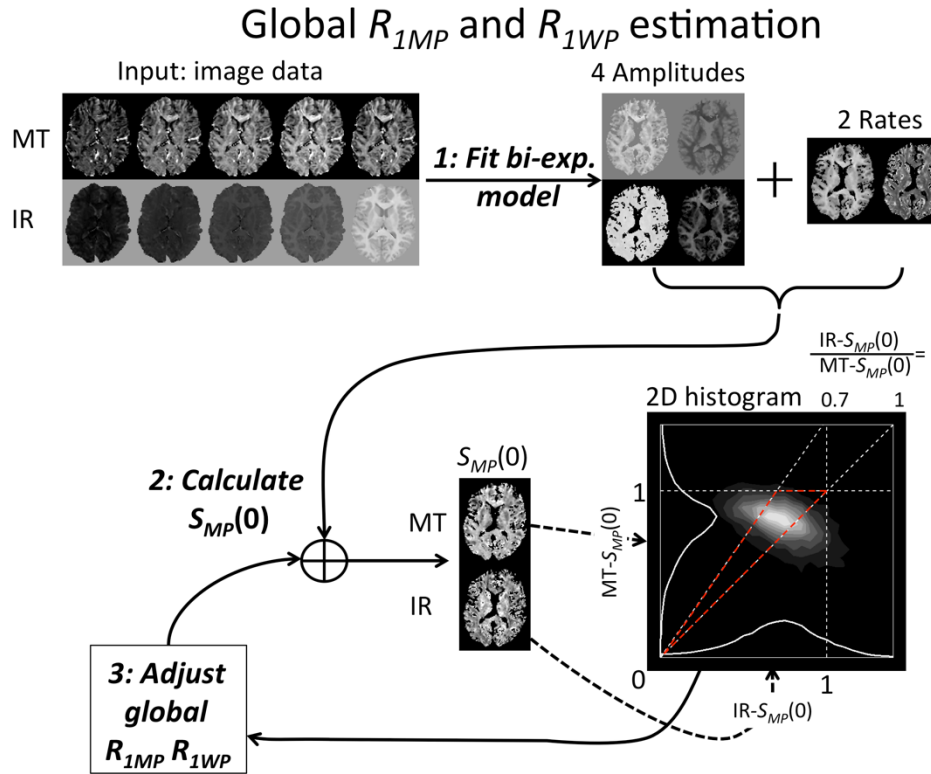
Figure 3.1 Voxel-wise fitting and parameter extraction to derive global $R_{1,MP}$ and $R_{1,WP}$ estimates. First (step 1) is the combined fitting of bi-exponential model to data from MT experiment and a single (A5.1 pulse) IR experiment. In step 2, $FS_{MP}(0)$ values are calculated for both experiments based on global values for $R_{1,MP}$ and $R_{1,WP}$. Then (step 3) R1 values are adjusted iteratively (repeating step 2) to maximize the fraction of voxels with $FS_{MP}(0)$ values within in the expected boundaries, outlined by the red triangle.

The constraints for step 3 were as follows: a) $FS_{MP}(0)<1$ for both IR and MT data (MP can not be inverted due to their short T_2) , b) based on the pulse durations and energy (6.0 resp. 5.1ms, 2.3 resp. 0.51 $(\mu T)^2$s), the ratio of $FS_{MP}(0)$ for the adiabatic inversion pulse and the MT pulse is between 0.7 and 1.0 as determined from simulations (details below and in Fig. 3.3a and c).

ROI analysis for $S_{MP}(0)$ and $S_{WP}(0)$ with Inversions
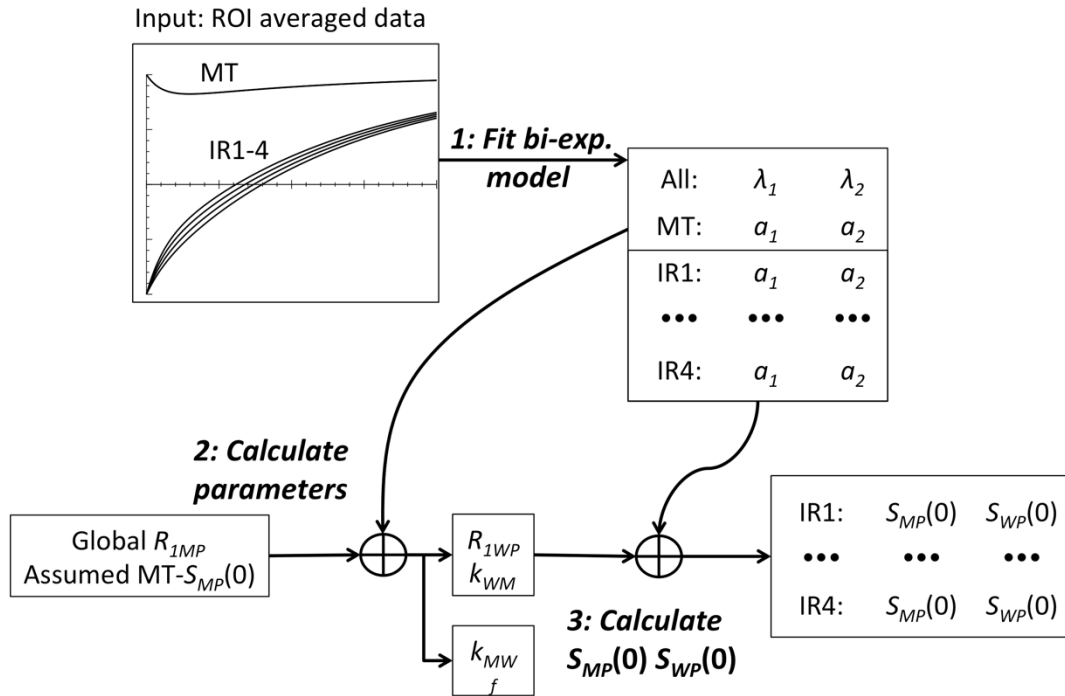
Figure 3.2 ROI-based fitting and calculation of $FS_{MP}(0)$ and $FS_{WP}(0)$ for IR data. First, (step 1), ROI-averaged data from MT experiment and IR experiments with four different inversion pulses are fitted to the bi-exponential model, resulting one set of λ's and 5 sets of values for a_1 and a_2. Then (step 2), based on global $R_{1,MP}$ from voxel-wise analysis (see Fig. 3.1), and assumed $FS_{MP}(0)$ for MT experiment, the MT parameters extracted in step 1 are used to calculate R_{1WP}, k_{WM}, k_{MW} and f. Then, in step 3, R_{1WP}, and k_{WM} are combined with the IR a's and λ's from step 1 to calculate the $FS_{MP}(0)$ and $FS_{WP}(0)$ for each IR experiment.

ROI-based analysis

ROI analysis was performed on all datasets in order to fine-tune $R_{1,WP}$ and calculate $FS_{MP}(0)$ for each of the four inversion pulses (Fig. 3.2). For this purpose, in each subject, a WM ROI in the splenium of the corpus callosum was selected manually, and $R_{1,MP}$ was set to the value found by the voxel-wise analysis. Furthermore $FS_{MP}(0)$ values for the MT pulse were set to 0.88 and 0.92 for 3 T and 7 T respectively, based on previous measurements that investigated $FS_{MP}(0)$ dependence on MT pulse length. The

rationale for fine-tuning $R_{1,WP}$ based on assumed levels of $FS_{MP}(0)$ for the MT experiment was that the latter was relatively well known, compared to the significant uncertainty in $R_{1,WP}$ found in the voxel-wise analysis.

The ROI-based analysis involved the following steps:

1. Jointly fit MT and IR data to Eq. 3.1, yielding one pair of decay rates (λ_1, λ_2) and five pairs of amplitudes (a_1, a_2).

2. Using the fixed values for $R_{1,MP}$, and $FS_{MP}(0)$ for the MT data, as well as the decay rates and MT amplitudes from step 1, calculate $R_{1,WP}$ and MT rates (k_{WM} and k_{MW}).

3. Calculate $FS_{MP}(0)$ for each of the four inversion experiments using their specific pairs of amplitudes.

Finally, in order to estimate reproducibility, for each fitted parameter, the standard deviation (SD) over subjects was calculated.

Simulations

Simulations were performed to study the various aspects of the experiment, including the effects of the IR and MT pulses on $FS_{WP}(0)$ *and* $FS_{MP}(0)$, the effect of $FS_{MP}(0)$ on the IR signal trajectory, the effect of noise and finite TR on parameter fitting. All simulations were performed in IDL.

Effect of inversion and MT pulses on $FS_{WP}(0)$ and $FS_{MP}(0)$

Simulations of the effects of the inversion and MT pulses on $FS_{WP}(0)$ and $FS_{MP}(0)$ were based on the Bloch equations and investigated dependence on T_2, assuming single exponential T_2 decay. For this purpose, temporal evolution was discretized using 1 μs time steps, and the evolution of the three Cartesian components of the magnetization was

effectuated by successively applying rotations and multiplications to represent effects of the RF pulse and T_2 decay respectively. One hundred different T_2 values were used, exponentially distributed between 1 μs and 1 s. In a second simulation, pulse length of the composite inversion pulse was varied (and as a result its energy) at a single T_2 (70 μs, in the estimated range of MP), to illustrate the effect on $FS_{MP}(0)$. Exchange was ignored in both simulations, as the applied RF pulses are short compared to the relevant exchange rates. A Lorentzian line shape (implicit in the exponential solution to the time domain Bloch equations) was used for three reasons: a) calculations with different line-shapes requires treatment in the spectral domain, which implies linearity of the system, an assumption that is applicable for small tip-angles experiments but not necessarily for inversions and/or short, high-power MT pulses; b) it has been suggested that in myelin, MP may exhibit a Lorentzian lineshape (59) with a T_2 in 60-100μs range;   c) this simulation is meant as a general illustration of the pulse effects, not as an exact study of MP T_2 values and line shapes, and it can be reasonably assumed different line-shape models would show similar trends as function of pulse power.

The effect of $FS_{MP}(0)$ on the IR signal trajectory

To investigate the effect of $FS_{MP}(0)$ on T_1 relaxation, the magnetization trajectory of the two pools in the IR experiment was simulated using the two-pool model equations (Eqs. 3.1-3.4) and the parameters found from fitting of the experimental data obtained at 7 T. Two extreme cases were simulated: one with complete saturation of the MP pool ($FS_{MP}(0)$= 1.0) and one without any saturation ($FS_{MP}(0)$= 0.0), while the WP pool was assumed to be perfectly inverted in both cases ($FS_{WP}(0)$= 2.0). This simulation was run for both field strengths separately, as the $R_{1,MP}$ was found to be field dependent. From this

data, the relative contribution of the rapidly relaxing component (rate λ_1) to the IR curve was estimated and a TI value was extracted above which its contribution becomes negligible. This was done by calculating the instantaneous T_1 (from $-S(t)/(dS(t)/dt)$) and ascertain when this reaches 95% of its long TI limit value, which is the inverse of the slow component rate (λ_2).
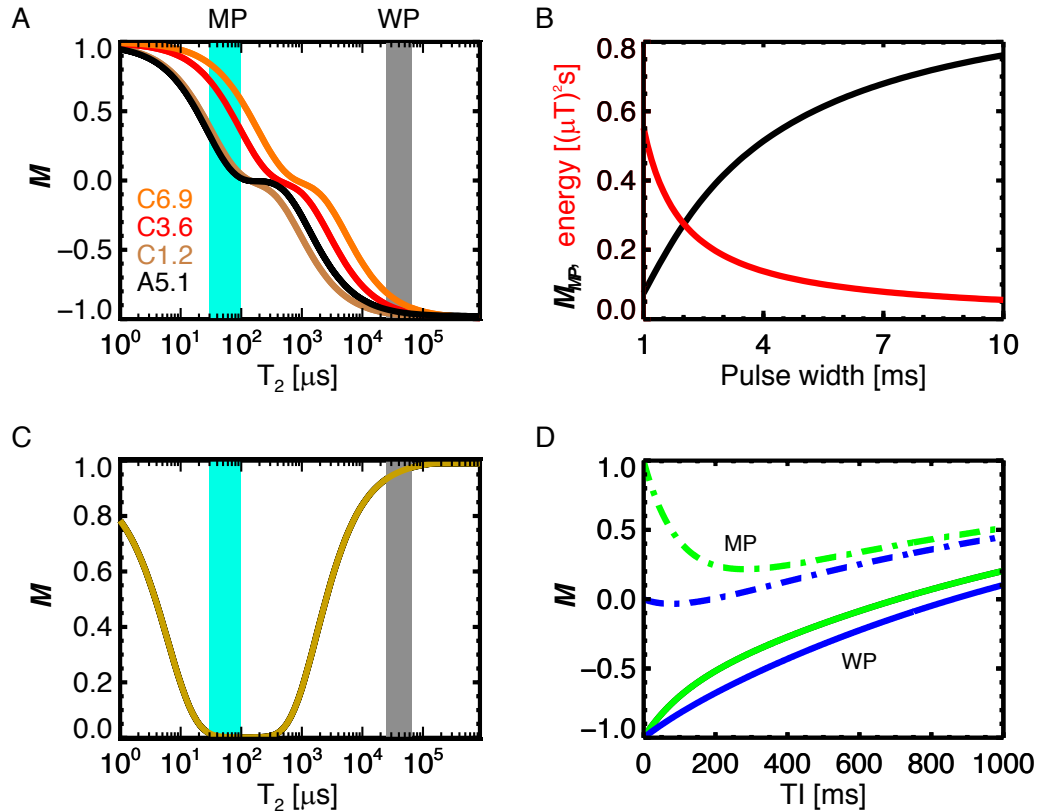
Figure 3.3 Simulated effect of IR pulses (a,b,d) and MT pulse (c) on longitudinal magnetization (M). **A**: Effect of inversion pulse on M as a function of T_2. While different inversion pulse types similarly invert long T_2 species characteristic of WP (grey band), they differentially affect the short T_2 MP (blue band). **B**: For MP ($T_2 = 70\mu s$), magnetization (black) after a composite inversion pulse and the latter's energy (red) depend strongly on pulse duration **C:** Effect of MT pulse on M as a function of T_2. Nearly complete saturation (M~0) is achieved for MP, while WPs are minimally affected. **D**: Calculated MP (dashed lines) and WP (solid lines) magnetization following inversion, as function of (TI) time, for two extreme cases: no MP saturation (green), and complete MP saturation (blue). Parameters for this simulation were taken from mean 7 T values of Table 3.2. Perfect WP inversion was assumed.
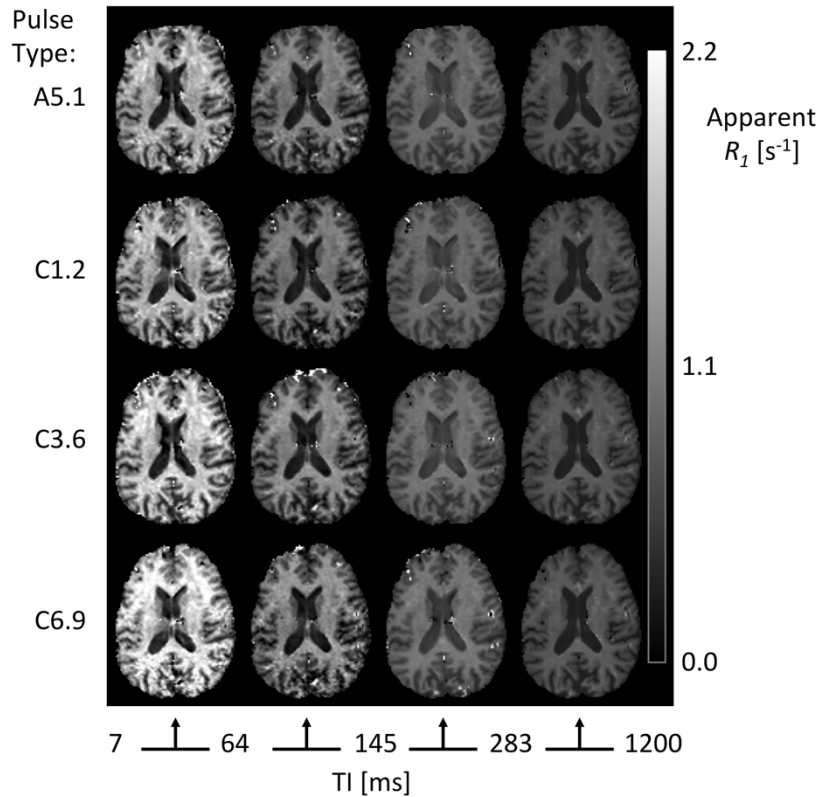
Figure 3.4 Effect of inversion pulse type (rows) on apparent (instantaneous) R_1 (scale in seconds), at increasing TI (columns). Apparent R_1, as calculated from adjacent TI's, was highest for lowest power composite pulse (C6.9) and short TI.

The effect of noise and finite TR on parameter fitting

To gain some insight into the stability of the two-pool model fitting procedure under influence of noise, noise was added to a synthetic signal recovery curve (using Eq. 3.1) generated based on subject averaged model parameters extracted with the ROI-based fitting procedure (Table 3.2). The noise level was determined from the experimentally determined ROI-based fitting residue and corresponded to a SNR of 500:1 in the ROI-averaged signal. After each of 100,000 realizations of noise addition, the data was subjected to the ROI-based fitting procedure (Fig. 3.2), after which the SD of the extracted parameters was determined.

67
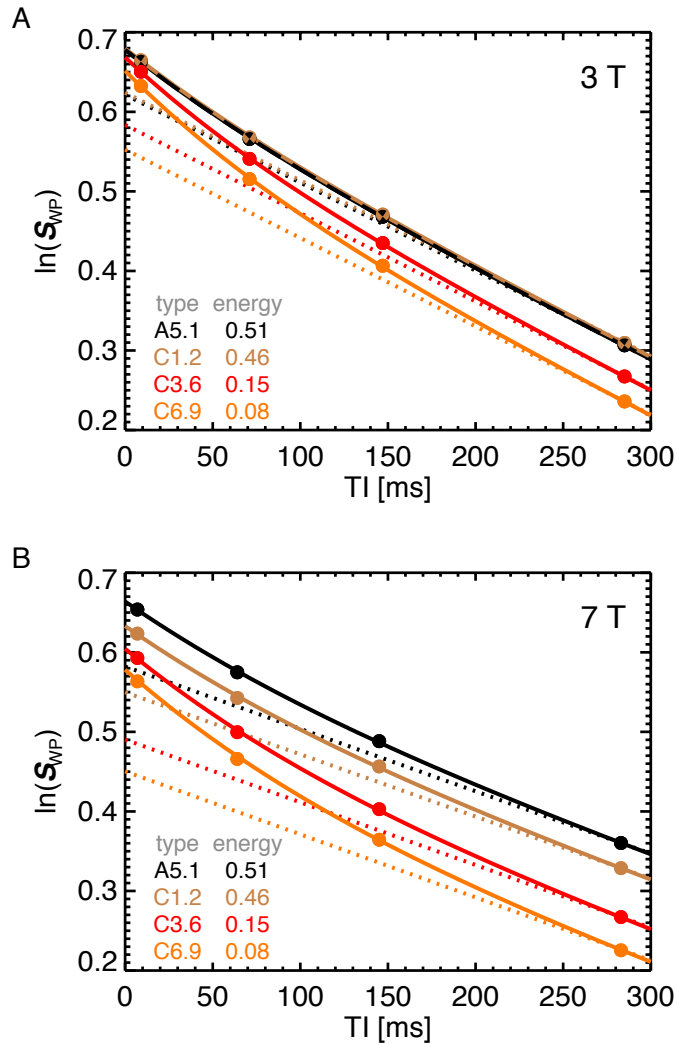
Figure 3.5 Demonstration of bi-exponential IR, based on measured and fitted S_{WP} in corpus callosum ROIs at 3 T (**A**) and 7 T (**B**). Subject and ROI-averaged IR data are shown in range of 0-300ms, where strongest effects of the bi-exponential nature of the decay is observed. The dashed lines are the single-exponential fits to the two longest TI's (283 and 1200 ms). Deviation form linearity (i.e. from single-exponential behavior) is strongest at early TI's and low-power pulses (C3.6 and C6.9) at 7 T. At 3 T, the adiabatic (A5.1) and shortest composite pulse (C1.2) produced virtually identical results.

To investigate the influence of the finite TR and incomplete magnetization recovery between scan repetitions on the extracted parameters, the evolution of the magnetization in the IR and MT experiments was simulated, again based on the experimentally determined two-pool model parameters (k, f, and R in Table 3.2). This

was done both for the actual TRs used in the experiments (4 s and 3 s for IR and MT)
respectively), as well as for a TR of 12 s at which complete recovery was assumed. Both
conditions were subjected to the ROI-based fitting procedure and the resulting parameter
values were compared.

3.6 *MT related parameters and bi-exponential recovery of T_1*

Initial evaluation of the effect of inversion pulse type on T_1 relaxation was
performed with simulations. Fig. 3.3a shows the effect of the each of the experimentally
used inversion pulses on M as a function of T_2. While all inversion pulses nearly fully
invert the long T_2 WP ($T_2 > 20$ ms), a highly variable saturation is observed for T_2 values
typical of MP (60-100 μs for Lorentzian lineshape, which has linewidth equivalent to 10-
15 μs Superlorentzian). The increasing saturation of MP (i.e. $FS_{MP}(0)$) with decreasing
inversion pulse duration is attributed to the increased pulse energy (Fig. 3.3b). The T_2
dependence of the saturation efficiency of the MT pulse (Fig. 3.3c) indicates almost
complete saturation for MP and negligible saturation for WP. Simulation of the effect of
variable MP saturation of the inversion pulse on IR characteristics shows an increasingly
bi-exponential recovery with reduced MP saturation (Fig. 3.3d). As a result, a relatively
high relaxation rate at the initial part of the recovery curve is observed.

Results of the experimental investigation into the effect of inversion pulse
characteristics on T_1 relaxation are summarized Figs. 3.4-3.6, and Tables 3.1 and 3.2. In
brief, a bi-exponential recovery is observed that is dependent on pulse type, consistent
with the notion that increasing pulse energy leads to a higher $FS_{MP}(0)$. As illustrated in
Fig. 3.4, following WP inversion, the initial (apparent) relaxation rate is increased
compared to the rate at longer TI, and this is dependent on pulse type. Between 7 and 64

ms after the inversion, rates in excess of 2 s^{-1} are observed for the lowest energy pulse (6.9 ms composite pulse), which is about twice the rate observed at the long TI's in our experiments, and in previously published work (33). This observed behavior is consistent with the notion that the decay for the shorter TI's is accelerated by the initially large difference in MP and WP magnetization ($FS_{MP}(0) << FS_{WP}(0)$), resulting in strong MT effects. This is further exemplified in Fig. 3.5, showing IR data from the corpus callosum ROI together with single- and bi-exponential fits. A clear deviation from single exponential relaxation is observed at short TI, which again is strongest for the lowest energy inversion pulse and high field (7 T). The vertical offset of the curves is attributed to variable WP inversion efficiency, which is particularly pronounced at 7 T (see Table 3.1 for estimated inversion efficiency).
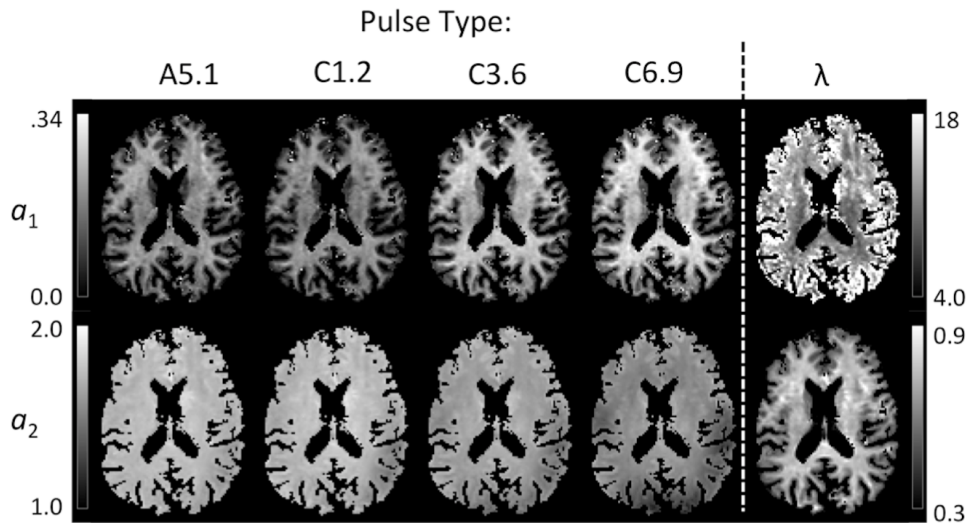
Figure 3.6 Example of voxel-wise fitting of bi-exponential relaxation behavior. Shown are results for a single slice in a single subject at 7 T. The contribution of the fast component (represented by a_1) increases with increasing pulse length for composite pulses C1.2-C6.9 (decreasing energy). The voxels with CSF where masked out from the images, as their fits resulted in extreme values for some of the parameters due to a close to single-exponential nature of IR in CSF.

Further analysis focused on two-pool model fitting based on the procedures outlined in Figs. 3.1 and 3.2. First, bi-exponential fitting was performed to the MT and inversion data (Step 1 in Fig. 3.1). An example of the extracted values for amplitudes (a_1 and a_2) and rates ((λ_1 and λ_2) of the two exponential components is shown in Fig. 3.6. The relative values of a_1 and a_2 varied strongly with inversion pulse type, with that of the rapidly relaxing component a_1 increasing with lower pulse energy. This was particularly apparent in WM, consistent with its higher MP fraction. The slowly relaxing component amplitude (a_2) varied little over the brain, indicating an efficient inversion. Exceptions were areas of in the posterior brain, attributed to off-resonance effects.

Table 3.1 Pulse-dependent results of two-pool fitting in corpus callosum white matter of IR experiments at 3 T and 7 T (n=10). Reported are subject averages (and SD's) of amplitudes (a_1 and a_2) and saturation levels assuming f =0.27 (based on MT data). Pulse energy is integral of B_1^2 in units of $(\mu T)^2 s$. Range indicates theoretically possible values for all possible effects of inversion pulse on MP, while assuming a 100% inversion of WP.

B_0	Type	Energy	a_1	a_2	FS_{MP}	FS_{WP}
3 T	A5.1	0.51	0.116 (0.009)	1.854 (0.008)	0.87	1.97
	C1.2	0.46	0.113 (0.010)	1.860 (0.009)	0.89	1.97
	C3.6	0.15	0.170 (0.011)	1.781 (0.011)	0.62	1.95
	C6.9	0.08	0.194 (0.013)	1.725 (0.015)	0.48	1.92
	range (theory)		0.08-0.30	1.92-1.71	0.0-1.0	
7 T	A5.1	0.51	0.173 (0.012)	1.769 (0.010)	0.87	1.94
	C1.2	0.46	0.170 (0.012)	1.714 (0.044)	0.84	1.88
	C3.6	0.15	0.225 (0.016)	1.605 (0.047)	0.56	1.83
	C6.9	0.08	0.245 (0.026)	1.538 (0.052)	0.46	1.78
	range (theory)		0.16-0.40	1.84-1.60	0.0-1.0	

Figs. 3.7a and b illustrate the extraction of global $R_{1,MP}$ and $R_{1,WP}$ values based on constraints on $FS_{MP}(0)$, for 3 T and 7 T data respectively (see also Fig. 3.1). Maximizing the number of voxels satisfying this constraint (indicate by the shaded area in the top right corner of each figure) led to an $R_{1,MP}$ estimate of 4.0 s^{-1} and 2.0 s^{-1} at 3 T and 7 T respectively, while $R_{1,WP}$ values were 0.40 s^{-1} and 0.35 s^{-1}. Based on the sensitivity of the $FS_{MP}(0)$ distribution to changes in the $R_{1,MP}$ value, the $R_{1,MP}$ error margin can be estimated to be about 10%, while that for $R_{1,WP}$ was estimated at 20%.

Quantitative results of bi-exponential fitting and parameter extraction based on the ROI-based analysis (outlined in Fig. 3.2) are summarized in Tables 3.1 and 3.2. Table 3.1 shows subject-averaged values for pulse type-dependent parameters a_1, a_2, $FS_{MP}(0)$, and $FS_{WP}(0)$, confirming the decreased $FS_{MP}(0)$ and increased contribution of the rapidly relaxing component for low energy inversion pulses. This trend was strongest for the 7 T data, which is attributed to the lower $R_{1,MP}$ at this field strength. Subject- and ROI-averaged values for parameters considered common to all pulse types (i.e. λ_1, λ_2, $R_{1,MP}$, $R_{1,WP}$, k_{WM}, k_{MW}, and f) are shown in Table 3.2. As indicated above, $R_{1,MP}$ was taken from the voxel-wise analysis, whereas $R_{1,WP}$ was fine-tuned based on ROI-averaged signals. Changes in $R_{1,WP}$ with fine-tuning were within 20% of the original values. Note that although k and f values are expected to not depend on field strength, appreciable differences in k-values were observed. This suggests that the experimental data are not fully described by our model.

Results of the noise simulations that evaluated the stability of the fitted parameters are shown in Table 3.3. These results indicate a precision that was for most parameters about 3%, with 7 T data generally showing smaller values compared to 3 T

data. Note that the precision of $R_{1,WP}$ in this analysis is substantially better than the margin estimated in the voxel-wise analysis (for estimation of the global values for $R_{1,MP}$ and $R_{1,WP}$). This suggests that the accuracy of $R_{1,WP}$ is limited by the accuracy of $R_{1,MP}$, rather than by the noise (or inter-subject variations, judging from the low SD over subjects reported in Table 3.2).

Simulations of finite TR (incomplete signal recover between repeated measurements) on extracted parameter values showed relatively minor effects (Table 3.4). Strongest effects were observed at 7 T, as expected based on the slower T_1 recovery. Finite TR resulted in an underestimation of λ_1, and an overestimation of λ_2. As a result $R_{1,WP}$ was overestimated, while k_{WM} was underestimated. Little effect on f was observed.

Table 3.2 The average (SD) of extracted two-pool model parameters (using Eq. 3.1-3.4) in corpus callosum ROI (n=10), $R_{1,MP}$ is reported without SD as a single value was assumed for all subjects; all rates are reported in s^{-1}.

B_0	λ_1	λ_2	f	$R_{1,WP}$	$R_{1,MP}$	k_{WM}	k_{MW}
3 T	12.11 (0.83)	1.103 (0.034)	0.265 (0.014)	0.410 (0.027)	4.0	2.39 (0.26)	6.61 (0.64)
7 T	9.25 (0.68)	0.773 (0.016)	0.268 (0.013)	0.406 (0.018)	2.0	2.04 (0.15)	5.58 (0.54)

Table 3.3 Noise simulation results: the SD (absolute and relative percentage) of fitted and derived parameters for simulated data with baseline (ROI) SNR of 500 (based on the R^2 of the actual fit results), all rates are in units of s^{-1}.

B_0		a_1,a_2	λ_1	λ_2	f	$R_{1,WP}$	k_{WM}	k_{MW}	$FS_{MP}(0)$
3 T	SD	0.0035	0.32	0.0025	0.0054	0.014	0.069	0.26	0.032
	%		2.8	0.23	2.7	3.5	3.3	4.6	3.2
7 T	SD	0.0035	0.21	0.0021	0.0036	0.0067	0.052	0.17	0.022
	%		2.3	0.25	1.8	1.9	2.5	3.0	2.2

Table 3.4 Comparison the fitting results from simulations (based on the parameters printed in Table 3.2) run with the experimental TR and a TR four times as long, all rates are in units of s^{-1}.

B_0	TR	f	$R_{1,WP}$	k_{WM}	k_{MW}
3 T	12,9	0.271	0.363	2.39	6.45
	4,3	0.270	0.391	2.33	6.32
7 T	12,9	0.268	0.405	2.04	5.56
	4,3	0.262	0.455	1.85	5.21

The presence of a second, rapidly relaxing component to T_1 relaxation can interfere with attempts to quantify T_1 relaxation based on the conventional assumption that the inversion recovery is single-exponential. This is particularly true at short TI, as is strikingly apparent from the instantaneous T_1 shown in Fig. 3.8. Therefore, when quantifying T_1 relaxation assuming single-exponential behavior, it may be advantageous to exclude the recovery at short TI. Simulations show that for T_1 to be within 95% of $1/\lambda_2$ (i.e. for the instantaneous T_1 to stabilize), the minimum TI would need to be between 176 and 299 ms at 3 T, and between 324 and 443 ms at 7 T, with lower and upper values reflecting maximal and minimal MP saturation respectively.

Figure 3.7 (next page) Voxel-wise analysis approach to extract global values for $R_{1,WP}$ and $R_{1,MP}$. Contour plots of 2D histograms show the distribution of calculated $FS_{MP}(0)$ values for IR (horizontal axis) and MT data (vertical axis). Histograms were calculated for a range of R_{1WP} and R_{1MP} values (columns and rows respectively, values in s^{-1}), and reflect all voxels in all subjects at 3 T and 7 T (**A** and **B** respectively). The dashed lines in each histogram show the range of expected $FS_{MP}(0)$ values (both $FS_{MP,Inv}(0)$ and $FS_{MP,MT}(0) <1.0$ and $0.7 < FS_{MP,Inv}(0) / FS_{MP,MT}(0) < 1.0$; the area is indicated with shading in top right plots). The numbers printed in the plots are the fractions of the number of brain voxels falling within the expected range (see also Fig. 3.1). The histogram with the highest fraction (in red) was identified to deduce the appropriate values for $R_{1,WP}$ and $R_{1,MP}$ for each field strength.

A) $S_{MP}(0)$ distribution as function of global R_{1WP} and R_{1MP}, 3 T

B) $S_{MP}(0)$ distribution as function of global R_{1WP} and R_{1MP}, 7 T
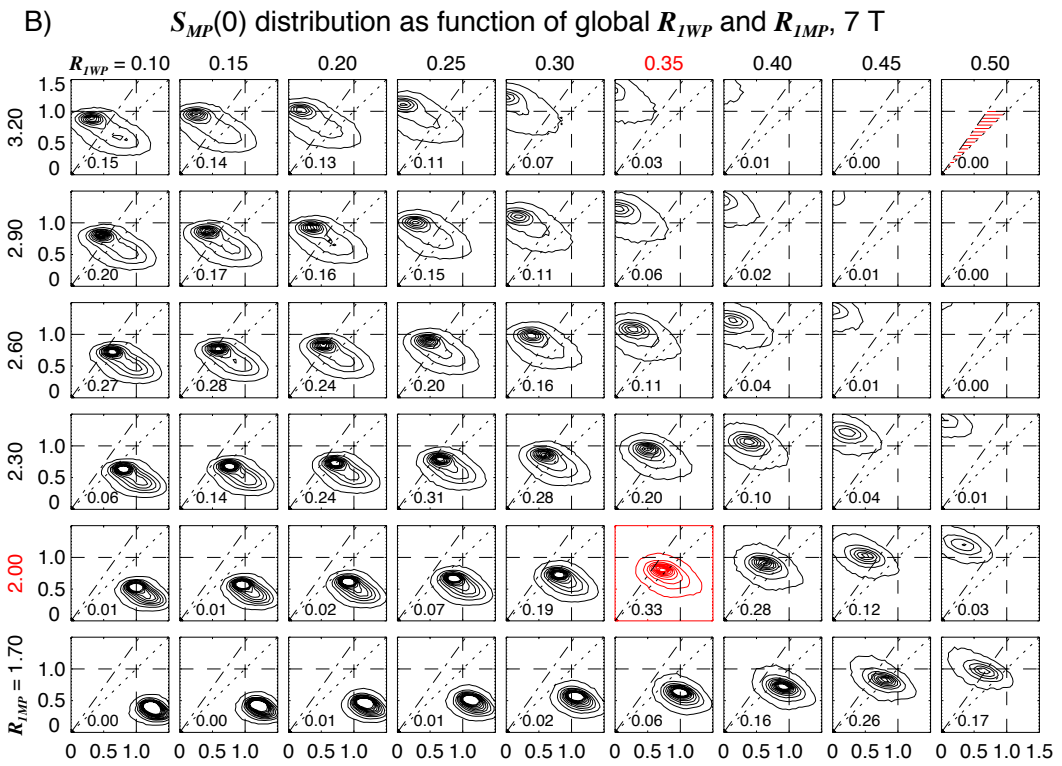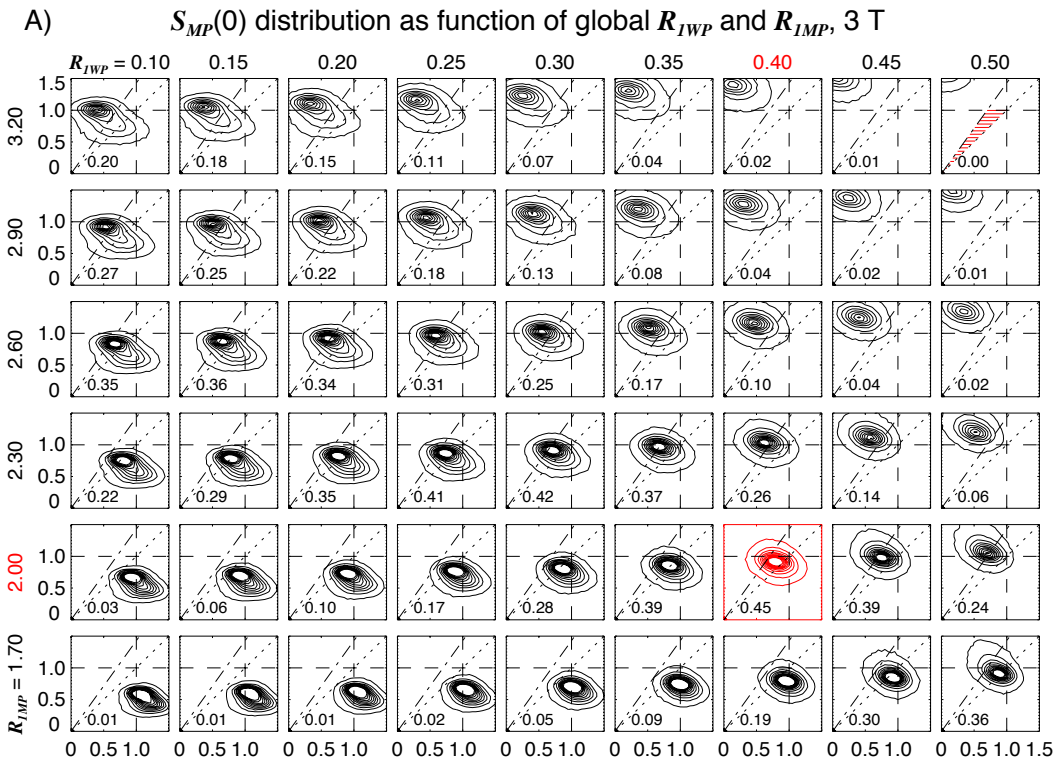
3 .7 Discussion and comparison with previous on T_1 relaxation and MT

The experiments described in this work demonstrate a dependence of IR on the parameters of the RF inversion pulse. Specifically, a bi-exponential recovery was observed, in which the amplitude of the rapid component depended on the power of the RF pulse. This finding is consistent with the notion that this component originates from MT between WP and MP, whose magnetization difference resulting from the inversion pulse is expected to depend on RF pulse energy. Simulations of the effects of the inversion pulses used in this work indeed indicated a highly variable magnetization difference between WP and MP.

Previous studies have recognized the potential contribution of MT to bi-exponential signal recovery after inversion of WP magnetization, and were able to explain experimental IR data with a two-pool model of MT between WP (47–49,77). The RF energy dependence of the recovery observed in the current study further solidifies this notion. In addition, the analysis presented here further characterizes the contribution of MT by comparing inversion recovery data with MT data. Use of the known MP saturation resulting from the MT pulse, and assuming $R_{1,MP}$ and $R_{1,WP}$ constant over the brain, allowed full characterization of MP and WP magnetization recovery and extraction of the two-pool model parameters. The resulting estimates for f in corpus callosum were, as expected, virtually identical for 3T and 7 T (0.266 versus 0.268) and consistent with what would be expected based on the close to 30% fraction of proteins and lipids (and hence an approximately MP fraction of 30%, considering that the hydrogen proton fraction in proteins and lipids is similar to that in water) (36,80). Our estimates furthermore appear consistent with previous MRI measurements of proton density not

relying on MT contrast, which found WM water content to be around 70% (81,82,123,126). Nevertheless, our estimate of f is somewhat higher than previous MT studies (40,90,93,94,109). While this may, in part, be due to incorrect values for $R_{1,MP}$ assumed in these studies (11), and their different approach for MT contrast generation, the reasons for this discrepancy remain poorly understood and require further investigation.

In this study, significant efforts were made towards estimation of $R_{1,MP}$, because of its importance in quantification of MT and T_1 relaxation. In our approach, both $R_{1,MP}$ and $R_{1,WP}$ and were assumed to be constant over the brain, which likely is inaccurate considering the diversity in molecular structure in brain tissues and the potential contribution of paramagnetic species (e.g. iron) to T_1. Nevertheless, our values of 4.0 and 2.0 s^{-1} for $R_{1,MP}$ at 3 T and 7 T respectively are in the range of average values of between 2-5 s^{-1} reported for membrane model systems at fields from 8 T down to 1 T (37,56,127) or 2.3-6 s^{-1} derived from the dependence of R_1 on f at fields ranging from 7 T down to to 1.5 T (11,28,33,123,124).

Among the parameters extracted with the presented analysis is k_{WM} (and related parameter k_{MW}) representing the MT rate between WP and MP. Values of between 2.4 and 2.0 s^{-1} were found in the corpus callosum ROI at 3 T and 7 T respectively, which is on the low end of the 2.5-4 s^{-1} range reported in literature (45,90,109,113). In part, this may be related to methodological differences. In this regard, it should also be noted that k_{WM} represents an aggregate of processes that may contribute in varying amount between different methods: these include spin diffusion (38,128), MT between MP and WP in myelin water, and MT between myelin water and water in other compartments. This may

77

also explain the (small) differences seen in our 3 T and 7 T values. A slight underestimation of k_{WM} also appeared likely resultant from the finite TR used in our experiments (Table 3.4).

The finding of a bi-exponential T_1 recovery and its origin in MT effects has important implications for T_1-weighted MRI, in particular when reproducible contrast and accurate recovery rates are required. Bi-exponential fitting of MRI data acquired at a number of TI values would be one way to address this issue. As demonstrated above, this leads to T_1 estimates (from the slow component, i.e. λ_2^{-1}) in corpus callosum white matter of 905±27ms and 1293±28ms for 3 T and 7 T respectively (See Table 3.1), which both are somewhat higher than reported previously (for overview see (33)). However, this type of fitting is notoriously difficult to do, as signal to noise ratio is often limited and only few TI values are sampled. Fortunately, in human brain, the rate constants (λ_1, λ_2) differ substantially, with λ_1 being much higher than λ_2. Thus, at TI values much larger than λ_1^{-1}, the recovery can be characterized by a single-exponential function with rate constant λ_2, which then can be interpreted as an apparent R_1 value. This is further illustrated in the simulations shown in Fig. 3.8, indicating the minimum TI values at which the apparent (instantaneous) T_1 becomes independent of TI. This conclusion was also reached in a very recent paper investigation bi-exponential relaxation (129). The effects of bi-exponential relaxation in IR experiments can be further minimized by the use of high-power adiabatic inversions that fully invert WP and fully saturate MP. Under this condition, contribution of the fast component is smallest and least variable. In alternative (non-IR) techniques for T_1 quantification, such as mcDESPOT (121), MT may be a confound (130), and its contribution will depend on experimental parameters.
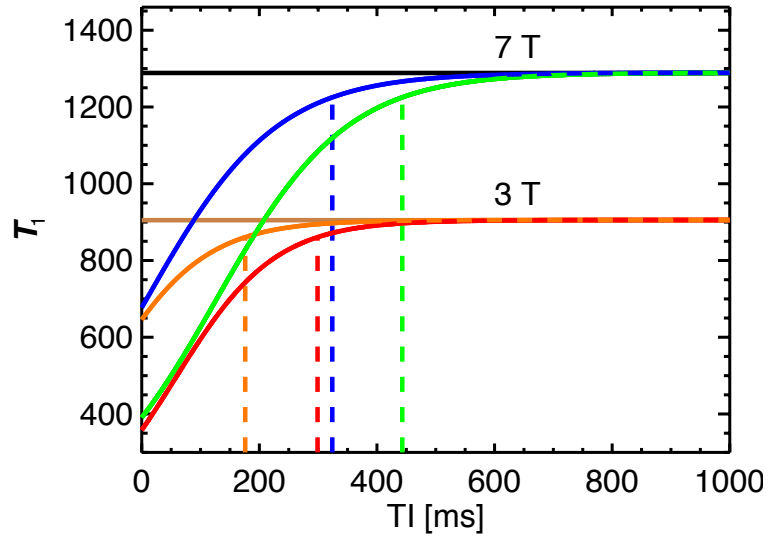
Figure 3.8 The instantaneous T_1 $(= -S(t)/(\frac{dS(t)}{dt}))$ calculated from two-pool model simulated data (using the average parameters from Table 3.2), for the minimum and maximum effects (high- and low-power inversion) (red/orange= 3 T, green/blue 7 T, orange/blue minimum effect, red/green maximum). The vertical lines indicate the minimum TI for an error smaller than 5% in the calculated (single-exponential) T_1.

In addition to affecting quantification, variable MP saturation can have influence on the contrast in T_1-weighted MRI and techniques that use inversion pulses for tissue suppression, and these effects extend beyond TI times indicated above (i.e. around 300 and 440 ms for worst cases, i.e. minimal MP saturation at 3 T and 7 T respectively). Examples of the latter are the use of double inversion recovery to selectively image grey or white matter (131), IR–based myelin imaging using ViSTa (132). For consistent results, optimization of TI values ideally would take into account the power of the RF inversion pulse. As shown in Fig. 3.3d, the zero crossing of the IR curves depends on the MP saturation level and therefore on the applied RF energy. Of course, such optimization would not be sufficient to account for variations in f.

As indicated above, the contribution of the rapidly relaxing component to the inversion recovery is, aside from f, dependent on RF pulse parameters, and field strength.

The latter dependence originates from the effect of field strength on $R_{1,MP}$: a_1 increases with decreases in $R_{1,MP}$ at higher field in the complicated fashion indicated by equations (1-4). Thus, at fields above 7 T, contribution of the fast component should further increase. Together with the increase in SNR available at high field, this would improve determination of a_1, a_2, λ_1, and λ_2, and potentially allow robust quantification of MT exchange rates (k_{MF} and k_{WF}) from IR data only, without the need for dedicated MT experiments. Conversely, at 1.5 T, the deviation from single-exponential inversion recovery is expected to be smaller.

Although our analysis of T_1 relaxation assumed a dominant contribution from MT, it should be realized that in some brain regions, paramagnetic species such as iron may contribute as well. For example, in the iron-rich grey matter of the globus pallidus, this may increase the relaxation rate by as much as 0.3 s^{-1} at 7 T (33). This complicates the extraction of parameters such as f and k_{WM} from the bi-exponential fit, which may require additional information (e.g. estimates of local iron content based on R_2^* data).

A few limitations of the current study deserve further attention. One limitation is the assumed efficiency of MT pulses, which was based on experimental variation of pulse duration. This implicitly assumed a narrow distribution of T_2 values for the MP pool. However, it is possible that a fraction of MPs escape saturation, due to an either very short or very long T_2. This would then lead to an underestimation of f. Judged from the similarity between fitted R_{1WP} found by either assuming fixed MT efficiency (in the ROI analysis) or fixed (global) $R_{1,WP}$ (in the voxel-wise analysis), this appeared not to be a major issue. Another limitation is the sensitivity of multi-exponential fitting and parameter extraction to measurement noise. The SD value of some of the ROI-derived

parameters reached 5% even is the presence of a high (500:1) SNR. This is attributed to the inherent difficulty of the fitting problem, combined with temporal instabilities (caused by e.g. head motion). Finally, the limited accuracy of the R_{1MP} value also limits the accuracy in other derived parameters, in particular R_{1WP} and the k_{MW}.

Chapter 4: Study of Magnetization Transfer and Macromolecular Proton T_2 in Marmoset Brain

One way to study MP T_2 is to measure the dependence of MP saturation on the B_1 amplitude of an RF pulse, and compare it with the Bloch equations simulation (Fig. 4.2). A large range of B_1 values for the RF pulses is needed to reliably simulate the B_1 dependence of saturation effects on MPs to infer T_2. This is attempted by studying marmoset brains *in vivo* using MRI, in which case the application of RF pulses with high B_1 (up to 2000 Hz in this study) is possible. However, use of such a high B_1 is not feasible *in vivo* human studies, due to the restriction on specific absorption rate (SAR) and the limited instrument capability of the human MRI scanners. This work is partially adapted from our conference abstract (3).

4 .1 *Importance of determination of the MP T_2 for MT applications*

Magnetization Transfer (MT) contrast has been used to study brain myelination and relies on selectively saturating semi-solid protons (often referred to as macromolecular protons (MPs) in literature) based on their rapid T_2 relaxation. Optimization of this selectivity and quantification of MT contrast requires knowledge of the macromolecular proton T_2, which has proven difficult to measure. The range of reported estimates (10 to 60 μs (35,59,60,63,75,96,113)) is rather large, likely due to differences in experimental conditions, measurement method and sample type. The lack of knowledge about MP T_2 and the large uncertainty in determination of it often lead to inaccurate assumptions on response of MPs to RF pulses in MT applications (45,50) and may result in wrong estimation of MP fraction (11). With the goal of optimizing the measurement of the MP

fraction using MT experiments (45,50,74), we set out to study the MT-related parameters and further determine the MP T_2, in white matter, grey matter and muscle in marmosets *in vivo*.

4 .2 *Two-pool exchange model and MRI measurements*

One *in vivo* scan of a common marmoset (*Callithrix jacchus*) was performed on a Bruker 7 T scanner. In order to study MT without CEST and direct WP saturation effects, we followed a recent approach based on monitoring the saturation of WP signal following a brief, 2 ms MP saturation pulse (1,2). The effect of a binomial saturation recovery (SR) pulse (133) on MP magnetization was studied as a function of post-saturation delay t (measured from the center of the pulse) using a multi-gradient echo sequence, after which the amplitude of the saturation effect and its dependence on SR pulse amplitude were calculated and compared with simulated values to determine MP T_2. First, experiments were performed to determine parameters describing MT kinetics, assuming a two-pool model of exchange between MPs and WPs (defined as Experiment I), and subsequently, MP T_2 was investigated by studying the magnitude of the MP saturation effects as a function of B_1 amplitude of the MP saturation pulse (defined as Experiment II).

Two-pool model

Following an initial RF pulse that differentially saturates the WP and MP pools, we assume that the fractional saturations of the two pools, FS_{WP} and FS_{MP}, experience bi-exponential evolutions as described in Eqs. 1.12-1.13 (1,2,76).

Experiment I: Determination of MT parameters

To measure the parameters related to the two-pool exchange model, two types of preparation pulses, namely a WP IR pulse and a composite broadband MP SR pulse were used to saturate the two pools to different extents. After variable delay t, MGRE image acquisition was performed to sample $FS_{WP}(t)$. The use of two different preparation pulses facilitated fitting λ_1 and λ_2, and furthermore allowed extraction of k_{MW}, k_{WM}, f, and $R_{1,WP}$ by assuming $R_{1,MP} = 2$ s^{-1} and $FS_{MP}(0) = 1.0$ for the SR experiments, the later of which was determined by simulations using the Bloch equations (Fig. 4.2), based on the reported T_2 values, 10-60 μs (35,59,60,63,75,96,113). The inversion pulse was a hard pulse, with pulse duration of 0.5 ms, B$_1$ (amplitude of the RF field) of 2000 Hz (1 Hz equals 0.0235 μT). The SR pulse had a duration of 2 ms and consisted of a train of hard pulses with angles 45°, -90°, 90°, -90°, ..., -90°, 45°, the number of pulses and B$_1$ amplitude were 17 and 2000 Hz respectively.

Experiment II: Determination of MP T_2

To determine MP T_2, the SR pulse was repeated using different combinations of number of pulses and B$_1$ amplitudes, including 3 & 250 Hz, 5 & 500 Hz, 9 & 1000 Hz, 13 & 1500 Hz, with the same pulse duration of 2 ms and a train of variable number of hard pulses with angles 45°, -90°, 90°, -90°, ..., -90°, 45°.

Image acquisition

For both IR and SR experiments, image data were acquired using MGRE, sampling a single slice after the preparation pulse. The delay times for the IR experiment were 1.5, 50, 200, 400, 800 and 1200 ms (defined as the time from the center of the inversion pulse to the center of the MGRE excitation pulse). The delay times for the SR experiments in *Experiment I* were: 2.2, 49, 99, 199, 399 and 799 ms and for SR experiments in

84

Experiment II were: 2.2 and 99 ms. The IR and SR delay times in *Experiment I* were chosen to sample the signal recovery dynamics. The image resolution was 0.28mm. The echo time (TE) was 2.4 ms, and TRs were 3 s for all IR and SR experiments. For all IR and SR experiments, only one measurement were performed, one reference signal was acquired by the preparation pulse to provide to estimate $M_{WP}(\infty)$, and allow conversion of the measured signals to $FS_{WP}(t)$, in Eq. 1.12.

Pre-processing

Pre-processing included signal polarity correction, and calculation of $FS_{WP}(t)$. Polarity correction was needed only for IR (magnitude) data, because of signal rectification during the complex-to-magnitude conversion. It was performed based on the phase difference between the IR images with the (un-inverted) reference image. The $FS_{WP}(t)$ level expressed in Eq. 1.12 was determined by dividing each IR image by the corresponding reference image (i.e. data acquired without preparation pulse). Analogous analysis was performed for the SR data, however without performing the signal polarity adjustment. All processing was done in IDL (Exelsis Visual Information Solutions, Boulder, CO, USA).

ROI selection

Regions of interest were selected in white matter, grey matter, and muscle respectively, as illustrated in Fig. 4.1d.

Dependence of MP saturation on B_1 of SR pulses

To determine λ_1, λ_2, k_{WM}, k_{MW}, and $R_{1,WP}$, both the IR and the SR data from *Experiment I* were analyzed on a voxel-wise basis. Defining $FS_{MP}(0, B_1)$ as the $FS_{MP}(0)$ created by a SR pulse with a specific B_1 in *Experiment II*, $FS_{MP}(0,B_1)$ can be then

calculated based on analysis of the SR data in *Experiment II*. The following steps were involved:

[1] Fit Eq. 1.12 to the IR and SR data in *Experiment I* jointly, yielding one pair of decay rates (λ_1, λ_2) and two pairs of amplitudes (a_1, a_2) for each voxel.

[2] Assuming $R_{1,MP}=2$ s^{-1} (2) and $FS_{MP}(0)$ for the SR experiment in *Experiment I* to be 1.0 as discussed above, calculate k_{WM}, k_{MW}, $R_{1,WP}$, using Eqs. 1.10 & 1.14, based on the decay rates and amplitudes found under Step [1].

[3] Fit Eq. 1.12 to the SR data from *Experiment II*, to find a pair of amplitudes $(a_1(B_1), a_2(B_1))$ for every voxel at each B_1, using decay rates (λ_1, λ_2) found under Step [1]. Then calculate $FS_{MP}(0,B_1)$ using these $(a_1(B_1), a_2(B_1))$ pairs, according to Eq. 1.13 by setting $t{=}0$ s, with all other parameters known from Steps [1] and [2], as shown in Eq. 4.1.

$$FS_{MP}(0, B_1) = \frac{a_1(B_1)(-\lambda_1+k_{WM}+R_{1,WP})}{k_{WM}} + \frac{a_2(B_1)(-\lambda_2+k_{WM}+R_{1,WP})}{k_{WM}} \qquad (4.1)$$

Determination of MP T_2 in three ROIs

This estimate of $FS_{MP}(0,B_1)$ was then averaged over each ROI and compared with the simulated dependence of longitudinal magnetization (after the SR pulse) on T_2 and B_1 (Fig. 4.2), assuming a single (average) T_2 of the MPs, obtained from simulations of the Bloch equations, to find T_2 for MPs in white matter, grey matter and muscle respectively.
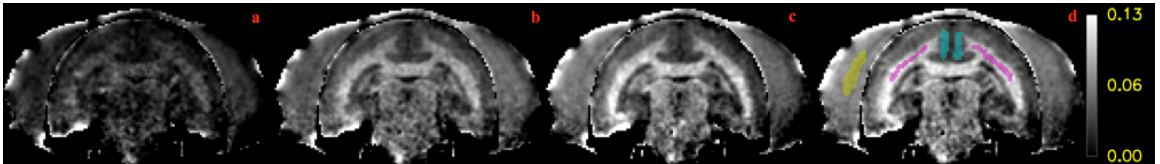
Figure 4.1 Fractional difference between images at two delays, divided by the reference image $(Im(t = 2.2 \text{ ms}) - Im(t = 99 \text{ ms}))/Im(Ref)$ for SR experiments with B_1 of 500 Hz(a), 1000 Hz(b), 1500 Hz(c), and 2000 Hz(d); (d) show the ROI's in WM (purple), GM (cyan), and muscle (yellow).
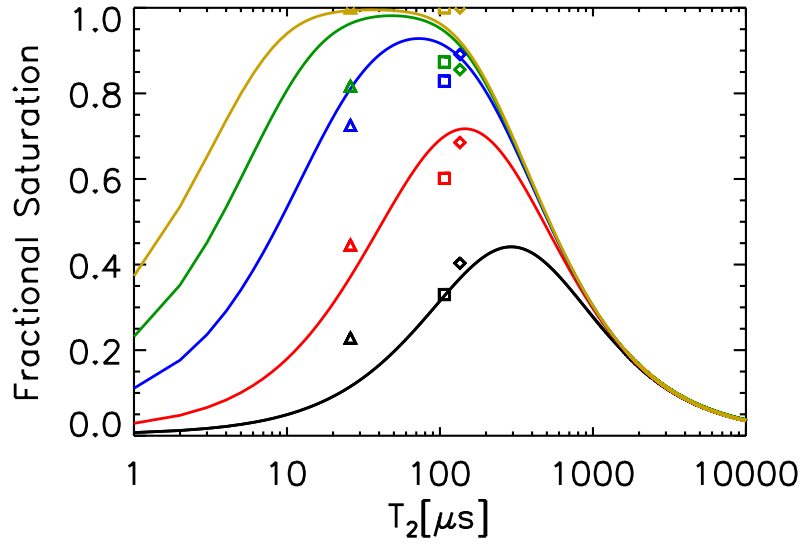
Figure 4.2 Lines show the fractional saturation created by a SR pulse as function of T_2 for five different combinations of number of hard pulses and B_1: 3 & 250 Hz (black), 5 & 500 Hz (red), 9 & 1000 Hz (blue), 13 & 1500 Hz (green), and 17 & 2000 Hz (gold) with the same pulse duration of 2 ms, simulated using the Bloch equations. Fitting these simulated fractional saturations to those measured in WM (square symbols), GM (diamond symbols) and muscle (triangular symbols) ROI's, resulted in MP T_2 of 107, 135 and 26 μs respectively.
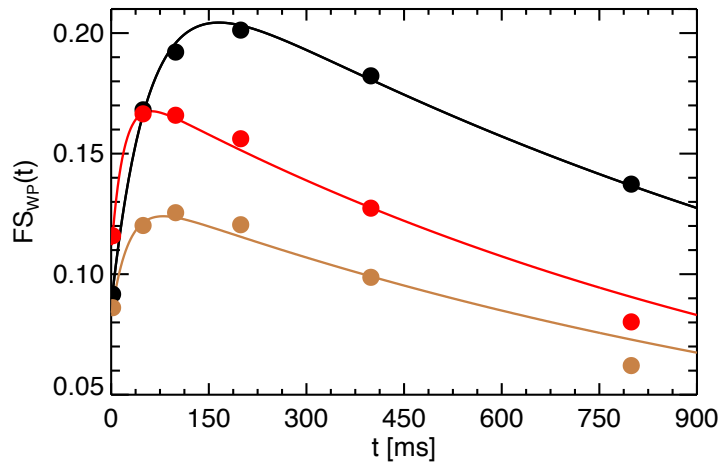
Figure 4.3 Twop-pool model fitting (shown in lines) to ROI averaged $FS_{WP}(t)$ (shown in dots) for the SR experiments in *Experiment I*, in WM (black), GM (brown) and muscle (red).

Table 4.1 Fitting results for two-pool exchange model parameters averaged within each ROI; $R_{1,MP}$ was taken as 2.0 s^{-1} as determined previously (2); R^2 was adjusted for degrees of freedoms.

	a_1(IR)	a_2(IR)	a_1(SR)	a_2(SR)	λ_1	λ_2	$R_{1, WP}$	f	k_{WM}	k_{MW}	R^2
WM	0.24	1.68	-0.15	0.24	17.39	0.70	0.45	0.18	2.73	12.92	0.999
GM	0.10	1.95	-0.041	0.076	37.65	0.77	0.69	0.059	2.08	33.64	0.989
Muscle	0.073	1.93	-0.051	0.11	52.64	0.87	0.76	0.081	4.11	46.62	0.981

Table 4.2 Results for fitting of MP T_2 and R^2 (adjusted for degrees of freedoms), for ROI's in WM, MG and muscle.

	WM	GM	Muscle
T_2 (µs)	107	135	26
R^2	0.89	0.93	0.90

4 .3 Extraction of MT related parameters and fitting of MP T_2

Fig. 4.1 shows the fractional difference between images at two delays ($Im(\Delta = 2.2\text{ms}) - Im(\Delta = 99\text{ms}))/Im(Ref)$ for different powers levels (500Hz, 1000Hz, 1500Hz, and 2000Hz). It shows the B_1 dependence of saturation effects, and stronger saturation effect can be achieved by increasing B_1, for up to 2000 Hz.

Voxel-wise fitting of the two-pool model (Eq. 1.12) to the IR and SR data allowed robust extraction of the model parameters. ROI averaged results are shown in Fig. 4.3 and Table 4.1. The ROI-averaged values for $R_{1,WP}$, f, and k_{MW} were similar to those found in recent *in vivo* studies on human brain based on similar methods at 7 T (1,2). Comparing the measured $FS_{MP}(0,B_1)$ (Eq. 4.1) with the simulated saturation effect on MPs based on Bloch equations, resulted in MP T_2 of 107, 135 and 26 µs in the ROI's of WM, GM and muscle respectively, as shown in Fig. 4.2 and Table 4.2.

4 .4 Discussion and comparison

This study proves that the SR pulse used here can selectively saturate MPs in brain within only 2 ms *in vivo*. This short pulse duration is advantageous for studying MT as it minimizes the confounding CEST effects, which relies on applying RF pulses with long durations (on the order of seconds) to saturate exchangeable protons (27) and would otherwise complicate interpretation. Further our simulation shows that by changing the number of sub-pulses, and B_1, one can change the saturation effects on MPs with short T_2 without altering WPs with long T_2, which can be appreciated from Fig. 4.2.

A potential source of error is the wrong assumption of $FS_{MP}(0)$. An improvement could be made by applying SR pulses with even longer pulse duration or higher B_1 to achieve complete saturation on MPs, for precise extraction of the two-pool exchange model parameters, which will be demonstrated in our study on a fixed marmoset brain *ex vivo* in Chapter 5. However, our experiments in this study were interrupted due to the failure of the receive RF coil. For the range of reported T_2 values, from 10 to 60 μs (35,59,60,63,75,96,113), Bloch equations simulation shows that $FS_{MP}(0)$ varies from 0.93 to 1.0, as can be seen from Fig. 4.2. By changing $FS_{MP}(0)$ to 0.93, the ROI averaged MP fractions change to 0.19 for WM, 0.064 for GM, and 0.088 for muscle, which have slight increase, compared to the case of assuming $FS_{MP}(0)$ as 1.0, as shown in Table 4.1. Therefore, the error in estimation of MP fraction induced by assumption of $FS_{MP}(0)$ is small.

However, by assuming $FS_{MP}(0)$ as 1.0, the estimated fractional saturation levels for SR experiments with B_1 of 250-1500 Hz (symbols in Fig. 4.2), can not reliably fit to the simulated saturation effects on MPs (lines in Fig. 4.2) to infer MP T_2. The resultant T_2 of

107 µs for WM and 135 µs for GM fall out of the range of the reported T_2 values, from

10 to 60 µs (35,59,60,63,75,96,113). Overall the fittings of T_2 for all ROI's are not robust,

as can be seen from their adjusted R^2 values, shown in Table 4.2. Besides the error

caused by the wrong assumption on $FS_{MP}(0)$, the discrepancy may partially be attributed

to the intrinsic insufficiency to use Bloch equations, which assume a Lorentzian

lineshape (134), to simulate the effects of RF pulses on MPs, which exhibits a super-

Lorentzian lineshape (26,134).

Chapter 5: Determination of the resonance frequency and T_2 for macromolecular protons in a fixed marmoset brain

Previous work has reported an asymmetry of MT around WP resonance frequency, resulting from a mismatch between the resonance frequencies of WPs and MPs (66). Studying of asymmetry in MT is essential for precise estimation of related parameters for MT and CEST experiments. In this chapter, we measure the resonance frequency of MPs relative to that of WPs, by applying off-resonance RF pulses to measure offset frequency dependent saturation effects on WPs and MPs respectively. Similar to Chapter 4, MP T_2 was also studied by applying RF pulses with different B_1 (amplitude of the applied RF pulses) and then simulating the B_1 dependence of saturation effects on MPs, based on Bloch equations simulation. The experiments were performed on fixed marmoset brain samples, which allowed for much higher B_1 than *in vivo* studies, due to the restriction on specific absorption rate (SAR) for *in vivo* studies. The large B_1 for RF pulses used in this work (B_1 ranged from 250 up to 5000 Hz) allowed us to achieve maximal saturation effect on MPs (see Fig. 5.2), such that $FS_{MP}(0)$ could be taken as 1.0, which simplified the two pool model fitting, as discussed in Section 1.2. This work is adapted from our conference abstract (4).

5 .1 *Importance of studying MP resonance frequency and MT asymmetry*

Magnetization Transfer (MT) contrast has been used to study brain myelination and for characterization of myelin disorders (63,135,136). Most MT studies ignore potential chemical shifts between macromolecular protons (MPs) and water protons (WPs) (26,63,135,136), despite the evidence to the contrary (66,67). Ignoring chemical shift

results in errors in estimation of MT parameters, especially at high field. Experiments with steady state off-resonance RF irradiation have been performed to characterize MP chemical shift and its effect on MT; however, these generally suffer from confounds related to direct WP saturation and CEST effects. Here, we propose a novel approach to studying the MP chemical shift based on a delay-dependent pulsed MT experiment.

MP T_2 was also studied, following methods similar to those described in Chapter 4, by measuring the B_1 (amplitude of the applied RF pulse) dependence of saturation effects on MPs and comparing it with simulated saturation effects as a function of T_2 and B_1 (Fig 5.4), based on the Bloch equations.

5 .2 *Two-pool exchange model and MRI measurements*

One *ex vivo* scan of a fixed marmoset brain (*Callithrix jacchus*) was performed on a Bruker 4.7 T scanner. In order to study MT without CEST and direct WP saturation effects, we followed a recent approach based on monitoring the saturation of WP signal following a brief, 4 ms MP saturation pulse (1,2). MP T_2 was studied by applying RF pulses with different B_1 to saturate MPs to different extent and measuring the B_1 dependence of saturation effects on MPs. This was further compared with the simulated saturation effects as a function of B_1 and T_2, based on Bloch equations, to infer MP T_2. Further, the effect of an off-resonance frequency-specific saturation recovery (SR) pulse (45,50,133) on both MP and WP magnetizations was also studied as a function of post-saturation delay t measured from the center of the pulse) using a multi-gradient echo sequence. Then the amplitude of the saturation effects and its dependence on the off-resonance frequency of the frequency-specific SR pulse were calculated and modeled using a super-Lorentzian (SL) lineshape for MPs and a Lorentzian lineshape for WPs to

determine their off-resonance frequencies respectively. First, experiments were performed to determine parameters describing MT kinetics and MP T_2, assuming a two-pool model of exchange between MPs and WPs (defined as *Experiment I*), and subsequently, both MP and WP resonance frequencies were investigated by fitting SL and Lorentzian lineshapes to the magnitude of the saturation effects as a function of off-resonance frequency of the frequency specific SR pulse respectively (defined as *Experiment II*).

Two-pool exchange model

Following an initial RF pulse that differentially saturates the WP and MP pools, we assume that the fractional saturations of the two pools, FS_{WP} and FS_{MP}, experience bi-exponential evolutions as described in Eqs. 1.12-1.13 in Chapter 1 (1,2,76).

Experiment I: Determination of MT parameters and MP T_2

To measure the parameters related to the two-pool exchange model and MP T_2, two types of preparation pulses, namely a WP IR pulse and six composite broadband MP SR pulse with varying B_1 amplitude were used to saturate the two pools to different extents. After variable delay t, MGRE image acquisition was performed to sample $FS_{WP}(t)$. The inversion pulse had a constant B_1 of 2000 Hz (1 Hz equals 0.0235 µT) and a pulse duration of 0.5 ms. The six SR pulses had a common duration of 4 ms, each consisting of a train of variable number of hard pulses with angles 90°, -180°, 180°, -180°, …., -180°, 90°. The six different combinations of number of pulses and B_1 amplitude for the SR pulses, included 3 & 250 Hz, 5 & 500 Hz, 9 & 1000 Hz, 17 & 2000 Hz, 33 & 4000 Hz and 33 & 5000 Hz. The use of multiple different preparation pulses facilitated fitting λ_1 and λ_2, and furthermore allowed extraction of k_{MW}, k_{WM}, f, and $R_{1,WP}$, and $R_{1,MP}$. The use

of multiple B_1's for the SR pulses allowed us to measure the B_1 dependence of saturation effects on MPs to infer MP T_2, based on Bloch equations simulation (Fig. 5.4), similar to the study in Chapter 4. By using the large range of B_1 (from 250 up to 5000 Hz), we also found that the saturation effect on MPs, $FS_{MP}(0)$, maximized for B_1 of 2000Hz and above, such that $FS_{MP}(0)$ for the pulses with B_1 of 2000-5000 Hz was taken as 1.0, to simplify the two-pool exchange model fitting, as discussed in Section 1.2.

Experiment II: Determination of resonance frequency for MPs and WPs

To determine MP and WP resonance frequencies, the broadband SR pulses were replaced by a frequency-specific SR pulse and applied at 23 different frequency offsets (F), ranging from -30 kHz to 30 kHz (-30, -15, -8, -5, -2, -1, -0.7, -0.4, -0.2, -0.1, 0, 0.1, 0.2, 0.4, 0.7, 1, 2, 5, 8, 15, 30 kHz). The pulse had a duration of 12 ms, a B_1 amplitude of 500 Hz, and a hyperbolic secant envelope for its amplitude, with a β of 600 s^{-1} (104). The full width at half maximum (FWHM) of its power spectral density is 119 Hz.

Image acquisition

For all IR and SR experiments, image data were acquired using multiple gradient echo (MGRE), sampling only one slice after the preparation pulses. The delay times in *Experiment I* were 3.8, 8, 28, 58, 98, 198, 398, 798 and 1598 ms (defined as the time from the center of the inversion pulse to the center of the MGRE excitation pulse). The delay times for the frequency-specific SR experiments in *Experiment II* were: 7.8, 57.8, 107.8, 207.8 and 407.8 ms. The IR and SR delay times were chosen to sample the signal recovery dynamics. The isotropic image resolution was 0.25 mm. The echo time (TE) was 3 ms, and TRs were 3 s for all IR and SR experiments. For all IR and SR experiments, only one measurement were performed, and one reference signal was

acquired by omitting the preparation pulse to provide to estimate $M_{WP}(\infty)$ in Eq. 1.12, and allow conversion of the measured signals to $FS_{WP}(t)$.

Pre-processing

Pre-processing included signal polarity correction, and calculation of $FS_{WP}(t)$. Polarity correction was needed only for IR (magnitude) data, because of signal rectification during the complex-to-magnitude conversion, during image reconstruction. It was performed based on the phase difference between the IR images with the (un-inverted) reference image. The $FS_{WP}(t)$ level expressed in Eq. 1.12 was determined by dividing each IR image by the corresponding reference image (i.e. data acquired without inversion pulse). Analogous analysis was performed for the SR data, however without performing the signal polarity adjustment. All processing was done in IDL (Exelsis Visual Information Solutions, Boulder, CO, USA).

ROI selection

Regions of interest were selected in white matter and grey matter, as illustrated in Fig. 5.1. All data are averaged within the WM and GM ROI's respectively for further analysis.
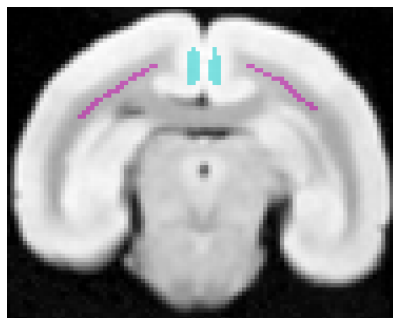
Figure 5.1 ROI's in WM (purple) and GM (cyan).

Dependence of MP and WP saturations on frequency offsets of SR pulses

To determine λ_1, λ_2, k_{WM}, k_{MW}, $R_{1,MP}$ and $R_{1,WP}$, both the IR and the broadband SR data from *Experiment I* were analyzed. Defining $FS_{MP}(0, B_1)$ as the $FS_{MP}(0)$ created by a broadband SR pulse with amplitude of B_1 in *Experiment I, and defining $FS_{MP}(0, F)$* as the $FS_{MP}(0)$ and $FS_{WP}(0, F)$ as the $FS_{WP}(0)$ created by a frequency-specific SR pulse at frequency offset F in *Experiment II*, $FS_{MP}(0, B_1)$, $FS_{MP}(0,F)$ and $FS_{WP}(0, F)$ can be then calculated based on analysis of all the data in *Experiment I & II*. The following steps were involved:

[1] Fit Eq. 1.12 to the IR and broadband SR data in *Experiment I* jointly, yielding one pair of decay rates (λ_1, λ_2) and seven pairs of amplitudes (a_1, a_2) for GM and WM ROI's respectively.

[2] $R_{1,MP}$ and $R_{1,WP}$ were assumed to be the same for WM and GM, as suggested by previous report that the contrast between WM and GM primarily originates from their difference in MP fraction (2,12,13). $FS_{MP}(0)$ was taken as 1.0 for the SR experiment with B_1 of 2000 Hz in *Experiment I*, based on the observation from Fig. 5.4 that $FS_{MP}(0)$ maximized for B_1 of 2000-5000 Hz. Then calculate k_{WM}, k_{MW}, $R_{1,WP}$, $R_{1,MP}$ using Eqs. 1.10 & 1.14, based on the decay rates and amplitudes found under Step [1].

[3] Fit Eq. 1.12 to the frequency-specific SR data from *Experiment II*, to find a pair of amplitudes ($a_1(F)$, $a_2(F)$) at each F, using decay rates (λ_1, λ_2) found under Step [1]. Then calculate $FS_{MP}(0,F)$ and $FS_{WP}(0,F)$ using these ($a_1(F)$, $a_2(F)$) pairs, according to Eqs. 1.12-1.13 by setting $t=0$ s, with all other parameters known from Steps [1] and [2], as shown in Eqs. 5.1-5.2.

$$FS_{MP}(0, F) = \frac{a_1(F)(-\lambda_1 + k_{WM} + R_{1,WP})}{k_{WM}} + \frac{a_2(F)(-\lambda_2 + k_{WM} + R_{1,WP})}{k_{WM}} \quad (5.1)$$

$$FS_{WP}(0, F) = a_1(F) + a_2(F) \qquad (5.2)$$

[4] Using the amplitude pairs $(a_1(B_1), a_2(B_1))$ $((a_1, a_2)$ pair for broadband SR experiments with amplitude of B_1 in Experiment I) and decay rates (λ_1, λ_2) found in Step [1], calculate $FS_{MP}(0,B_1)$ using these $(a_1(B_1), a_2(B_1))$ pairs, according to Eq. 1.13 by setting $t=0$ s, with all other parameters known from Steps [1] and [2], as shown in Eq. 5.3.

$$FS_{MP}(0, B_1) = \frac{a_1(B_1)(-\lambda_1 + k_{WM} + R_{1,WP})}{k_{WM}} + \frac{a_2(B_1)(-\lambda_2 + k_{WM} + R_{1,WP})}{k_{WM}} \qquad (5.3)$$

Determination of resonance frequencies for MPs and WPs in WM and GM ROI's

A SL lineshape (Eq. 5.4) was fit to the WM and GM ROI averaged $FS_{MP}(0,F)$ respectively, following previous work (26,65). A Lorentzian lineshape (Eq. 5.5) was fit to the WM and GM ROI averaged $FS_{WP}(0,F)$ respectively.

$$g_{SL}\left((F - \Delta F_{SL}), T_{2,SL}, A_{SL}\right) =$$

$$A_{SL}\sqrt{\frac{2}{\pi}} \int_0^{\frac{\pi}{2}} \frac{T_{2,SL}}{|3\cos^2\theta - 1|} exp\left(-2\left(\frac{2\pi(F - \Delta F_{SL})T_{2,SL}}{3\cos^2\theta - 1}\right)^2\right) \sin\theta d\theta \qquad (5.4)$$

$$g_L((F - \Delta f_0(F) - \Delta F_L), T_{2,L}, A_L) = A_L \frac{T_{2,L}}{\pi\left(1 + \left(2\pi(F - \Delta f_0(F) - \Delta F_L)T_{2,L}\right)^2\right)} \qquad (5.5)$$

In Eqs. 5.3-5.4, A is a scaling factor, F is the frequency of the applied frequency-specific SR pulse as mentioned above, and ΔF is the resonance frequency.

Determination of MP T_2 for WM and GM ROI's

Similar to the study in Chapter 4, $FS_{MP}(0,B_1)$ was compared with the simulated dependence of longitudinal magnetization following a broadband SR pulse on T_2 and B_1 (Fig. 5.4), obtained from simulations of the Bloch equations, to find T_2 for MPs in WM and GM respectively.

Table 5.1 Fitting results of the two-pool exchange model parameters for WM and GM ROI's; R^2 is adjusted for degree of freedoms.

	λ_1	λ_2	$R_{1,WP}$	$R_{1,MP}$	f	k_{WM}	k_{MW}	R^2
WM	28.04	2.11	1.44	3.97	0.29	7.11	17.64	0.999
GM	21.04	1.75	1.44	3.97	0.14	2.44	14.95	0.999
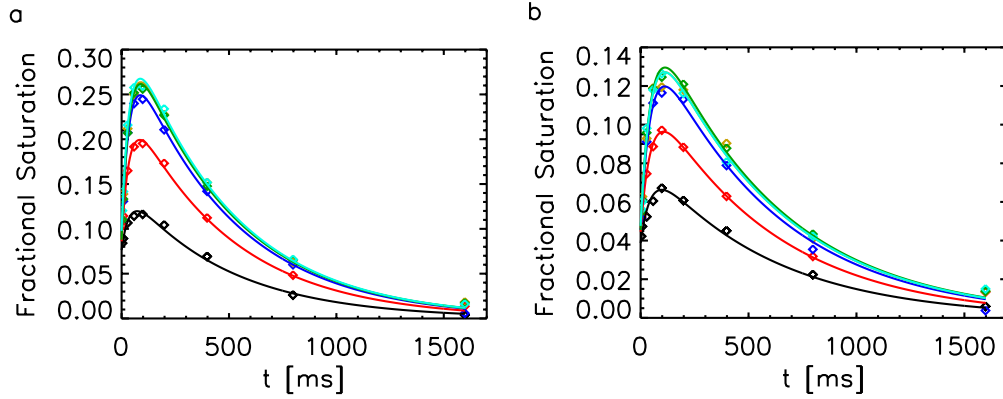
Figure 5.2 Fractional saturation of WPs in WM (a) and GM (b) ROI's as a function of delay time *t* for broadband SR pulses in *Experiment I* with different parameters: 250 Hz with 3 flips (black), 500 Hz with 5 flips (red), 1000 Hz with 9 flips (blue), 2000 Hz with 17 flips (cyan), 4000 Hz with 33 flips (green), 5000 Hz with 33 flips (yellow). Solid lines are two pool model fits to measurement data (symbols).
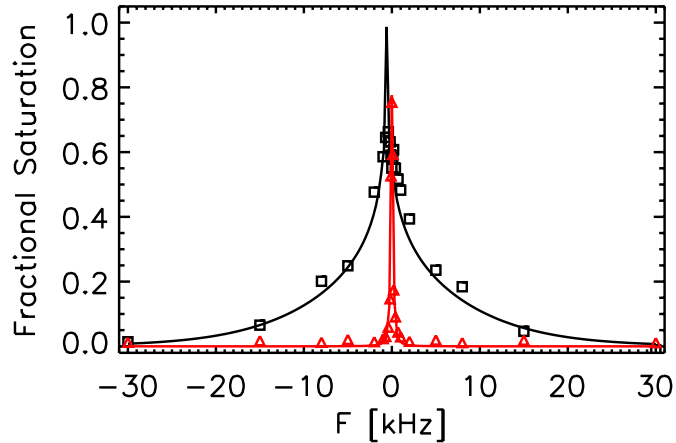
Figure 5.3 MP (black) and WP (red) fractional saturation in WM as a function of frequency offset. Black line shows SL fit to $FS_{MP}(0,F)$ (black squares) and the red line shows Lorentzian fit to $FS_{WP}(0,F)$ (red triangles).
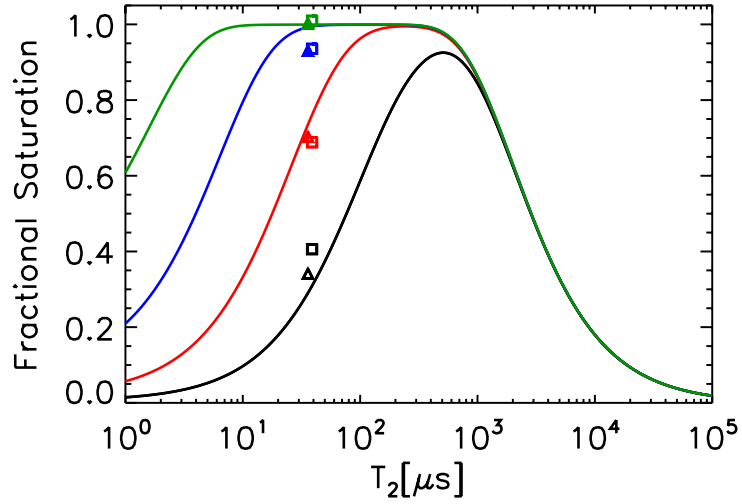
Figure 5.4 Fractional saturation created by a SR pulse as function of T_2 for four different combinations of number of hard pulses and B_1: 3 & 250 Hz (black), 5 & 500 Hz (red), 9 & 1000 Hz (blue), and 17 & 2000 Hz (green) with the same pulse duration of 4 ms, simulated using the Bloch equations. Fitting these simulated fractional saturations to those measured in WM (triangular symbols) and GM (square symbols) ROI's resulted in MP T_2 of 36 μs for WM and 39 μs GM respectively.

Table 5.2 Results for fitting of MP T_2 and R^2 (adjusted for degrees of freedoms), for ROI's in WM and GM.

	WM	GM
T_2 (μs)	36	39
R^2	0.96	0.88

5 .3 Resonance frequencies of MPs and WPs and MP T_2

Fig. 5.2 shows the fitting of $FS_{WP}(t)$ for the SR experiments in *Experiment I* to Eq. 1.12, for both WM and GM ROI's. As can be seen, $FS_{WP}(t)$ maximized at 2000 Hz pulse amplitude, suggesting full (100%) MP saturation. Table 5.1 shows the corresponding two-pool exchange model parameters. The MP fraction and all the exchange rates, including k_{MW}, k_{WM}, and $R_{1,WP}$, and $R_{1,MP}$ in both WM and GM are higher than those

99

measured on marmoset brain *in vivo* reported in Chapter 4 (3), which may be attributed to the dehydration effect induced by fixation.

Dependence of the fractional saturations of MPs and WPs on offset frequency of the off-resonance RF pulse (Fig. 5.3) shows a maximum at -544 Hz (-2.72 ppm) for MPs and 10 Hz (0.05 ppm) for WPs, in both WM and GM ROI's. Overall, the resonance frequency of MPs has a shift of -2.77 ppm relative to that of WPs.

Fitting of $FS_{MP}(0,B_1)$ to the simulated saturation effects on MPs as a function of B_1 and T_2 is shown in Fig. 5.4. The MP T_2 was found to be 36 μs for WM and 39 μs for GM respectively, as summarized in Table 5.2.

5.4 *Comparison and discussion*

The frequency specific SR experiments allowed investigation of MT asymmetries without confounding effects from direct WP saturation and CEST (27). The former was effectively accounted for in the 2-pool exchange model fitting approach, whereas the latter was avoided due to the short duration of the MT pulse. Based on this, the MT effect was found to be symmetric around -2.77 ppm, which is consistent with previous work (66). The resonance frequency of MPs relative to WPs agrees with the range of chemical shift of alkyl protons, which are abundant in membrane lipids and constitute a major fraction of MPs. The observed MP chemical shift should be accounted for in the analysis of MT or CEST experiments, that aim at quantifying parameters such as MP pool fraction (*f*) and MT exchange rates (k_{MW} *and* k_{WM}), or the content and spectral properties of exchangeable protons (27).

Experiments on the fixed marmoset brain allowed us to apply high-power RF pulse (up to B_1=5000 Hz in this study), and further to confirm in experiments, that using the SR

pulse with 17 flips and B_1 of 2000 Hz, the saturation effect on MPs maximized, as can be seen from Fig. 5.4. Therefore, SR pulse with 17 flips and B_1 of 2000 Hz proved to completely saturate the MPs and the corresponding $FS_{MP}(0)$ could be taken as 1.0 to simplify the fitting of two-pool exchange model as discussed in Section 1.2. This determination of $FS_{MP}(0)$ provides improved estimation of two-pool exchange model parameters and MP T_2, compared to the study in Chapter 4, where $FS_{MP}(0)$ was estimated only based on Bloch equations simulation.

$R_{1,MP}$ is found to be much higher than $R_{1,WP}$, confirming our previous *in vivo* study on human brain (2), reported in Chapter 3. However, in most conventional MT studies, $R_{1,MP}$ was either assumed to be 1.0 s^{-1} or to be the same as $R_{1,WP}$, which had been reported to result in error in estimation of MP fraction (11). This may explain the high MP fraction determined using our transient MT method (1,2), compared to the conventional steady state MT approach (63,135).

The T_2's for WM and GM were found to be 36 and 39 μs respectively, consistent with the reported T_2 values, from 10 to 60 μs (35,59,60,63,75,96,113). However, both T_2's are much smaller than 107 μs for WM and 135 μs for GM measured *in vivo* reported in Chapter 4. Besides the difference in physiological conditions, this discrepancy can also be caused by the improved determination of $FS_{MP}(0)$ using experiments with a large range of B_1 for the RF pulses in this study, whereas $FS_{MP}(0)$ was estimated only based on Bloch equations simulation in Chapter 4.

Experimental data from Fig. 5.4 (symbols) shows that, increasing B_1 from 1500 Hz to 2000 Hz resulted in increase of $FS_{MP}(0,B_1)$ from 0.93 to 1.0 for both WM and GM. However, simulation based on Bloch equations shows no difference between saturation

effects for RF pulses with B_1 of 1500 Hz (the blue line in Fig. 5.2) and 2000 Hz (the green line in Fig. 5.2), for T_2 in the range of 30 to 400 µs, as can be seen from Fig. 5.4. This may suggest that a portion of MPs has T_2 values outside the range of 30 to 400 µs. This is in agreement with the previous reported MP spectrum exhibiting a SL lineshape (26,134), which is summation (or integration) of Gaussians with a range of T_2 values (74,102). The situation may be further complicated by the high B_1 used in this study (up to 2000-5000 Hz), which causes the saturation effects to be nonlinear with the power of an RF pulse (the integral of squared B_1 amplitude over the pulse duration) (137,138). Altogether, this suggests that simulation based on Bloch equations, which assume a single Lorentzian line for MPs, is insufficient to interpret the measured B_1 dependence of saturation effects on MPs in this study.

A potential confound is the effect of tissue heating, caused by the RF pulses with high B_1 (up to 5000 Hz) used in this study. Tissue heating may affect nuclear magnetic resonance (NMR) properties, including T_2 (139). To estimate the specific absorption rate (SAR) and temperature change in the brain sample, we assume the RF pulse amplitude B_1=5000 Hz (117.4 µT) is uniform across the sample. Then the amplitude of the electric field E and SAR can be calculated as:

$$E = B_1/\sqrt{\varepsilon_r \varepsilon_0 \mu_0} \qquad (5.6)$$

$$SAR = \sigma E^2/\rho \qquad (5.7)$$

Here σ= 0.67 S/m (140) is the conductivity and ρ=1000 kg/m^3 is the density, ε_r=51 is the relative permittivity (140), of the brain sample, ε_0 and μ_0 are the permittivity and permeability of vacuum. Then the temperature increase ΔT created by each pulse can be calculated as:

$$\Delta T = \frac{SAR * T_d}{C} \tag{5.8}$$

where T_d=4 ms is the pulse duration, and C=3600 J/kg/K (141) is the specific heat of brain tissue. And ΔT is found to be 0.018 K, induced by the pulse with the highest B_1 of 5000 Hz, for each cycle with TR of 3 s. Assuming the weight of the brain sample as 0.01 kg, then the power deposition rate can be written as:

$$P = \frac{SAR * 0.01 \, kg * 4ms}{3 \, s} \tag{5.9}$$

Assume the temperature of the brain sample and air are in equilibrium, according to Fourier's law, the temperature difference between the brain sample and air can be calculated as:

$$\Delta T = \frac{P * b}{k * a} \tag{5.10}$$

where a=0.001 m^3 is the estimated surface area of the tube hosting the brain sample, k=0.3 W·m^{-1}·K^{-1} is the thermal conductivity of Fomblin filling in the tube, and b=0.003 m is the estimated distance from the brain sample to the interface of the tube and air. With these assumptions, we found ΔT=1.3 K. Therefore, the temperature change and the thus induced change of tissue properties, caused by the high B_1 RF pulses, are small and unlikely to affect MP T_2 values.

Chapter 6: Spectral characteristics of semi-solid protons in human brain white matter at 7 T

Due to the difficulty in the detection of MPs in MRI because of their short T_2, interpretation of MT contrast has generally relied on various assumptions about the spectral properties of MPs and the effect RF pulses on their magnetization. For example, in steady state MT, a super-Lorentzian lineshape centering at resonance frequency of WPs is often assumed for MP spectrum (26,63); in previous transient MT experiments, MPs were often assumed unaffected by the RF pulses (45,50). To better understand the roles and behaviors of MPs in human brain MRI and further improve MT related MRI techniques, the spectral properties of MPs, which define the response of MPs to a certain RF pulse, have to be determined *in vivo*, and this is the goal of the work described in this chapter. Low-amplitude (B_1=200 Hz) RF pulses are used to measure the dependence of the saturation effects of MPs on RF pulses applied at different frequency offsets and to further determine the spectral properties for MPs, including their lineshape, T_2, and resonance frequency. Direct saturation on WPs is accounted for by the two-pool exchange model described in Section 1.2. Confounds from CEST effects is minimized by using RF pulses with short pulse durations of 6-12 ms. This work is adapted from our manuscript accepted for publication in Magnetic Resonance in Medicine.

6.1 *Significance and previous attempts to quantify spectral properties of MP*

In MRI of human brain, Magnetization Transfer (MT) contrast (142) has been used extensively to study tissue composition, specifically the fraction of hydrogen (^{1}H) protons with restricted mobility, often referred to as semi-solid protons or macromolecular

protons (MPs) (2,54,63,135,136). These protons, having a short T_2, are generally not directly detectable by MRI but, through MT, exert an influence on ^{1}H protons in water (WPs), the primary contributors to the MRI signal. Measures of the magnitude of this MT effect have been used to study MP content in brain tissue (63,135,136) and characterize alterations in brain myelin content in multiple sclerosis (94,143) and other pathology (144–146).

The mechanisms underlying MT contrast are complex (147,148), often rendering interpretation and quantification difficult. Generally, the strongest contributions to MT come from MPs such as proteins and lipids, whose protons can affect WP magnetization through dipolar coupling and chemical exchange (26,54,147,149). However, chemical exchange effects of smaller molecules may contribute as well (42,150). And chemical exchange effects can be enhanced by using long RF irradiation as is done in so called chemical exchange saturation transfer (CEST) techniques (27). While MT generally contributes to MRI contrast to some extent, this contribution is amplified by differentially perturbing WP and MP magnetization levels from their thermal equilibrium values (54). Because of this, MT contrast is not only dependent on dipolar coupling strength and exchange rate between WP and MP, but also on specifics of the MRI pulse sequence (54). It is the latter principle that has been exploited to highlight certain contributions to MT, rendering a contrast that emphasizes either MPs (59,63,70,135,136) or exchangeable protons (27,150) with some chemical specificity (27). On the other hand, MP magnetization levels are often not well known and difficult to control, due to the short transverse relaxation time (T_2) of MPs. Therefore, for proper quantification of MT, and

avoid unintended contribution of MT in general (non-MT) MRI applications, MP magnetization levels need to be estimated.

Apart from the exchange rate between MPs and WPs, MT contrast is dependent on the characteristics of the radiofrequency (RF) irradiation, the spectral characteristics of MPs and WPs, and T_1 relaxation. Of these factors, the MP spectrum may be the most critical and most difficult to measure, because of MPs extremely short transverse relaxation time constant (T_2). Direct measurements with NMR spectrometers on *ex-vivo* brain tissue samples and various membrane model systems, including myelin extracts and lecithin, have shown that MPs have complex lineshapes with varying width and off-resonance frequency, dependent on the host molecules and strength of dipolar coupling with neighboring MPs (35,56–60). Typically, at field strengths up to 9.4 T, super-Lorentzian (SL) and Lorentzian lineshapes have been reported over a spectral range of about 6 ppm and T_2 values of 20-100 μs (35,56–60,111). The general understanding is that in membrane-rich white matter, lipid methylene and methyl groups are the major contributors to these spectra (13,35,59,111).

Because MP spectral characteristics may be quite different in-vivo, and at higher field strengths, various attempts have been made to infer the MP spectrum from their effect on the easier detectable WP signal using steady state MT experiments. Studies at clinical field strengths up to 3 T have reported a SL lineshape with a T_2 of in the range of 9-15 μs for white matter (WM) in-vivo (63,66,102), similar to the range of 9-13 μs found for tissue samples using this approach (26,65,75,135), but below the 20-100 μs range directly measured by NMR spectroscopy. In addition, several studies have found the MP spectrum to be shifted by about -3 ppm relative to the WP resonance (66–69), consistent

with the chemical shift of lipid methylene protons. However this has proven difficult to reproduce, in particular at high field, due to confounding CEST effects (55), and increased tissue heating associated with RF irradiation. Currently, most quantitative MT methods assume the MP spectrum to be centered on the water resonance.

To further investigate MP spectral characteristics, with the ultimate purpose of better quantifying MT contrast in MRI of brain tissue, we applied an indirect measurement approach based on transient MT effects after MP saturation with a brief, RF pulse (98). Using a range of specific RF frequencies allowed us to characterize MP spectral characteristics in human brain at 7 T in an efficient manner, while minimizing effects of CEST, tissue heating, and direct WP saturation.

6.2 *Two-pool exchange model and MRI measurements*

MRI experiments were performed on eight human subjects (ages 20-49, average 30.6, 4 female), scanned under an IRB approval on a 7 T Siemens scanner using a 32-channel receive array. In order to study MT without CEST and direct MP saturation effects, we followed a recent approach based on monitoring the saturation of WP signal following a brief, 6-12 ms MP saturation pulse (1,2). This saturation recovery (SR) approach resembles the selective inversion recovery (IR) approach (45,50), but sacrifices some sensitivity to obtain an improved estimate of initial MP magnetization level, and render this level insensitive to B_1 variation (1,2). Like the IR approach, it allows sensitive determination of the parameters describing the MT process, by accounting for the direct water saturation effects (1,2,45,50), and minimization of CEST effects and tissue heating. First, experiments were performed to determine parameters describing MT kinetics, assuming a two-pool model of exchange between MP and WP (defined as Experiment I),

and subsequently, MP spectral characteristics were investigated by studying the magnitude of the MT effects as a function of the frequency of narrowband MP saturation pulse (defined as Experiment II).

Two-pool exchange model

Following an initial RF pulse that differentially saturates the WP and MP pools, the fractional saturations of the two pools, FS_{WP} and FS_{MP}, experience bi-exponential evolutions as follows (1,2,76):

$$FS_{WP}(t) = 1 - \frac{M_{WP}(t)}{M_{WP}(\infty)} = a_1 e^{-\lambda_1 t} + a_2 e^{-\lambda_2 t} \qquad (6.1)$$

$$FS_{MP}(t) = 1 - \frac{M_{MP}(t)}{M_{MP}(\infty)} = \frac{a_1(-\lambda_1 + k_{WM} + R_{1,WP})}{k_{WM}} e^{-\lambda_1 t} + \frac{a_2(-\lambda_2 + k_{WM} + R_{1,WP})}{k_{WM}} e^{-\lambda_2 t}$$

$$(6.2)$$

$$2\lambda_{1,2} = R_{1,WP} + R_{1,MP} + k_{MW} + k_{WM} \pm \sqrt{(R_{1,MP} - R_{1,WP} + k_{MW} - k_{WM})^2 + 4k_{MW}k_{WM}}$$

$$(6.3)$$

$$a_{1,2} = \pm \frac{FS_{WP}(0)(R_{1,WP} + k_{WM} - \lambda_{2,1}) - FS_{MP}(0)k_{WM}}{\lambda_1 - \lambda_2} \qquad (6.4)$$

$$(1-f)k_{WM} = fk_{MW} \qquad (6.5)$$

In these equations, M_{WP} and M_{MP} are the longitudinal magnetizations of the two pools, $R_{1,WP}$ and $R_{1,MP}$ are their relaxation rates, λ_1 and λ_2 are fast and slow rate constants of the saturation recovery, and a_1 and a_2 are the corresponding amplitudes. Parameters k_{WM} and k_{MW} represent the MT exchange rate constants relative to WP and MP pool sizes respectively.

Experiment I: Determination of MT parameters

To measure the parameters related to the two-pool exchange model, two types of preparation pulses, namely a WP inversion recovery (IR) pulse and a composite broadband MP saturation recovery (SR) pulse, were used to saturate the two pools to

different extents. After variable delay t, EPI image acquisition was performed to sample $FS_{WP}(t)$. The use of two different preparation pulses facilitated fitting λ_1 and λ_2, and furthermore allowed extraction of k_{MW}, k_{WM}, f, and $R_{1,WP}$ by assuming $R_{1,MP} = 2$ s^{-1} and $FS_{MP}(0) = 0.93$ for the broadband SR experiment as determined previously (2). The inversion pulse was adiabatic, with a hyperbolic secant envelope, duration of 5.12 ms, energy of 0.51 $(\mu T)^2$s, B$_1$ (amplitude of the RF field) modulation frequency of 833 Hz and β of 1400 s^{-1} (104). The broadband SR pulse had a duration of 6 ms and consisted of a train of 17 hard pulses with angles 60°, -120°, 120°, -120°, …., -120°, 60°, with a B$_1$ amplitude of 833 Hz (2).

Experiment II: Determination of MP spectral characteristics

To determine MP spectral characteristics, the broadband SR pulse was replaced by a frequency-specific SR pulse and applied at 12 different frequency offsets (F) with respect to the water resonance frequency, ranging from -16 kHz to 16 kHz (-16, -8, -4, -2, -1, -0.5, 0.5, 1, 2, 4, 8, 16 kHz). The order of scans for different values of F was randomized for each subject. The pulse had a duration of 12 ms, and a hyperbolic secant envelope for its amplitude, identical to that used for the inversion pulse described above, with a β of 600 s^{-1} (104). The full width at half maximum (FWHM) of its power spectral density is 119 Hz. A relatively low B$_1$ amplitude of 200 Hz was used in order to avoid saturation and the non-linear relationship between $FS_{MP}(0)$ and the integral of squared B$_1$ amplitude over the pulse duration for all values of F (137,138). This simplified the derivation of the MP spectrum from the experimental data.

Image acquisition

For both IR and SR experiments, image data were acquired using single-shot EPI, sampling 5 slices consecutively after the preparation pulse; cycling the slice order over 5 repetitions thus resulted in acquisition of 5 delay times for each slice (125). Axial-oblique slices of 2 mm thickness were placed, with 3.4 mm inter-slice gap, parallel to AC-PC line and encompassed the central part of the corpus callosum. The delay times for the IR experiment were 6, 63, 144, 282 and 1200 ms (defined as the time from the center of the inversion pulse to the center of the EPI excitation pulse). The delay times for the broadband SR experiments were: 7, 127, 258, 401 and 559 ms and for the frequency-specific SR experiments were: 10, 130, 260, 402 and 559 ms. The IR and SR delay times were chosen to sample the signal recovery dynamics, within the constraint of the minimal slice repetition time (TR) set by the duration of the EPI readout. The image resolution was 144x108 with SENSE rate-2 acceleration, the field-of-view was 240x180 mm. The echo time (TE) was 24 ms, TRs were 6 and 3 s for IR and SR experiments respectively. In order to suppress signals from scalp lipids, the TE was increased by 0.49 ms on even numbered repetitions (2). A multi gradient echo (MGRE) sequence with TR of 0.2 s, TE of 2.5 ms, 7 echoes with echo spacing of 0.74 ms, the same resolution and field-of-view as the EPI scans and total scan time of 21.6 s, was scanned before all IR and SR experiments. This MGRE sequence served as reference to reconstruct the accelerated EPI scans and was also used to estimate the B_0 (amplitude of the static field) inhomogeneity. For IR experiments, six repeat measurements were performed, the first two of which omitted the inversion pulse and were used to provide a reference signal to estimate $M_{WP}(\infty)$ in Eq. 6.1, and allow conversion of the measured signals to $FS_{WP}(t)$. Similarly, ten repetitions (including two serving as reference) and six repetitions (including one

reference) were acquired for the broadband and frequency-specific SR experiments respectively.

Pre-processing

Pre-processing included motion correction, signal polarity correction, averaging, and calculation of FS_{WP}(t). Prior to averaging repetitions, complex images were spatially registered to correct for motion. Only in-plane registration was performed, as the small number of slices did not support through-plane motion correction. Polarity correction was needed only for IR (magnitude) data, because of signal rectification during the complex-to-magnitude conversion. It was performed based on the phase difference between the IR images with the (un-inverted) reference image. The FS_{WP}(t) level expressed in Eq. 6.1 was determined by dividing each IR image by the corresponding reference image (i.e. data acquired without inversion pulse). Analogous analysis was performed for the SR data, however without performing the signal polarity adjustment. All processing was done in IDL (Exelsis Visual Information Solutions, Boulder, CO, USA).

Voxel-wise determination of MP saturation

To determine λ_1, λ_2, k_{WM}, k_{MW}, and $R_{1,WP}$, both the IR and the broadband SR data from Experiment I were analyzed on a voxel-wise basis. Defining FS_{MP}(0, F) as the FS_{MP}(0) created by a frequency-specific SR pulse applied at frequency F, FS_{MP}(0,F) can be then calculated based on analysis of the frequency-specific SR data in Experiment II. The following steps were involved:

1. Fit Eq. 6.1 to the IR and broadband SR data jointly, yielding one pair of decay rates (λ_1, λ_2) and two pairs of amplitudes (a_1, a_2) for each voxel.

2.   Assuming $R_{1,MP}=2$ s^{-1} and $FS_{MP}(0)$ for the broadband SR experiment to be 0.93 as determined previously (2), calculate k_{WM}, k_{MW}, $R_{1,WP}$, using Eqs. 6.3-6.4, based on the decay rates and amplitudes found under Step (a).

3.   Fit Eq. 6.1 to the frequency-specific SR data, to find a pair of amplitudes (a_1(F), a_2(F)) for every voxel at each F, using decay rates (λ_1, λ_2) found under Step (a). Then calculate $FS_{MP}(0,F)$ using these (a_1(F), a_2(F)) pairs, according to Eq. 6.2 by setting $t=0$ s, with all other parameters known from Steps (a) and (b), as shown in Eq. 6.6.

$$FS_{MP}(0,F) = \frac{a_1(F)(-\lambda_1+k_{WM}+R_{1,WP})}{k_{WM}} + \frac{a_2(F)(-\lambda_2+k_{WM}+R_{1,WP})}{k_{WM}} \quad (\,6.6\,)$$

Calculation of B_0 shift for frequency-specific SR scans

B_0 inhomogeneity and its drift over the course of the experiments can potentially change the effective F for each of the frequency-specific SR pulses. B_0 measurement with methods like WASSR (151) can be used to correct for these effects. Here, B_0 inhomogeneity for each scan was calculated voxel-wise as follows:

(a) The phase of even echoes of the MGRE scan was fitted to a linear model to estimate spatial variations (inhomogeneity) in B_0.

(b) The EPI (either IR or SR) scan following the MGRE was assumed to suffer from the same B_0 inhomogeneity as the MGRE scan.

(c) The relative B_0 shift between successive EPI scans (temporal drift) was determined from their relative phase.

(d) The absolute B_0 shift, ΔB_0, for a specific EPI scan was calculated by summing over all its previous relative B_0 shifts and the B_0 inhomogeneity of the first EPI scan, as determined in Step (c) and Step (b) respectively.

MP spectral characteristics in a WM region of interest

To infer MP spectral characteristics in WM in human brain, we performed region of interest (ROI) analysis. Since the total scan time for each subject took up to ~1.35 hours and only motion within the axial plane was corrected for by in-plane registration, care was taken to select the ROI well within WM. This was done from images of the MP fraction *f* thresholded at 0.2, and Gaussian smoothed over a kernel of 7 voxels. Fig. 6.1 shows an example of WM ROI's on five slices for one of the 7 subjects studied.
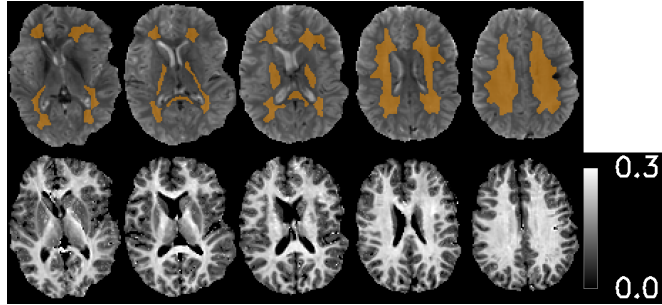
Figure 6.1 Example of WM ROI selection. ROI location is shown superimposed on EPI scan (top row), together with corresponding *f* maps. Selection was based on thresholding *f* at 0.2, followed by Gaussian smoothing with a 7 voxel kernel.

The ROI averaged $FS_{MP}(0,F)$ was calculated for each subject. Following previous work (26,65), a SL lineshape (Eq. 6.7) and Lorentzian (L) lineshape (Eq. 6.8) were fit to this data.

$$g_{SL}\left((F - \Delta f_0(F) - \Delta F_{SL}), T_{2,SL}, A_{SL}\right) =$$

$$A_{SL}\sqrt{\frac{2}{\pi}} \int_0^{\frac{\pi}{2}} \frac{T_{2,SL}}{|3\cos^2\theta - 1|} exp\left(-2\left(\frac{2\pi(F - \Delta f_0(F) - \Delta F_{SL})T_{2,SL}}{3\cos^2\theta - 1}\right)^2\right) sin\theta d\theta \qquad (6.7)$$

$$g_L((F - \Delta f_0(F) - \Delta F_L), T_{2,L}, A_L) = A_L \frac{T_{2,L}}{\pi\left(1 + \left(2\pi(F - \Delta f_0(F) - \Delta F_L)T_{2,L}\right)^2\right)} \qquad (6.8)$$

In Eqs. 6.7 and 6.8, A is a scaling factor, F is the frequency of the applied frequency-specific SR pulse as mentioned above, and ΔF is the resonance frequency of MPs. $\Delta f_0(F)$ is the WM ROI averaged frequency offset caused by the B_0 shift for a frequency-specific SR scan applied at frequency F, and is equal to $\gamma \Delta B_0 / 2\pi$, with ΔB_0 determined above and γ being the gyromagnetic ratio. The averages and standard deviations were calculated for T_2 and ΔF over subjects for both lineshapes. Fitting using the sum of two Lorentzians to individual subject $FS_{MP}(0,F)$ was also performed, using a common ΔF_L determined from the single Lorentzian fit for both Lorentzians, to account for the potential contribution of two MP pools with distinct spectral characteristics (73–75,152). Finally, fitting SL, Lorentzian and sum of two Lorentzians to $FS_{MP}(0,F)$ data combined from all subjects was also performed.

Effects of number of voxels selected in ROI on T_2 and ΔF fitting

The number of voxels in the above-mentioned WM ROI for each subject ranged from 2648 to 5580. To investigate the effects of number of voxels in ROI on fitting of T_2 and ΔF, we reduced the number of voxels for each subject to 1024, 512, 256, 128, 64, 32, 16, 8, 4, 2, 1. These new voxels were randomly selected from the original WM ROI and this process was repeated 50 times. Following each selection of variable number of voxels, we repeated the processes of fitting to SL and Lorentzian as described above, to find T_2 and ΔF. The standard deviations for both T_2 and ΔF were calculated over the 50 selections and 7 subjects (50*7=350 samples for T_2 and ΔF, respectively), and were then plotted as a function of the number of voxels in the ROI's.

Potential effects of B_1 amplitude on the MP spectrum

The validity of our approach to infer the MP spectrum implicitly assumes a linear relationship between $FS_{MP}(0,F)$ and the power of off-resonance MT pulses, which holds true only when the B_1 amplitude is low enough to avoid substantial saturation (137,138). To study the effect of B_1 amplitude of the frequency-specific SR pulse on the inferred MP spectrum, we fitted a Lorentzian lineshape to simulated $FS_{MP}(0,F)$'s using Bloch equation. First, $FS_{MP}(0,F)$ for the MPs with a $T_{2,input}$ of 65 μs is simulated, under the influence of frequency-specific hyperbolic secant SR pulse with a duration of 12 ms and a B_1 of 200 Hz (matching the preparation pulses used in the frequency-specific SR experiments), applied at several different frequency offsets, ranging from -16 kHz to 16 kHz. A Lorentzian fit yielded a $T_{2,output}$. Then, dependence of $T_{2,output}$ on $T_{2,input}$ and B_1 were studied by varying $T_{2,input}$ while keeping B_1 fixed as 200 Hz, and varying B_1 while keeping $T_{2,input}$ fixed as 65 μs, respectively. A Lorentzian rather than a SL lineshape was used in all these simulations, due to the lack of a rigorous way to simulate Bloch equations incorporating a SL lineshape, under influence of a shaped MT pulse (134).

Quantification of the symmetry of the MP spectrum

The effect of CEST on our spectrum measurements is expected to be small because of the short, 12 ms duration of the RF pulses used for the SR experiment. To investigate the presence of any remaining CEST effect, we analyzed spectral symmetry with the notion that any asymmetries would point to a potential CEST contribution (66,68,137,138). Symmetry was shown by inspecting the residuals after subtracting the fits from ROI averaged $FS_{MP}(0,F)$ of all subject, done for all types of lineshapes, including SL, Lorentzian and sum of tow Lorentzians.

Potential effects of assumptions for the values of $R_{1,MP}$ and $FS_{MP}(0)$

115

A potential source for inaccuracies in the extracted parameters are incorrect assumptions for the values of $R_{1,MP}$ and $FS_{MP}(0)$. For the broadband SR experiment (Experiment I), $R_{1,MP}$=2.0 s^{-1} and $FS_{MP}(0)$=0.93 were assumed, and these may not be entirely accurate. We investigated the effect of changes in these values on the MP T_2 determined in Experiment II, based on subject and ROI averaged values of decay rates (λ_1, λ_2) and amplitudes (a_1, a_2) for all IR and SR experiments, which were fitted without using any assumption. By varying $R_{1,MP}$ from 1 to 3 s^{-1} and $FS_{MP}(0)$ from 0.8 to 1.0 respectively, and going through procedures described above, new T_2 values were found for both SL and Lorentzian lineshapes, and these were compared with the original values.

6.3 The spectral properties of MPs

Voxel-wise fitting of the 2-pool model (Eq. 6.1) to the IR and broadband SR data allowed robust extraction of the model parameters. ROI averaged results are shown in Fig. 6.2 and Table 6.1. A single set of rate constants (λ_1 and λ_2) fitted both IR and SR data well, as judged from the close fit to the data apparent in Fig. 6.2. The ROI-averaged values for $R_{1,WP}$, f, and k_{MW} were similar to those found in a previous study based on IR and SR measurements at 7 T (1).

With the voxel-wise fast (λ_1) and slow (λ_2) rate constants known, voxel-wise two-pool model fitting of $FS_{WP}(t)$ to the frequency-specific SR data yielded maps of coefficients $a_1(F)$ and $a_2(F)$, as exemplified in Fig. 6.3 (top two rows). Next, using Eq. 6.6, voxel-wise values for $a_1(F)$ and $a_2(F)$ were used to calculate $FS_{MP}(0,F)$, whose maps is shown as the bottom row of Fig. 6.3, and further ROI-averaged values for $FS_{MP}(0,F)$ were determined for each subject. Before proceeding with fitting line shapes to these data,

small adjustments to the data were made to correct for potential shifts in F due to instrument drift. These correction values $\Delta f_0(F)$ were small relative to the spectral range.

a

b
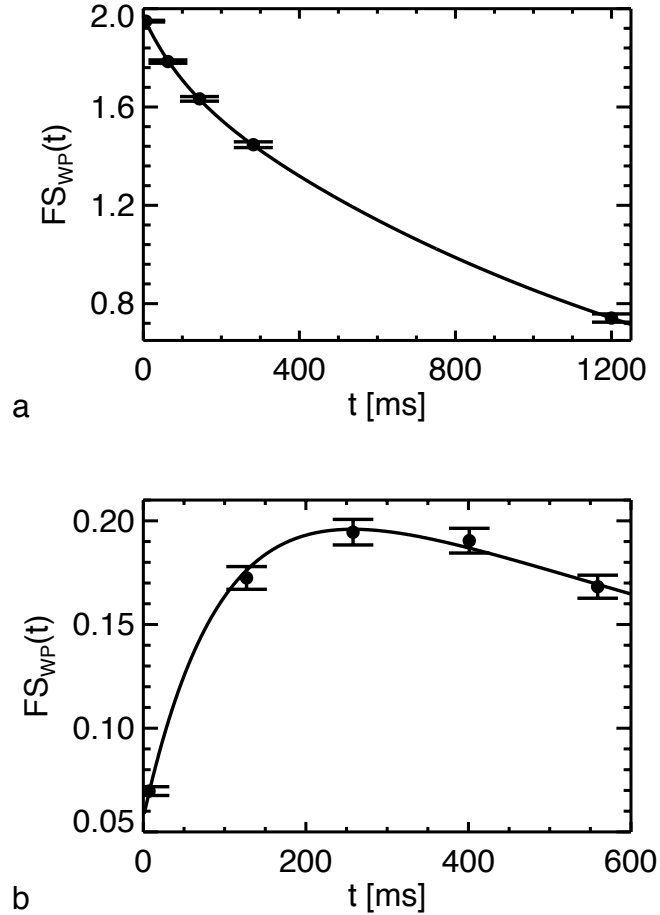
Figure 6.2 Two-pool model fitting (shown in lines) to subject and WM ROI averaged $FS_{WP}(t)$ (shown in dots) of IR (a) and broadband SR (b) experiments, with the error bars representing the standard deviations over subjects.

Table 6.1 Average (standard deviation) of the extracted two-pool model parameters in WM ROI's over subjects from Experiment I, with $R_{1, MP}$ assumed as 2.0 s^{-1} uniform across the brain for all subjects, as determined previously by van Gelderen et al (1,2); all rates are reported in s^{-1}; R^2 was adjusted for degrees of freedoms.

a_1(IR)	a_2(IR)	a_1(SR)	a_2(SR)	λ_1	λ_2	$R_{1, WP}$	$R_{1, MP}$	f	k_{WM}	k_{MW}	R^2
0.216	1.75	-0.197	0.254	9.95	0.716	0.363	2.0	0.250	2.07	6.21	0.99996
(0.009)	(0.01)	(0.010)	(0.010)	(0.32)	(0.015)	(0.010)		(0.012)	(0.13)	(0.25)	(1 x 10^{-5})
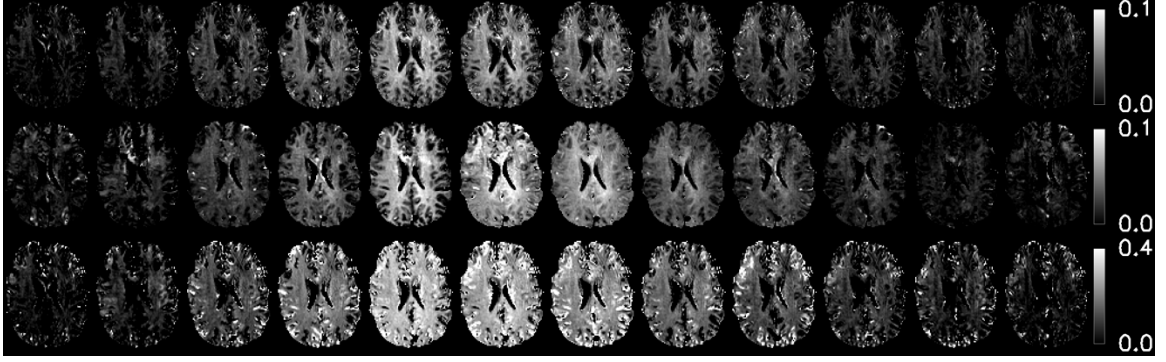
Figure 6.3 Examples of maps of $-a_1$(F) (first row) and a_2(F) (second row), and FS_{MP}(0,F) (third row), for the frequency-specific SR data fit, at different frequency F (from left to right: -16, -8, -4, -2, -1, -0.5, 0.5, 1, 2, 4, 8, 16 kHz); the bright spots are created by amplification of noise in regions with low signal, through the data processing.

Table 6.2 summarizes the results of fitting a SL (Eq. 6.7), Lorentzian (Eq. 6.8), and sum of two Lorentzians to subject-wise ROI-averaged FS_{MP}(0,F). $T_{2,SL}$ of 9.6±0.6 μs and ΔF_{SL} of -773±14 Hz (-2.58±0.05 ppm), and $T_{2,L}$ of 65±2 μs and ΔF_L of -727±28 Hz (-2.42±0.09 ppm) were found for SL and Lorentzian fitting respectively. For the two-Lorentzian fit, a common ΔF_L of -727 Hz (-2.42 ppm) determined from the single Lorentzian fit was used. This fitting resulted in a 74±3% fraction of MPs with a T_2 of 23±5 μs, and a 26±3% fraction with a T_2 of 124±13 μs. Judging from the R^2 (adjusted for degrees of freedoms) values, the SL and sum of two Lorentzians had similar performance in the fitting, and both provided better fit than Lorentzian.

Table 6.2 Results of T_2, ΔF and R^2 (adjusted for degrees of freedoms) for fitting of SL, Lorentzian and sum of two Lorentzians lineshapes to FS_{MP}(0,F) data, report in the form of subject average±(standard deviation over subjects); for sum of two Lorentzians fit, a common ΔF_L for both Lorentzians was assumed to be -727 Hz (-2.42 ppm), identical to that obtained from the single Lorentzian fit. The component with T_2 of 23±5μs, composes 74±3% of the total MPs, and the other component with T_2 of 124±13 μs composing the rest.

	SL	Lorentzian	Sum of 2 Lorentzians
T_2 (μs)	9.6±0.6	65±2	23±5/124±13
ΔF (Hz)	-773±14	-727±28	-727
R^2	0.982±0.005	0.939±0.013	0.989±0.003

SL and Lorentzian fits to ROI averaged $FS_{MP}(0,F)$ data were also performed on all subjects jointly (but without averaging over subjects, since $\Delta f_0(F)$ is different across subjects). This is shown in Fig. 6.4a, yielding $T_{2,SL}$ of 9.5 µs and ΔF_{SL} of -781 Hz (-2.60 ppm) for the former, and $T_{2,L}$ of 65 µs and ΔF_L of -726 Hz (-2.42 ppm) for the later. Fitting to the same data using sum of two Lorentzians, resulted in $T_{2,L}$'s of 23 µs (73%) and 122 µs (27%), as shown in Fig. 6.4b.
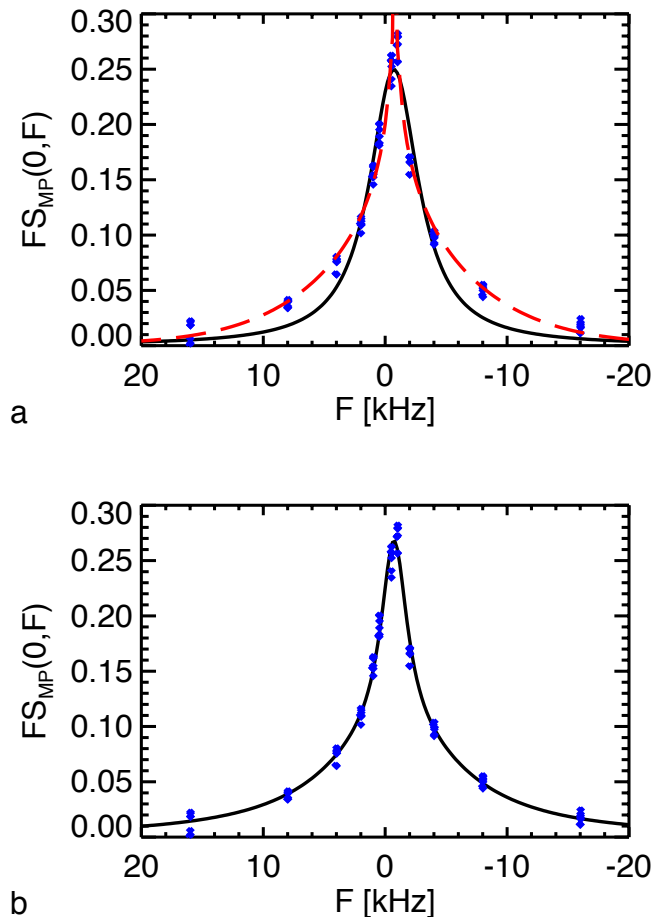
Figure 6.4 A SL lineshape (shown as the red dashed curve in a) and a Lorentzian lineshape (shown as the black solid curve in a) fitting to the WM ROI averaged $FS_{MP}(0,F)$ of all subjects jointly (shown in blue dots); sum of two Lorentzians (shown as the curve in b) fits to the same data (shown in blue dots).
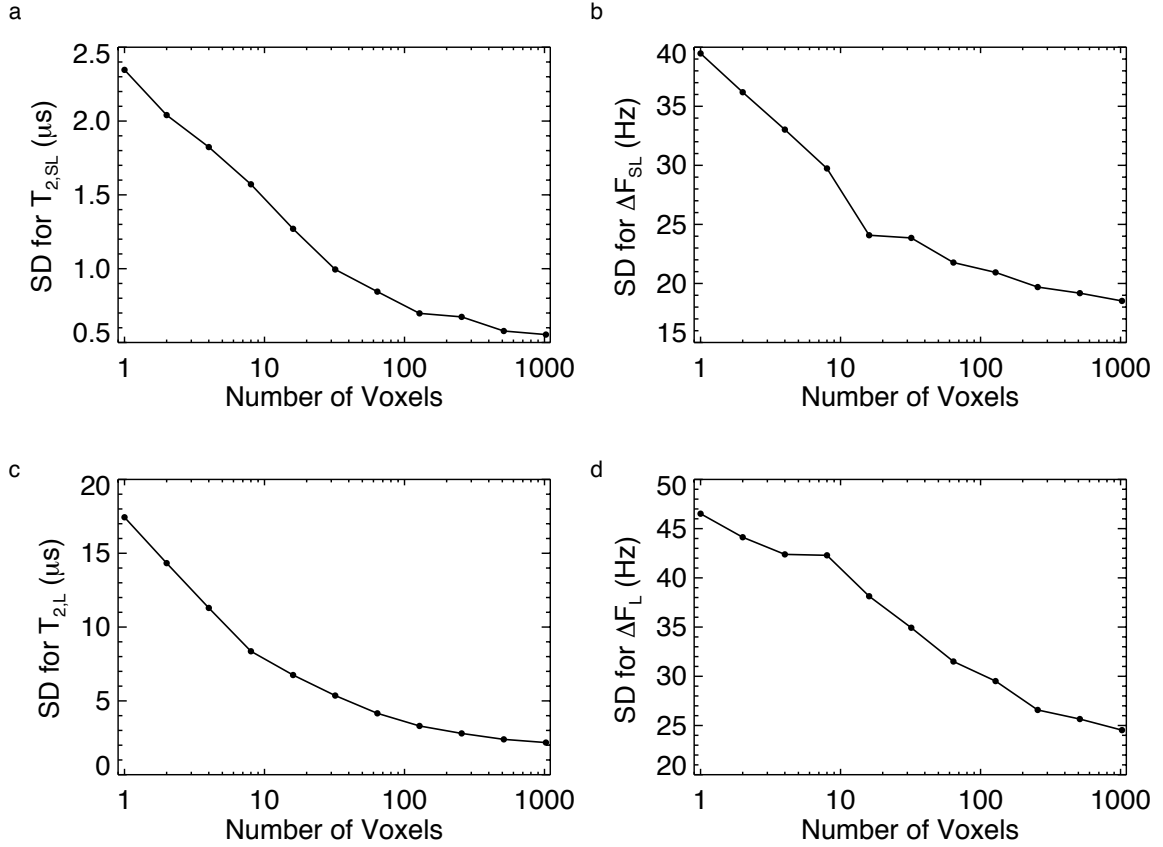
Figure 6.5 Standard deviations (SDs) of $T_{2,SL}$ (a), ΔF_{SL} (b), $T_{2,L}$ (c), and ΔF_L (d), calculated over 7 subjects and 50 random selections of voxels within WM region for each subject, as functions of number of voxels.

Fig. 6.5 shows the standard deviations (SDs) of T_2 and ΔF over 7 subjects and 50 random selections of voxels within the WM region for each subject, as functions of number of voxels, which included 1024, 512, 256, 128, 64, 32, 16, 8, 4, 2, 1, for both SL and Lorentzian fitting. As can be seen, the standard deviations for $T_{2,SL}$, ΔF_{SL}, $T_{2,L}$, and ΔF_L all increase, as the number of selected voxels decreases. And even with only one voxel selected for each subject, the standard deviations of $T_{2,SL}$, ΔF_{SL}, $T_{2,L}$, and ΔF_L are all less than 30% of their respective average values, as shown in Table 6.2. Therefore, our method to fit T_2 and ΔF also works for reduced number of voxels included in ROI, but at the penalty of greater uncertainty.

Assuming the total variance $V_t (= SD^2)$ is equal to the sum of inter subject variance V_i and variance from the image noise V_n/N: $V_t(N) = V_i + V_n/N$, with N as the number of voxels selected. Then we have $V_t(1) = V_i + V_n > V_n$ and $V_t(1024) = V_i + V_n/1024$. As can be seen from Fig. 6.5, $V_t(1)/1024$ and $V_n/1024$ $(< V_t(1)/1024)$ for $T_{2,SL}$, ΔF_{SL}, $T_{2,L}$, and ΔF_L are all negligible compared to $V_t(1024)$, we then have $V_t(1024) \approx V_i$. Therefore, the SDs at $N = 1024$ $(= \sqrt{V_t(1024)} = \sqrt{V_i})$ may only reflect the inter subject variability. And all SDs at $N = 1024$ shown in Fig 6.5 are close to those reported in Table 6.2, where N ranges from 2648 to 5580 for different subjects.

After subtraction of the fitted (symmetric) lineshapes from the spectral data, residual signal appears small for the SL fit (Fig. 6.5a), and the fit of two Lorentzians (Fig. 6.5c). The small residuals and the absence of any clear asymmetry in their distribution is consistent with expected suppression of CEST effects, and associated asymmetries, with the measurement approach followed here. However, deviation of the residuals from zero is obvious for the Lorentzian fit (Fig. 6.5b), confirming previous steady state MT studies (63,70,135,136) where SL provided a fit superior over a Lorentzain lineshape.
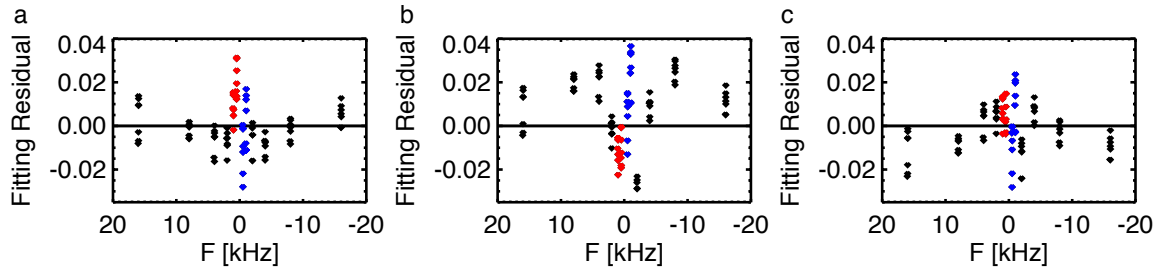
Figure 6.6 Residuals for the SL fit (a), single Lorentzian fit (b), and sum of two Lorentzians fit (c) subtracted from the WM ROI averaged $FS_{MP}(0,F)$ of all subjects (shown in dots), with data in range of 0 Hz$<F<$1500 Hz marked in red and -1500 Hz$<F<$0 Hz marked in blue.

Results of the simulations performed to investigate the influence of the B_1 amplitude on inferred T_2 are shown in Fig. 6.6. As expected, for an actual MP T_2 ($T_{2,\text{input}}$) of 65 μs, the inferred T_2 ($T_{2,\text{output}}$) drops precipitously with RF power (Fig. 6.6b). However, at the experimental B_1 amplitude of 200 Hz, this drop remains limited: the $T_{2,\text{output}}$ of 60 μs underestimates $T_{2,\text{input}}$ by 5 μs, i.e. less than 10%. According to Fig. 6.6b, variation of B_1 by 25 Hz results in an error in the estimation of $T_{2,\text{output}}$ on the order of 1 μs, which suggest a low sensitivity to B_1 inhomogeneity. Similarly, at other values of $T_{2,\text{input}}$, and B_1 =200 Hz, the difference between $T_{2,\text{input}}$ and $T_{2,\text{output}}$ remains modest (Fig. 6.6c).

The extracted MP T_2 values proved robust against small changes in assumed values for $R_{1,MP}$ and $FS_{MP}(0)$. Changing $R_{1,MP}$ from 1 to 3 s^{-1} resulted in very little change in $FS_{MP}(0,F)$. For the SL lineshape, $T_{2,\text{SL}}$ changed from 9.4 to 9.3 μs, while for the Lorentzian, $T_{2,\text{L}}$ changed from 65 to 64 μs. Changes of $FS_{MP}(0)$ from 0.8 to 1.0 resulted in a similar $T_{2,\text{SL}}$ in the range of 9.3-9.4 μs, and $T_{2,\text{L}}$ remained at a constant value of 64 μs, although increasing $FS_{MP}(0)$ of the broadband SR experiment results in increased $FS_{MP}(0,F)$.

6.4 Discussion and comparison with previous MP spectral studies

In order to aid interpretation of MT contrast at high field, we investigated MP spectral characteristics in human brain WM at 7 T. For this purpose, we used a dedicated indirect measurement approach that minimized direct saturation of WPs, CEST effects, and tissue heating, problems often associated with the generation of MT contrast in-vivo. We found that at 7 T, the MP spectrum is well represented by a symmetric, SL lineshape

with a time constant $T_{2,SL}$ of 9.6±0.6 μs, and shifted by -2.58±0.5 ppm relative to the water resonance. As will be discussed in the following, these results are consistent with previous findings and mechanistic interpretations of MT from studies at lower field and point to dipolar coupling between methylene protons as a major determinant of the MP spectral characteristics. We anticipate that these values for the MP spectral characteristics will help design and quantification of future MT studies at 7T.
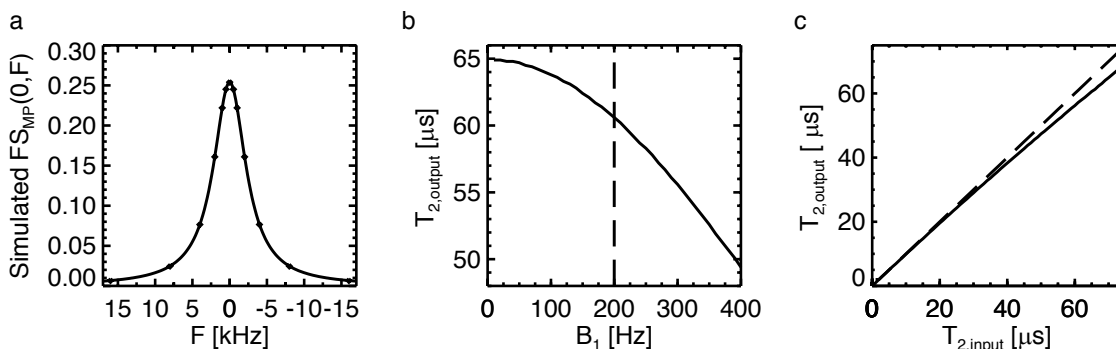
Figure 6.7 Simulations of influence of B_1 amplitude on inferred T_2: (a) Lorentzian fit (the curve) to simulated $FS_{MP}(0,F)$ (the dots) of MP pool with $T_{2,input}$ of 65 μs, using Bloch equation, under the influence of frequency-specific hyperbolic secant pulses with B_1 of 200 Hz, a common pulse duration of 12 ms, resulting in a $T_{2,output}$ of 60 μs; (b) B_1 dependence of $T_{2,output}$ by varying B_1 while keeping $T_{2,input}$ fixed as 65 μs; (c) $T_{2,input}$ dependence of $T_{2,output}$ by varying $T_{2,input}$ while keeping B_1 fixed as 200 Hz.

As has been found with previous indirect measurement of MP spectral characteristics at 1.5 T and 3 T, (26,63,135,136) the 7 T data could be reliably fit with a SL lineshape. This is consistent with a dipolar coupling mechanism in semi-solids such as membrane proteins and lipids (26,60,102,153). In addition, it was found that the 9.6 μs $T_{2,SL}$ at 7 T was similar to the 9.2 μs - 13.1 μs range of values found in previous studies at lower fields between 0.5 T and 3 T (40,63,66,135,136). Like the SL lineshape, the field independence of the linewidth is suggestive of a dominant contribution of dipolar coupling, rather than width being determined by chemical shift differences between the

[1]H species contributing to MT (111). Previous direct measurements of MP spectral characteristics on fixed human WM tissue samples have found 50- 65 μs for $T_{2,\mathrm{L}}$ (58,59) at 7 T and 4.7 T. These values were based on Lorentzian lineshapes, and translate into $T_{2,\mathrm{SL}}$ values of 16-21 μs for SL lines of the same FWHM. These ex-vivo Lorentzian linewidths therefore are quite consistent with the in-vivo values, especially when considering the differences in measurement conditions.

Our MT study at 7 T found that the center of the MPs spectrum is shifted upfield relative to the resonance frequency of WPs by -2.58 ppm. This result agrees well with values of -2.34 ppm previously reported at 3 T (66), and the -2.55 ppm reported in WM of cat brain at 4.7 T (67). Combined, these studies show that the absolute spectral frequency shift is proportional to field strength, an observation consistent with a chemically shifted proton species contributing to MT. The value of the shift is somewhat smaller than the range of -3.2 to -3.9 ppm measured for methylene protons, the dominant proton species in myelin (35). While methylene protons are most abundant in WM (59), a not insignificant contribution to our MT signal may have come from, more downfield shifted proton species (e.g. in proteins and smaller molecules). These protons, while measured together with the methylene protons, may shift the combined spectral line downfield from the -3.2 to -3.9 ppm range.

To the extent that MT is caused by methylene protons in myelin lipids, their substantial orientational order may introduce a dependence of spectral linewidth on the direction of white matter fibers relative to the magnetic field. In fact, a recent study found that $T_{2,\mathrm{SL}}$ may vary between 12 and 15 μs, dependent on fiber orientation (102). Due to lack of information about fiber orientation, we could not confirm this dependence in our

own data. Nevertheless, if confirmed, a fiber-orientation dependent MP T_2 would further underscore the importance of the dipolar coupling mechanism for the apparent MP T_2, and furthermore predict an orientation dependence of MT effects. Similarly, since the effect of an inversion RF pulse on MP magnetization depends on MP spectral characteristics (2), orientation dependence of MP T_2 may also render apparent T_1 (as measured from an IR experiment (2)) orientation dependent.

An advantage of the proposed method for the measurement of MP characteristic is the insensitivity to CEST effects, which can substantially contribute to so called "z-spectra" typically acquired to quantify MT effects (66,147,154), and thus confound interpretation. When generating MT contrast with seconds-long RF irradiation, MT from exchangeable protons can reduce the amplitude of the WP signal by as much of 2-4%, which is substantial when considering that typical asymmetry in z-spectra due to non-exchanging protons is only on the order of 1-2% (66). Although currently several approaches exist to distinguish CEST from other (non-exchange) MT effects (138,154,155), CEST effects were not explicitly excluded from z-spectrum asymmetry quantifications reported previously (66,67). Nevertheless, it appears that the quantitative shifts characterizing this asymmetry are quite similar between the proposed and previous methods and amount to about -2.6 ppm.

A potential source for inaccurate quantification of MP spectral characteristics with the proposed method is the potential dependence on RF irradiation strength (B_1 amplitude). Preliminary experimental study of effects of B_1 on the spectrum measurement was performed on two subjects in a similar manner as described above. Experiment I was done in exactly the same way as described in Method for both subjects. In Experiment II,

multiple B_1's were used for the frequency-specific SR experiment, to quantify the B_1 dependence of ROI averaged $FS_{MP}(0,F)$. In lack of a rigorous way to do the simulation based on a SL lineshape (134) as mentioned above, attempts were made to simulate these data using single Lorentzian and a combination of multiple Lorentzians respectively, however no close fit was found. This may reflect the intrinsic insufficiency of a Lorentzian lineshape to represent the underlying interaction between the immobile MPs. The situation may be further complicated by the existence of multiple MP species, each with a SL lineshape centered on a different resonance frequency (35). Thus, while our spectral measurements provide a measure of linewidth and chemical shift, both of which provide insights into the molecular source of MT in white matter, uncertainty remains about the precise lineshape.

The similar failure to simulate dependence of the saturation effects of MPs on B_1 was also found in our study on a marmoset brain *in vivo* reported in Chapter 4 and on a fixed marmoset brain *ex vivo* reported in Chapter 5. As discussed in Section 5.4, the study Chapter 5 provided improved estimation of MT parameters than Chapter 4, therefore we will only compare the results between Chapter 5 and this study here. In this study, we found MP T_2 of 65 μs for human brain WM *in vivo* assuming a Lorentzian lineshape, while in Chapter 5, MP T_2 was found to be 36 μs for WM. The fractional saturations $FS_{MP}(0,F)$, as shown in Fig. 6.4a, are less than 0.3 for all frequency offsets, whereas in Chapter 5 the fractional saturations $FS_{MP}(0,B_1)$, as shown in Fig. 5.4, ranged from 0.3 up to 1.0. Therefore, this study is less subject to influence from the nonlinear relation between saturation effects on MPs and the RF power (137,138), and the reported MP T_2 is more reliable than that in Chapter 5.

The skin depth, δ, for the RF pulses can be calculated using the following formula:

$$\delta = \sqrt{\frac{2\rho}{\omega\mu}}\sqrt{\sqrt{1 + (\rho\omega\varepsilon)^2} + \rho\omega\varepsilon} \qquad (\,6.9\,)$$

Here $\rho= 1.49$ $\Omega\cdot$m is the resistivity of brain tissue (156), $\omega=2\pi*300$ MHz is the angular frequency of resonance at 7 T, $\mu=1.26*10^{-6}$ N$\cdot$A^{-2} is the magnetic permeability, and $\varepsilon=4.6*10^{-10}$ F/m is the permittivity at 7 T (140). This results in a δ of 6 cm, compared to the typical adult head's diameter of 16 cm (156). However, in practice, multiple RF coils are posited around the head of a subject, in a cylindrical shape. The coils create cylindrical RF field with the highest B_1 at the center, as shown in previous studies (156), providing enough RF amplitude to image the whole brain.

A novel approach was introduced to study MPs spectral characteristics while minimizing effects of RF-related tissue heating, direct saturation of WPs and CEST effects. Applied to WM in human brain at 7 T, MPs were found to have a symmetric, SL lineshape with a $T_{2,\mathrm{SL}}$ of 9.6 μs and an resonance frequency ΔF_{SL} of -773 Hz (-2.58 ppm), consistent with previous results at low field, and consistent with a previously suggested major contribution of dipolarly-coupled lipid methylene protons. These results, as well as the proposed measurement approach, are expected to facilitate the use and interpretation of quantitative MT approaches at high field.

Chapter 7: Combination of MT and R_2^* measurements to distinguish between contributions of semisolids and iron to R_1

In human brain, the apparent longitudinal relaxation rate (R_1) primarily originates from magnetization transfer (MT) effects associated with the macromolecular ^{1}H-proton (MP) fraction (f), as demonstrated in Chapter 3. However, in iron-rich regions, the iron concentration may contribute significantly as well (33). To quantify the relative contributions of iron and macromolecules at 7 T, we measured f and R_1 of water protons ($R_{1,WP}$) corrected for MT effects, using the methods described in Chapters 2 & 3. Using values of brain iron levels from literature, the relationship between iron concentration, R_1, and R_2^* was investigated and found to be approximately linear. The results indicate that the combination of R_2^* and MT measurements may provide a sensitive means to quantify $R_{1,WP}$, f and iron concentration.

7.1 *Correlations of the apparent R_1 with iron concentration*

Previous studies have shown that R_1 contrast in brain is predominantly determined by the macromolecular ^{1}H-proton (MP) fraction f (2,33). Therefore, methods (1,45,50) based on monitoring the longitudinal relaxation of water ^{1}H-protons (WPs) followed by a two pool, i.e., WPs and MPs, exchange model analysis have been used (2,45,50) to estimate f. However, these studies generally require extensive experiments to solve for the unknown parameters in the two-pool model, often requiring a number of simplifying assumptions (1,45,50), as discussed in Chapter 1. These assumptions may not be correct in regions with high iron concentration. For example, iron may affect the intrinsic R_1 of WPs ($R_{1,WP}$) in the absence of MT effects and in iron-rich brain regions the iron

concentration has been found to correlate with the apparent R_1 (33). Here, we applied a previously introduced pulsed MT method to measure $R_{1,WP}$, described in Chapters 2-3 and correlated it with R_2^* as a surrogate indicator of iron concentration, as well with putative iron concentrations derived from previously published histological measurements (78,79).

7.2 *Two-pool exchange model and MRI measurements*

MRI experiments were performed on seven human subjects (ages 23-49, average age 32.3, 3 females), scanned under an IRB approval on a 7 T Siemens scanner. This study included measurement of $R_{1,WP}$, And R_2^* was measured using a MGRE sequence. Details of experiments and data processing procedure are described below.

Measurement of $R_{1,WP}$

$R_{1,WP}$ was measured using the same procedure as presented in subsections of *Experiment I: Determination of MT parameters* and *Image acquisition* in Chapter 6. Basically, two types of preparation pulses, namely a WP inversion recovery (IR) pulse and a composite broadband MP saturation recovery (SR) pulse, were used to saturate the two pools to different extents. This was followed by EPI image acquisition at variable delay t, to sample $FS_{WP}(t)$, as shown in Eq. 1.12. (Refer to the two relevant subsections in Chapter 6 for details.)

Measurement of R_2^*

R_2^* was measured using a MGRE sequence with TR of 1 s, TE of 3.2 ms, 28 even echoes with spacing of 1.54 ms, the same resolution and field-of-view as the EPI scans, and 2 repetitions.

Data Analysis

Pre-processing

Pre-processing of MGRE images for R_2^* determination included removing both constant phase and linear phase drift for all echoes, such that only the dephasing induced by the local magnetic field inhomogeneity was kept. The magnitude values of these images were used for R_2^* fitting. On EPI images, distortion due to B_0 inhomogeneity was corrected by subtraction of a linear phase from the EPI images, calculated by fitting a linear phase drift through echoes using the MGRE images. Then all MGRE and EPI images were registered to correct only for in-plane motion, since the small number of slices did not support through-plane motion correction. For IR images, polarity correction was performed for their magnitude data, based on the phase difference between the IR images with the (un-inverted) reference image, to correct for signal rectification during the complex-to-magnitude conversion. Then averaging over repetitions was performed for all images. FS_{WP}(t) as expressed in Eq. 1.12 was calculated by dividing each IR image by the corresponding reference image (i.e., data acquired without inversion pulse). Analogous analysis was performed for the SR data, however without performing the signal polarity adjustment. All processing was done in IDL (Exelsis Visual Information Solutions, Boulder, CO, USA).

Voxel-wise determination of R_2^*

A single exponential decay, as shown in Eq. 7.1, was fitted to the magnitude data of the images acquired using the MGRE sequence, in a voxel wise fashion.

$$M_\perp(t) = M_{\perp0}e^{-R_2^*t} \qquad\qquad (7.1)$$

Here, t is the time of each echo, $M_\perp(t)$ is the magnitude of the corresponding transverse magnetization at echo time t, and $M_{\perp0}$ is the magnitude of the initial transverse magnetization at $t = 0$. The first 3 echoes were dropped, and only echo times

130

between 7.8 ms to 44.8 ms (including 25 echoes) were used for the fitting, to avoid influence from the fast decaying myelin water component, whose T_2^* is on the order of 7 ms (72).

Voxel-wise determination of $R_{1,WP}$

To determine λ_1, λ_2, k_{WM}, k_{MW} and $R_{1,WP}$, both the IR and the SR data were fitted to the two-pool exchange model, on a voxel-wise basis, following these steps:

(a) Fit Eq. 1.12 to the IR and SR data jointly, yielding one pair of decay rates (λ_1, λ_2) and two pairs of amplitudes (a_1, a_2) for each voxel.

(b) Assuming $R_{1,MP}=2$ s^{-1} and $FS_{MP}(0)$ for the SR experiment to be 0.93 as determined previously (2), calculate k_{WM}, k_{MW}, $R_{1,WP}$, using Eqs. 1.10 & 1.14, based on the decay rates and amplitudes found in Step (a).

ROI selection

Four ROI's were drawn in Caudate nucleus (CN), Putman (PUT), Thalamus (TH) and Frontal white matter (FWM), as exemplified by Fig. 7.1.
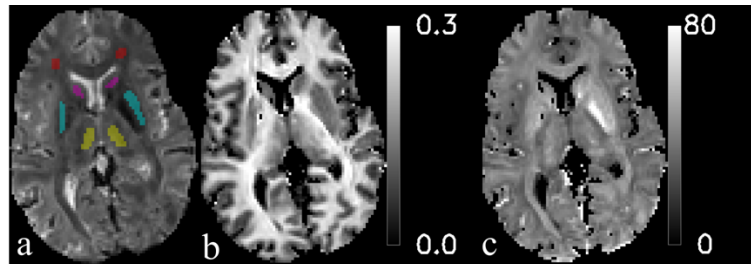
Figure 7.1 Example of hand drawn ROI's (a) on Caudate Nucleus (CN) (pink), Putamen (PUT) (green), Thalamus (TH) (yellow) and Frontal White Matter (FWM) (red). ROI locations are shown superimposed on a MGRE image at echo time of 32.5 ms, together with the corresponding f (b) and R_2^* (c) maps.

Estimation of iron concentration

Iron concentration in the four ROI's was calculated using formulae published in a study by Hallgren et al. (79) as follows:

Caudate nucleus: $y = 96.6(1 - \exp(-0.05x)) + 3.3$ $\qquad$ (7.2)

Putman: $y = 146.2(1 - \exp(-0.04x)) + 4.6$ $\qquad$ (7.3)

Thalamus: $y = 141.9 \exp(-0.013x) - 134.4 \exp(-0.0439x)$ $\qquad$ (7.4)

Frontal white matter: $y = 39.5(1 - \exp(-0.10x)) + 3.1$ $\qquad$ (7.5)

where y is the fresh weight concentration of non-heme iron in parts per million (ppm), and x is the age of the subject in years. In Hallgren et al.'s original report (79), no formula was provided for TH, but the TH data was later fitted to a bi-exponential model as shown in Eq. 7.4 reported in another study (78).

Correlation of R_2* with putative iron concentration and MP fraction

The subject-wise ROI-averaged correlations between $R_{1,WP}$ and the iron concentration, between $R_{1,WP}$ and R_2*, and between R_2* and the iron concentration were studied using linear regression, respectively.

7 .3 Correlation of $R_{1,WP}$ with R_2* and putative iron concentration

Table 7.1 shows the fitting results of R_2*. Results on the two-pool model parameters fitting, including f and $R_{1,WP}$, are shown in Table 7.2. The fittings of R_2* and $R_{1,WP}$ are both robust, as demonstrated by the adjusted R^2 values in Table 7.1-7.2.

Linear regression of R_2* with the iron concentration gives: $R_2^*(C_{Fe}) = 0.218 C_{Fe} + 28.1$ with adjusted R^2 of 0.79, where C_{Fe} is the fresh weight concentration of non-heme iron in parts per million (ppm). Linear regression of $R_{1,WP}$ with the iron concentration gives: $R_{1,WP}(C_{Fe}) = 0.00118 C_{Fe} + 0.33$ with adjusted R^2 of 0.78. And linear regression of $R_{1,WP}$ with R_2* gives: $R_{1,WP}(R_2^*) = 0.00433 R_2^* + 0.22$ with adjusted R^2 of 0.60. These three correlations are shown in Fig. 7.2.

Table 7.1 ROI averaged R_2^* (in Hz), averaged (±standard deviation) over all subjects; R^2 was adjusted for degrees of freedom.

	CN	PUT	TH	FWM
R_2^*	45±5	51±5	40±3	38±2
R^2	0.997±0.004	0.999±0.001	0.999±0.001	0.994±0.005

Note: Caudate Nucleus (CN), Putamen (PUT), Thalamus (TH) and Frontal White Matter (FWM)
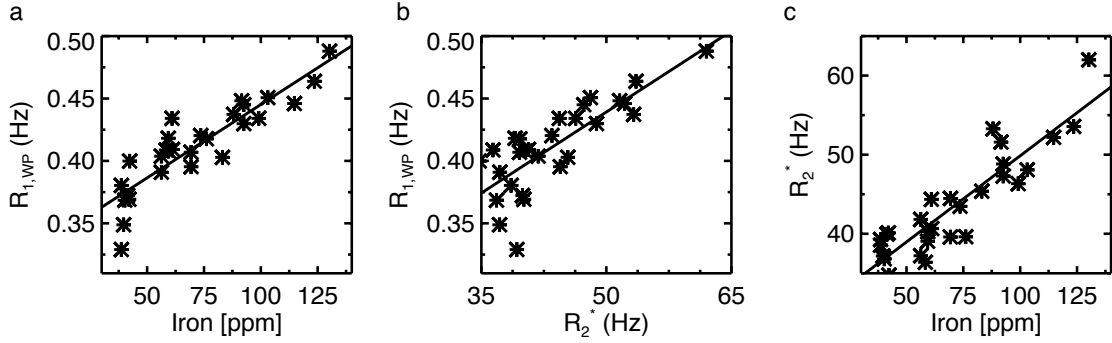
Figure 7.2 Linear correlations between $R_{1,WP}$ and iron concentration (a), between $R_{1,WP}$ and R_2^* (b), and between R_2^* and iron concentration (c), with iron concentration as weight fraction.

7.4 Comparison and discussion

As shown in Table 7.2, $R_{1,WP}$ varies from 0.37 to 0.45 s^{-1} in all ROI's. Taking parameters from TH as an example, varying $R_{1,WP}$ from 0.37 to 0.45 s^{-1}, but keeping other parameters unchanged, results in change of 0.0097 s^{-1} in λ_1 and 0.0702 s^{-1} in λ_2, corresponding to 0.2% and 10.5% of λ_1 and λ_2 respectively. This is in agreement with a report by Rooney et al. (29) that, in iron-rich regions, iron concentration accounts for 10-20% change in the apparent R_1.

R_2^* is found to linearly correlate with the iron concentration, consistent with previous reported linear correlation of R_2^* with iron (157–159). Importantly, R_2^* can be used to reliably estimate $R_{1,WP}$ to reduce the number of unknowns in Eqs. 1.10-1.14 and

can possibly be used to facilitate the extraction of two-pool exchange model parameters,

including MP fraction.

Table 7.2 Average (standard deviation) of the ROI averaged two-pool model parameters over subjects, where $R_{1,MP}$ was assumed as 2.0 s^{-1} uniform for all brain regions, as determined previously (1,2); all rates are reported in s^{-1}; R^2 was adjusted for degrees of freedoms.

ROI	a_1(IR)	a_2(IR)	a_1(SR)	a_2(SR)	λ_1	λ_2	$R_{1, WP}$	$R_{1, MP}$	f	k_{WM}	k_{MW}	R^2
CN	0.08	1.86	-0.08	0.14	15.3	0.56	0.42	2.0	0.10	1.27	12.2	0.9998
	(0.01)	(0.02)	(0.01)	(0.01)	(2.6)	(0.01)	(0.02)		(0.01)	(0.19)	(2.4)	(0.0001)
PUT	0.08	1.85	-0.09	0.16	12.6	0.60	0.45	2.0	0.11	1.20	9.6	0.9998
	(0.01)	(0.01)	(0.01)	(0.01)	(2.0)	(0.02)	(0.02)		(0.01)	(0.20)	(1.8)	(0.0001)
TH	0.10	1.85	-0.12	0.20	11.4	0.63	0.41	2.0	0.16	1.53	8.1	0.9997
	(0.01)	(0.01)	(0.01)	(0.01)	(0.9)	(0.02)	(0.01)		(0.01)	(0.12)	(0.8)	(0.0001)
FWM	0.24	1.72	-0.20	0.26	9.37	0.72	0.37	2.0	0.26	1.97	5.8	0.9999
	(0.02)	(0.03)	(0.01)	(0.01)	(0.52)	(0.02)	(0.02)		(0.02)	(0.13)	(0.4)	(0.0001)

Note: Caudate Nucleus (CN), Putamen (PUT), Thalamus (TH) and Frontal White Matter (FWM)

Chapter 8: Summary

In summary, this dissertation presents our quantitative study of the mechanisms of T_1 relaxation in brain MRI, with an emphasis on understanding the contribution from magnetization transfer. Properties of MPs, including their relative concentration, their exchange rate with WPs, T_2, lineshape, and resonance frequency are extensively investigated. Our approach, based on transient MT followed by two-pool exchange model fitting, has much lower RF power deposition than conventional MT methods and thus can be applied safely on human *in vivo*, even at high field strength.

The two-pool exchange model, as introduced in Section 1.2, proves to fit robustly to the longitudinal magnetization relaxation of WPs for all three types of tissues, including human brain *in vivo*, marmoset brain *in vivo*, and fixed marmoset brain *ex vivo*. The recovery of WP longitudinal magnetization is confirmed to follow a bi-exponential evolution, with two distinct rate constants, which are different from the intrinsic R_1's (=1/T_1) of WPs and MPs. T_1 contrast is dominated by MT between WPs and MPs (2).

Through the study of MT, we quantified the properties of MPs in human brain *in vivo*, including their relative fraction, exchange rate with WPs, based on experiments using high B_1 RF pulses to achieve almost complete saturation on MPs, followed by two-pool exchange model analysis. This method provides a fast and practical way to measure MP fraction and to quantify contribution of MPs to T_1 contrast. MPs were found to constitute up to 27% of total ^{1}H protons in human brain white matter, which is consistent with previous reports based on chemical analysis (36) and MRI based proton density studies (81,126).

For the first time, we demonstrated a novel approach to investigating the spectral properties of MPs *in vivo* at high field, including the lineshape, T_2, and resonance frequency. This was achieved by applying low-power RF pulses at different frequency offsets and using a two-pool exchange model to account for the direct saturation effect on WPs. CEST effects, which can be magnified by applying long RF pulses and often confound the steady state MT experiments, are minimized in our method through using RF pulses with short pulse duration. We have shown that in white matter, at 7 T, the MP spectrum can be approximated using a super-Lorentzian line with a resonance frequency of -2.58±0.05 ppm, and a transverse relaxation time constant T_2 of 9.6±0.6 μs, which is consistent with previous results *in vivo* at lower field strength (66,136). The measured spectral properties of MP together with the understanding of MT, can serve as predetermined knowledge for interpretation of other studies of MT and CEST, can help better understand MRI contrasts, and can further be useful for developing new MRI techniques at high field.

Our method of measuring MP fraction can potentially be used to study brain tissue changes in neurodegenerative diseases (160), such as multiple sclerosis and Parkinson's disease. These diseases are found to be associated with loss of myelin, which constitutes most of the MP content in WM (35), functions as insulating layers surrounding axons (86,144), and is essential for neural signal transmission. Previous studies (93) have shown that MS lesions have lower MP fraction than healthy brain tissue. Compared to the conventional z-spectra method (54,136), our way to measure MP fraction is fast and the fitting to the two-pool exchange model is robust. However, our method must be expanded from the current two-dimensional image acquisition to three-dimensional image

acquisition if it is to be applied for clinical diagnosis and for monitoring the process of treatment. This is currently being investigated.

The work presented in Chapter 7 demonstrated the linear correlation between the intrinsic longitudinal relaxation rate of WPs, $R_{1,WP}$, with the transverse relaxation rate, R_2^*. Therefore, when using the two-pool exchange model as introduced in Section 1.2, instead of fitting $R_{1,WP}$ as an independent parameter, it can be estimated using R_2^*, which can be quickly and reliably determined using a MGRE sequence. In this case, only three independent parameters have to be fitted as discussed in Section 1.2, and only MP saturation pulses are needed for measurement of MP fraction, as discussed in Chapter 2 (1). This will further save the scanning time and make the two-pool exchange model more reliable for studying the MP fraction, making our method more feasible for clinical applications.

Bibliography

1. van Gelderen P, Jiang X, Duyn JH. Rapid measurement of brain macromolecular proton fraction with transient saturation transfer MRI. Magn. Reson. Med. [Internet] 2016:n/a--n/a. doi: 10.1002/mrm.26304.

2. van Gelderen P, Jiang X, Duyn JH. Effects of magnetization transfer on T1 contrast in human brain white matter. Neuroimage [Internet] 2015;128:85–95. doi: 10.1016/j.neuroimage.2015.12.032.

3. Jiang X, Gelderen P van, Li X, Leibovitch E, Sati P, Silva AC, Duyn JH. Study of Bound Proton T2 and Magnetization Transfer using Pulsed MT. In: ISMRM 23rd Annual Meeting. ; 2015. p. 5530.

4. Jiang X, van Gelderen P, Duyn JH. Measurement of the Resonance Frequency of Macromolecular Protons in Brain. In: ISMRM 24th Annual Meeting. ; 2016. p. 1502.

5. Lauterbur PC. Image Formation by Induced Local Interactions: Examples Employing Nuclear Magnetic Resonance. Nature [Internet] 1973;242:190–191. doi: 10.1038/242190a0.

6. Brown RW, Cheng Y-CN, Haacke EM, Thompson MR, Venkatesan R. Magnetic Resonance Imaging: Physical Principles and Sequence Design. Second Edi. John Wiley & Sons Ltd; 2014. doi: 10.1063/1.3554697.

7. Marques JP, Kober T, Krueger G, van der Zwaag W, Van de Moortele P-F, Gruetter R. MP2RAGE, a self bias-field corrected sequence for improved segmentation and T1-mapping at high field. Neuroimage 2010;49:1271–1281. doi: 10.1016/j.neuroimage.2009.10.002.

8. Mugler JP, Brookeman JR. Three-dimensional magnetization-prepared rapid gradient-echo imaging (3D MP RAGE). Magn. Reson. Med. 1990;15:152–157. doi: 10.1002/mrm.1910150117.

9. Levitt MH. Spin dynamics: basics of nuclear magnetic resonance. 2010.

10. Kalk A, Berendsen HJ. Proton magnetic relaxation and spin diffusion in proteins. J. Magn. Reson. [Internet] 1976;24:343–366. doi: 10.1016/0022-2364(76)90115-3.

11. Helms G, Hagberg GE. In vivo quantification of the bound pool T1 in human white matter using the binary spin-bath model of progressive magnetization transfer saturation. Phys. Med. Biol. [Internet] 2009;54:N529-40. doi: 10.1088/0031-9155/54/23/N01.

12. Koenig SH, Brown RD, Spiller M, Lundbom N. Relaxometry of brain: Why white matter appears bright in MRI. Magn. Reson. Med. [Internet] 1990;14:482–495. doi: 10.1002/mrm.1910140306.

13. Koenig SH. Cholesterol of myelin is the determinant of gray-white contrast in MRI of brain. Magn. Reson. Med. [Internet] 1991;20:285–91. doi: 10.1002/mrm.1910200210.

14. Kalender W a. X-ray computed tomography. Phys. Med. Biol. [Internet] 2006;51:R29--43. doi: 10.1088/0031-9155/51/13/R03.

15. Goldman LW. Principles of CT and CT technology. J. Nucl. Med. Technol. [Internet] 2007;35:115-28-30. doi: 10.2967/jnmt.107.042978.

16. Zhu A, Shim H. Current Molecular Imaging Positron Emitting Radiotracers in Oncology. Nucl. Med. Mol. Imaging (2010). [Internet] 2011;45:1–14. doi: 10.1007/s13139-011-0075-y.

17. Gillings N. Radiotracers for positron emission tomography imaging. Magn. Reson.

Mater. Physics, Biol. Med. [Internet] 2013;26:149–158. doi: 10.1007/s10334-012-0356-1.

18. Tai YF, Piccini P. Applications of positron emission tomography (PET) in neurology. J. Neurol. Neurosurg. Psychiatry [Internet] 2004;75:669–76. doi: 10.1136/jnnp.2003.028175.

19. Alauddin MM. Positron emission tomography (PET) imaging with (18)F-based radiotracers. Am. J. Nucl. Med. Mol. Imaging [Internet] 2012;2:55–76.

20. Vallabhajosula S, Solnes L, Vallabhajosula B. A broad overview of positron emission tomography radiopharmaceuticals and clinical applications: What is new?; 2011 pp. 246–264. doi: 10.1053/j.semnuclmed.2011.02.003.

21. Nasrallah I, Dubroff J. An Overview of PET Neuroimaging. Semin. Nucl. Med. 2013;43:449–461. doi: 10.1053/j.semnuclmed.2013.06.003.

22. Kemp B. PET Physics and Instrumentation. In: PET-CT and PET-MRI in Oncology. Springer; 2012. pp. 3–17. doi: 10.1007/174_2011_526.

23. Taylor AJ, Salerno M, Dharmakumar R, Jerosch-Herold M. T1 Mapping Basic Techniques and Clinical Applications. JACC Cardiovasc. Imaging 2016;9:67–81. doi: 10.1016/j.jcmg.2015.11.005.

24. Borthakur A, Sochor M, Davatzikos C, Trojanowski JQ, Clark CM. T1?? MRI of Alzheimer's disease. Neuroimage 2008;41:1199–1205. doi: 10.1016/j.neuroimage.2008.03.030.

25. Dinse J, Waehnert M, Tardif CL, Schäfer A, Geyer S, Turner R, Bazin PL. A histology-based model of quantitative T1 contrast for in-vivo cortical parcellation of high-resolution 7 Tesla brain MR images. In: Lecture Notes in Computer Science (including subseries Lecture Notes in Artificial Intelligence and Lecture Notes in Bioinformatics). Vol. 8150 LNCS. ; 2013. pp. 51–58. doi: 10.1007/978-3-642-40763-5_7.

26. Morrison C, Henkelman RM. A model for magnetization transfer in tissues. Magn. Reson. Med. [Internet] 1995;33:475–482.

27. Van Zijl PCM, Yadav NN. Chemical exchange saturation transfer (CEST): What is in a name and what isn't? Magn. Reson. Med. 2011;65:927–948. doi: 10.1002/mrm.22761.

28. Gelman N, Ewing JR, Gorell JM, Spickler EM, Solomon EG. Interregional variation of longitudinal relaxation rates in human brain at 3.0 T: Relation to estimated iron and water contents. Magn. Reson. Med. [Internet] 2001;45:71–79. doi: 10.1002/1522-2594(200101)45:1<71::AID-MRM1011>3.0.CO;2-2.

29. Rooney WD, Johnson G, Li X, Cohen ER, Kim S-GG, Ugurbil K, Springer CS. Magnetic field and tissue dependencies of human brain longitudinal1H2O relaxation in vivo. Magn. Reson. Med. [Internet] 2007;57:308–318. doi: 10.1002/mrm.21122.

30. Schenck JF. Magnetic resonance imaging of brain iron. 2003. doi: 10.1016/S0022-510X(02)00431-8.

31. Caravan P, Ellison JJ, McMurry TJ, Lauffer RB. Gadolinium(III) Chelates as MRI Contrast Agents: Structure, Dynamics, and Applications. Chem. Rev. [Internet] 1999;99:2293–352. doi: 10.1021/cr980440x.

32. Wang Y-XJ. Superparamagnetic iron oxide based MRI contrast agents: Current status of clinical application. Quant. Imaging Med. Surg. [Internet] 2011;1:35–40. doi: 10.3978/j.issn.2223-4292.2011.08.03.

33. Rooney WD, Johnson G, Li X, Cohen ER, Kim S-GG, Ugurbil K, Springer CS. Magnetic field and tissue dependencies of human brain longitudinal 1H2O relaxation in vivo. Magn. Reson. Med. [Internet] 2007;57:308–318. doi: 10.1002/mrm.21122.

34. Nave K-A, Werner HB. Myelination of the Nervous System: Mechanisms and Functions. Annu. Rev. Cell Dev. Biol. [Internet] 2014;30:503–533. doi: 10.1146/annurev-cellbio-100913-013101.

35. Wilhelm MJ, Ong HH, Wehrli SL, Li C, Tsai P-H, Hackney DB, Wehrli FW. Direct magnetic resonance detection of myelin and prospects for quantitative imaging of myelin density. Proc. Natl. Acad. Sci. 2012;109:9605–9610. doi: 10.1073/pnas.1115107109.

36. Randall LO. CHEMICAL TOPOGRAPHY OF THE BRAIN. J. Biol. Chem. [Internet] 1938;124:481–488.

37. Deese AJ, Dratz EA, Hymel L, Fleischer S. Proton NMR T1, T2, and T1 rho relaxation studies of native and reconstituted sarcoplasmic reticulum and phospholipid vesicles. 1982. doi: 10.1016/S0006-3495(82)84670-5.

38. Ellena JF, Hutton WC, Cafiso DS. Elucidation of cross-relaxation pathways in phospholipid vesicles utilizing two-dimensional proton NMR spectroscopy. J. Am. Chem. Soc. [Internet] 1985;107:1530–1537. doi: 10.1021/ja00292a013.

39. Du J, Sheth V, He Q, Carl M, Chen J, Corey-Bloom J, Bydder GM. Measurement of T1 of the ultrashort T2&z.ast; components in white matter of the brain at 3T. PLoS One 2014;9. doi: 10.1371/journal.pone.0103296.

40. Stanisz GJ, Odrobina EE, Pun J, Escaravage M, Graham SJ, Bronskill MJ, Henkelman RM. T1, T2 relaxation and magnetization transfer in tissue at 3T. Magn. Reson. Med. [Internet] 2005;54:507–512. doi: 10.1002/mrm.20605.

41. Henkelman RM, Stanisz GJ, Graham SJ. Magnetization transfer in MRI: A review. NMR Biomed. 2001;14:57–64. doi: 10.1002/nbm.683.

42. Liu G, Song X, Chan KWY, Mcmahon MT. Nuts and bolts of chemical exchange saturation transfer MRI. NMR Biomed. 2013;26:810–828. doi: 10.1002/nbm.2899.

43. Edzes HT, Samulski ET. Cross relaxation and spin diffusion in the proton NMR of hydrated collagen. Nature [Internet] 1977;265:521–523.

44. Gochberg DF, Gore JC. Quantitative imaging of magnetization transfer using an inversion recovery sequence. Magn. Reson. Med. [Internet] 2003;49:501–505. doi: 10.1002/mrm.10386.

45. Dortch RD, Moore J, Li K, Jankiewicz M, Gochberg DF, Hirtle JA, Gore JC, Smith SA. Quantitative magnetization transfer imaging of human brain at 7T. Neuroimage 2013;64:640–649. doi: 10.1016/j.neuroimage.2012.08.047.

46. Zimmerman JR, Brittin WE. Nuclear Magnetic Resonance Studies in Multiple Phase Systems: Lifetime of a Water Molecule in an Adsorbing Phase on Silica Gel. J. Phys. Chem. [Internet] 1957;61:1328–1333. doi: 10.1021/j150556a015.

47. Gochberg DF, Kennan RP, Gore JC. Quantitative studies of magnetization transfer by selective excitation andT1 recovery. Magn. Reson. Med. [Internet] 1997;38:224–231. doi: 10.1002/mrm.1910380210.

48. Prantner AM, Bretthorst GL, Neil JJ, Garbow JR, Ackerman JJH. Magnetization transfer induced biexponential longitudinal relaxation. Magn. Reson. Med. 2008;60:555–563. doi: 10.1002/mrm.21671.

49. Labadie C, Lee JH, Rooney WD, Jarchow S, Aubert-Frécon M, Springer CS, Möller

HE. Myelin water mapping by spatially regularized longitudinal relaxographic imaging at high magnetic fields. Magn. Reson. Med. 2014;71:375–387. doi: 10.1002/mrm.24670.

50. Gochberg DF, Gore JC. Quantitative magnetization transfer imaging via selective inversion recovery with short repetition times. Magn. Reson. Med. 2007;57:437–441. doi: 10.1002/mrm.21143.

51. Stikov N, Boudreau M, Levesque IR, Tardif CL, Barral JK, Pike GB. On the accuracy of T1 mapping: Searching for common ground. Magn. Reson. Med. 2015;73:514–522. doi: 10.1002/mrm.25135.

52. Kingsley PB, Ogg RJ, Reddick WE, Steen RGG. Correction of errors caused by imperfect inversion pulses in MR imaging measurement of T1 relaxation times. Magn. Reson. Imaging 1998;16:1049–1055. doi: 10.1016/S0730-725X(98)00112-X.

53. Barral JK, Gudmundson E, Stikov N, Etezadi-Amoli M, Stoica P, Nishimura DG. A robust methodology for in vivo T1 mapping. Magn. Reson. Med. 2010;64:1057–1067. doi: 10.1002/mrm.22497.

54. Henkelman RM, Huang X, Xiang Q-SS, Stanisz GJ, Swanson SD, Bronskill MJ. Quantitative interpretation of magnetization transfer. Magn Reson Med [Internet] 1993;29:759–766. doi: 10.1002/mrm.1910290607.

55. Mougin OE, Coxon RC, Pitiot a, Gowland P a. Magnetization transfer phenomenon in the human brain at 7 T. Neuroimage [Internet] 2010;49:272–81. doi: 10.1016/j.neuroimage.2009.08.022.

56. Chan SI, Feigenson GW, Serter CHA. Nuclear Relaxation Studies of Lecithin Bilayers. Nature [Internet] 1971;231:110–112.

57. Finer EG, Darke A. Phospholipid hydration studied by deuteron magnetic resonance spectroscopy. Chem. Phys. Lipids 1974;12:1–16. doi: 10.1016/0009-3084(74)90064-4.

58. Ramani A, Aliev AE, Barkera GJ, Tofts PS. Another approach to protons with constricted mobility in white matter: Pilot studies using wideline and high-resolution NMR spectroscopy. Magn. Reson. Imaging 2003;21:1039–1043. doi: 10.1016/S0730-725X(03)00207-8.

59. Horch RA, Gore JC, Does MD. Origins of the ultrashort-T2 1H NMR signals in myelinated nerve: A direct measure of myelin content? Magn. Reson. Med. [Internet] 2011;66:24–31. doi: 10.1002/mrm.22980.

60. Malyarenko DI, Zimmermann EM, Adler J, Swanson SD. Magnetization transfer in lamellar liquid crystals. Magn. Reson. Med. [Internet] 2013;72:1427–1434. doi: 10.1002/mrm.25034.

61. Langkammer C, Schweser F, Krebs N, et al. Quantitative susceptibility mapping (QSM) as a means to measure brain iron? A post mortem validation study. Neuroimage 2012;62:1593–1599. doi: 10.1016/j.neuroimage.2012.05.049.

62. Deistung A, Schäfer A, Schweser F, Biedermann U, Turner R, Reichenbach JR. Toward in vivo histology: A comparison of quantitative susceptibility mapping (QSM) with magnitude-, phase-, and R2*-imaging at ultra-high magnetic field strength. Neuroimage 2013;65:299–314. doi: 10.1016/j.neuroimage.2012.09.055.

63. Sled JG, Pike GB, Bruce Pike G. Quantitative imaging of magnetization transfer exchange and relaxation properties in vivo using MRI. Magn. Reson. Med. [Internet] 2001;46:923–931. doi: 10.1002/mrm.1278.

64. Sinclair CDJ, Samson RS, Thomas DL, Weiskopf N, Lutti A, Thornton JS, Golay X. Quantitative magnetization transfer in in vivo healthy human skeletal muscle at 3 T. Magn. Reson. Med. 2010;64:1739–1748. doi: 10.1002/mrm.22562.

65. Li JG, Graham SJ, Henkelman RM. A flexible magnetization transfer line shape derived from tissue experimental data. Magn. Reson. Med. 1997;37:866–871. doi: 10.1002/mrm.1910370610.

66. Hua J, Jones CK, Blakeley J, Smith SA, van Zijl PCM, Zhou J. Quantitative description of the asymmetry in magnetization transfer effects around the water resonance in the human brain. Magn. Reson. Med. [Internet] 2007;58:786–793. doi: 10.1002/mrm.21387.

67. Pekar J, Jezzard P, Roberts DA, Leigh JS, Frank JA, McLaughlin AGC. Perfusion imaging with compensation for asymmetric magnetization transfer effects. Magn. Reson. Med. [Internet] 1996;35:70–79. doi: 10.1002/mrm.1910350110.

68. Ng MC, Hua J, Hu Y, Luk KD, Lam EY. Magnetization transfer (MT) asymmetry around the water resonance in human cervical spinal cord. J. Magn. Reson. Imaging 2009;29:523–528. doi: 10.1002/jmri.21610.

69. Swanson SD, Pang Y. MT is Symmetric but Shifted with Respect to Water. Proc. Intl. Soc. Mag. Reson. Med. 2003;11:660.

70. Morrison C, Stanisz G, Henkelman RM. Modeling magnetization transfer for biological-like systems using a semi-solid pool with a super-Lorentzian lineshape and dipolar reservoir. J Magn Reson B [Internet] 1995;108:103–113. doi: 10.1006/jmrb.1995.1111.

71. MacKay A, Laule C, Vavasour I, Bjarnason T, Kolind S, Mädler B. Insights into brain microstructure from the T2 distribution. Magn. Reson. Imaging 2006;24:515–525. doi: 10.1016/j.mri.2005.12.037.

72. Sati P, van Gelderen P, Silva AC, Reich DS, Merkle H, de Zwart JA, Duyn JH. Micro-compartment specific T2 relaxation in the brain. Neuroimage 2013;77:268–278. doi: 10.1016/j.neuroimage.2013.03.005.

73. Levesque IR, Pike GB. Characterizing healthy and diseased white matter using quantitative magnetization transfer and multicomponent T2 relaxometry: A unified view via a four-pool model. Magn. Reson. Med. 2009;62:1487–1496. doi: 10.1002/mrm.22131.

74. Kalantari S, Laule C, Bjarnason TA, Vavasour IM, MacKay AL. Insight into in vivo magnetization exchange in human white matter regions. Magn. Reson. Med. [Internet] 2011;66:1142–1151. doi: 10.1002/mrm.22873.

75. Stanisz GJ, Kecojevic A, Bronskill MJ, Henkelman RM. Characterizing white matter with magnetization transfer and T2. Magn. Reson. Med. 1999;42:1128–1136. doi: 10.1002/(SICI)1522-2594(199912)42:6<1128::AID-MRM18>3.0.CO;2-9.

76. Forsén S, Hoffman R. Study of moderately rapid chemical exchange reactions by means of nuclear magnetic double resonance. J. Chem. Phys. [Internet] 2004;39:2892–2901. doi: 10.1063/1.1734121.

77. Gochberg DF, Kennan RP, Robson MD, Gore JC. Quantitative imaging of magnetization transfer using multiple selective pulses. Magn Reson Med [Internet] 1999;41:1065–1072. doi: 10.1002/(SICI)1522-2594(199905)41:5<1065::AID-MRM27>3.0.CO;2-9 [pii].

78. Adisetiyo V, Jensen JH, Ramani A, Tabesh A, Di Martino A, Fieremans E,

Castellanos FX, Helpern JA. In vivo assessment of age-related brain iron differences by magnetic field correlation imaging. J. Magn. Reson. Imaging 2012;36:322–331. doi: 10.1002/jmri.23631.

79. Hallgren B, Sourander P. The Effect of Age on the Non-Haemin Iron in the Human Brain. J. Neurochem. [Internet] 1958;3:41–51. doi: 10.1111/j.1471-4159.1958.tb12607.x.

80. Fatouros PP, Marmarou A, Physics R. Use of magnetic resonance imaging for in vivo measurements of water content in human brain: method and normal values. J. Neurosurg. [Internet] 1999;90:109–115. doi: 10.3171/jns.1999.90.1.0109.

81. Volz S, Nöth U, Jurcoane A, Ziemann U, Hattingen E, Deichmann R. Quantitative proton density mapping: correcting the receiver sensitivity bias via pseudo proton densities. Neuroimage 2012;63:540–552. doi: 10.1016/j.neuroimage.2012.06.076.

82. Abbas Z, Gras V, Möllenhoff K, Oros-Peusquens A-M, Shah NJ. Quantitative water content mapping at clinically relevant field strengths: a comparative study at 1.5 T and 3 T. Neuroimage [Internet] 2015;106:404–413. doi: 10.1016/j.neuroimage.2014.11.017.

83. O'Brien JS, Sampson EL. Lipid composition of the normal human brain: gray matter, white matter, and myelin. J. Lipid Res. [Internet] 1965;6:537–44.

84. MacKay AL, Vavasour IM, Rauscher A, Kolind SH, Mädler B, Moore GRW, Traboulsee AL, Li DKB, Laule C. MR Relaxation in Multiple Sclerosis. Neuroimaging Clin. N. Am. 2009;19:1–26. doi: 10.1016/j.nic.2008.09.007.

85. Dortch RD, Harkins KD, Juttukonda MR, Gore JC, Does MD. Characterizing inter-compartmental water exchange in myelinated tissue using relaxation exchange spectroscopy. Magn. Reson. Med. [Internet] 2013;70:1450–1459. doi: 10.1002/mrm.24571.

86. Laule C, Vavasour IM, Kolind SH, Li DKB, Traboulsee TL, Moore GRW, MacKay AL. Magnetic Resonance Imaging of Myelin. Neurotherapeutics 2007;4:460–484. doi: 10.1016/j.nurt.2007.05.004.

87. Fatouros PP, Marmarou A, Kraft KA, Inao S, Schwarz FP. In Vivo Brain Water Determination byT1 Measurements: Effect of Total Water Content, Hydration Fraction, and Field Strength. Magn. Reson. Med. [Internet] 1991;17:402–413. doi: 10.1002/mrm.1910170212.

88. Kamman RL, Go KG, Brouwer W, Berendsen HJC. Nuclear magnetic resonance relaxation in experimental brain edema: Effects of water concentration, protein concentration, and temperature. Magn. Reson. Med. [Internet] 1988;6:265–274. doi: 10.1002/mrm.1910060304.

89. Wolff SD, Balaban RS. Magnetization transfer contrast (MTC) and tissue water proton relaxationin vivo. Magn. Reson. Med. [Internet] 1989;10:135–144. doi: 10.1002/mrm.1910100113.

90. Yarnykh VL, Yuan C. Cross-relaxation imaging reveals detailed anatomy of white matter fiber tracts in the human brain. Neuroimage [Internet] 2004;23:409–24. doi: 10.1016/j.neuroimage.2004.04.029.

91. Dortch RD, Li K, Gochberg DF, Welch EB, Dula AN, Tamhane AA, Gore JC, Smith SA. Quantitative magnetization transfer imaging in human brain at 3 T via selective inversion recovery. Magn. Reson. Med. [Internet] 2011;66:1346–1352. doi: 10.1002/mrm.22928.

92. Tozer DJ, Rees JH, Benton CE, Waldman AD, Jäger HR, Tofts PS. Quantitative magnetisation transfer imaging in glioma: Preliminary results. NMR Biomed. 2011;24:492–498. doi: 10.1002/nbm.1614.

93. Yarnykh VL, Bowen JD, Samsonov A, Repovic P, Mayadev A, Qian P, Gangadharan B, Keogh BP, Maravilla KR, Jung Henson LK. Fast whole-brain three-dimensional macromolecular proton fraction mapping in multiple sclerosis. Radiology [Internet] 2015;274:210–20. doi: 10.1148/radiol.14140528.

94. Davies GR, Tozer DJ, Cercignani M, Ramani a, Dalton CM, Thompson a J, Barker GJ, Tofts PS, Miller DH. Estimation of the macromolecular proton fraction and bound pool T2 in multiple sclerosis. Mult. Scler. [Internet] 2004;10:607–13. doi: 10.1191/1352458504ms1105oa.

95. Underhill HR, Rostomily RC, Mikheev AM, Yuan C, Yarnykh VL. Fast bound pool fraction imaging of the in vivo rat brain: Association with myelin content and validation in the C6 glioma model. Neuroimage 2011;54:2052–2065. doi: 10.1016/j.neuroimage.2010.10.065.

96. Sobol WT, Cameron IG, Inch WR, Pintar MM. Modeling of proton spin relaxation in muscle tissue using nuclear magnetic resonance spin grouping and exchange analysis. Biophys. J. [Internet] 1986;50:181–191. doi: 10.1016/S0006-3495(86)83450-6.

97. Morris GA, Freemont AJ. Direct Observation of the Magnetization Exchange Dynamics Responsible for Magnetization Transfer Contrast in Human Cartilagein Vitro. Magn. Reson. Med. [Internet] 1992;28:97–104. doi: 10.1002/mrm.1910280110.

98. Goldman M, Shen L. Spin-spin relaxation in LaF3. Phys. Rev. 1966;144:321–331. doi: 10.1103/PhysRev.144.321.

99. Soellinger M, Langkammer C, Seifert-Held T, Fazekas F, Ropele S. Fast bound pool fraction mapping using stimulated echoes. Magn. Reson. Med. [Internet] 2011;66:717–724. doi: 10.1002/mrm.22846.

100. HU BS, CONOLLY SM, WRIGHT GA, Nishimura DG, Macovski A. Pulsed saturation transfer contrast. Magn. Reson. Med. [Internet] 1992;26:231–240. doi: 10.1002/mrm.1910260205.

101. Lattanzio P-JJ, Marshall KW, Damyanovich AZ, Peemoeller H. Macromolecule and water magnetization exchange modeling in articular cartilage. Magn. Reson. Med. [Internet] 2000;44:840–851. doi: 10.1002/1522-2594(200012)44:6<840::AID-MRM4>3.0.CO;2-K.

102. Pampel A, Müller DK, Anwander A, Marschner H, Möller HE. Orientation dependence of magnetization transfer parameters in human white matter. Neuroimage 2015;114:136–146. doi: 10.1016/j.neuroimage.2015.03.068.

103. Ordidge RJ, Gibbs P, Chapman B, Stehling MK, Mansfield P. High-speed multislice T_1 mapping using inversion-recovery echo-planar imaging. Magn. Reson. Med. [Internet] 1990;16:238–245. doi: 10.1002/mrm.1910160205.

104. Tannús A, Garwood M, Tannus A, Garwood M. Adiabatic pulses. In: NMR in Biomedicine. Vol. 10. ; 1997. pp. 423–434. doi: 10.1002/(SICI)1099-1492(199712)10:8<423::AID-NBM488>3.0.CO;2-X.

105. Helms G, Hagberg GE. Quantification of magnetization transfer by sampling the transient signal using MT-prepared single-shot EPI. Concepts Magn. Reson. [Internet] 2003;19A:149–152. doi: 10.1002/cmr.a.10093.

106. Bos A van den. Application of statistical parameter estimation methods to physical

measurements. J. Phys. E. [Internet] 1977;10:753. doi: 10.1088/0022-3735/10/8/001.

107. Waldman A, Rees JH, Brock CS, Robson MD, Gatehouse PD, Bydder GM. MRI of the brain with ultra-short echo-time pulse sequences. Neuroradiology 2003;45:887–892. doi: 10.1007/s00234-003-1076-z.

108. Du J, Ma G, Li S, Carl M, Szeverenyi NM, VandenBerg S, Corey-Bloom J, Bydder GM. Ultrashort echo time (UTE) magnetic resonance imaging of the short T2 components in white matter of the brain using a clinical 3T scanner. Neuroimage 2014;87:32–41. doi: 10.1016/j.neuroimage.2013.10.053.

109. Sled JGJG, Levesque I, Santos ACC, Francis SJJ, Narayanan S, Brass SDD, Arnold DLL, Pike GBB. Regional Variations in Normal Brain Shown by Quantitative Magnetization Transfer Imaging. Magn. Reson. Med. [Internet] 2004;51:299–303. doi: 10.1002/mrm.10701.

110. Underhill HR, Yuan C, Yarnykh VL. Direct quantitative comparison between cross-relaxation imaging and diffusion tensor imaging of the human brain at 3.0 T. Neuroimage 2009;47:1568–1578. doi: 10.1016/j.neuroimage.2009.05.075.

111. Feigenson GW, Chan SI. Nuclear magnetic relaxation behavior of lecithin multilayers. J. Am. Chem. Soc. [Internet] 1974;96:1312–1319. doi: 10.1021/ja00812a009.

112. Haacke EM, Cheng NYC, House MJ, Liu Q, Neelavalli J, Ogg RJ, Khan A, Ayaz M, Kirsch W, Obenaus A. Imaging iron stores in the brain using magnetic resonance imaging. Magn. Reson. Imaging 2005;23:1–25. doi: 10.1016/j.mri.2004.10.001.

113. Samsonov A, Alexander AL, Mossahebi P, Wu Y-CC, Duncan ID, Field AS. Quantitative MR imaging of two-pool magnetization transfer model parameters in myelin mutant shaking pup. Neuroimage 2012;62:1390–1398. doi: 10.1016/j.neuroimage.2012.05.077.

114. Clark VP, Courchesne E, Grafe M. In vivo myeloarchitectonic analysis of human striate and extrastriate cortex using magnetic resonance imaging. Cereb. Cortex 1992;2:417–424.

115. Constable RT, Smith RC, Gore JC. Signal-to-noise and contrast in fast spin echo (FSE) and inversion recovery FSE imaging. J. Comput. Assist. Tomogr. [Internet] 1992;16:41–7.

116. Smith RC, Constable RT, Reinhold C, McCauley T, Lange RC, McCarthy S. Fast spin echo STIR imaging. J. Comput. Assist. Tomogr. 1994;18:209–213.

117. Zhu DC, Penn RD. Full-brain T1 mapping through inversion recovery fast spin echo imaging with time-efficient slice ordering. Magn. Reson. Med. 2005;54:725–731. doi: 10.1002/mrm.20602.

118. Barazany D, Assaf Y. Visualization of cortical lamination patterns with magnetic resonance imaging. Cereb. Cortex 2012;22:2016–2023. doi: 10.1093/cercor/bhr277.

119. Stüber C, Morawski M, Schäfer A, et al. Myelin and iron concentration in the human brain: A quantitative study of MRI contrast. Neuroimage 2014;93:95–106. doi: 10.1016/j.neuroimage.2014.02.026.

120. Duyn J, de Zwart J, van Gelderen P, Koretsky A. A Simple B1 Correction Method for High Resolution Neuroimaging. In: Proceedings 14th Scientific Meeting, International Society for Magnetic Resonance in Medicine. ; 2006. p. 2355.

121. Deoni SCL, Rutt BK, Arun T, Pierpaoli C, Jones DK. Gleaning multicomponent T1 and T2 information from steady-state imaging data. Magn. Reson. Med.

2008;60:1372–1387. doi: 10.1002/mrm.21704.

122. Dinse J, Härtwich N, Waehnert MD, Tardif CL, Schäfer A, Geyer S, Preim B, Turner R, Bazin P-L. A cytoarchitecture-driven myelin model reveals area-specific signatures in human primary and secondary areas using ultra-high resolution in-vivo brain MRI. Neuroimage 2015;114:71–87. doi: 10.1016/j.neuroimage.2015.04.023.

123. Mezer A, Yeatman JD, Stikov N, et al. Quantifying the local tissue volume and composition in individual brains with magnetic resonance imaging. Nat Med [Internet] 2013;19:1667–1672.

124. Callaghan MF, Helms G, Lutti A, Mohammadi S, Weiskopf N. A general linear relaxometry model of R 1 using imaging data. Magn. Reson. Med. [Internet] 2015;73:1309–1314. doi: 10.1002/mrm.25210.

125. Ordidge RJ, Gibbs P, Chapman B, Stehling MK, Mansfield P. High-speed multislice T1 mapping using inversion-recovery echo-planar imaging. Magn. Reson. Med. 1990;16:238–245. doi: 10.1002/mrm.1910160205.

126. Volz S, Nöth U, Deichmann R. Correction of systematic errors in quantitative proton density mapping. Magn. Reson. Med. 2012;68:74–85. doi: 10.1002/mrm.23206.

127. Cornell BA, Pope JM, Troup GJF. A pulsed N.M.R. study of D2O bound to 1,2 dipalmitoyl phosphatidylcholine. Chem. Phys. Lipids 1974;13:183–201. doi: 10.1016/0009-3084(74)90035-8.

128. Schuh JR, Banerjee U, Müller L, Chan SI. The phospholipid packing arrangement in small bilayer vesicles as revealed by proton magnetic resonance studies at 500 MHz. Biochim. Biophys. Acta - Biomembr. 1982;687:219–225. doi: 10.1016/0005-2736(82)90549-1.

129. Rioux JA, Levesque IR, Rutt BK. Biexponential longitudinal relaxation in white matter: Characterization and impact on T1 mapping with IR-FSE and MP2RAGE. Magn. Reson. Med. 2016;75:2265–2277. doi: 10.1002/mrm.25729.

130. Zhang J, Kolind SH, Laule C, MacKay AL. How does magnetization transfer influence mcDESPOT results? Magn. Reson. Med. 2015;74:1327–1335. doi: 10.1002/mrm.25520.

131. Redpath TW, Smith FW. Technical note: Use of a double inversion recovery pulse sequence to image selectively grey or white brain matter. Br. J. Radiol. 1994;67:1258–1263. doi: 10.1259/0007-1285-67-804-1258.

132. Oh S-HH, Bilello M, Schindler M, Markowitz CE, Detre JA, Lee J. Direct visualization of short transverse relaxation time component (ViSTa). Neuroimage 2013;83:485–492. doi: 10.1016/j.neuroimage.2013.06.047.

133. Forster J, Schick F, Pfeffer M, Lutz O. Magnetization transfer by simple sequences of rectangular pulses. Magma Magn. Reson. Mater. Physics, Biol. Med. 1995;3:83–93. doi: 10.1007/BF01709851.

134. Graham SJ, Henkelman RM. Understanding pulsed magnetization transfer. J. Magn. Reson. Imaging 1997;7:903–912. doi: 10.1002/jmri.1880070520.

135. Ramani A, Dalton C, Miller DH, Tofts PS, Barker GJ. Precise estimate of fundamental in-vivo MT parameters in human brain in clinically feasible times. Magn. Reson. Imaging [Internet] 2002;20:721–731. doi: 10.1016/S0730-725X(02)00598-2.

136. Yarnykh VL. Pulsed Z-spectroscopic imaging of cross-relaxation parameters in tissues for human MRI: Theory and clinical applications. Magn. Reson. Med.

[Internet] 2002;47:929–939. doi: 10.1002/mrm.10120.

137. Scheidegger R, Vinogradov E, Alsop DC. Amide proton transfer imaging with improved robustness to magnetic field inhomogeneity and magnetization transfer asymmetry using saturation with frequency alternating RF irradiation. Magn. Reson. Med. 2011;66:1275–1285. doi: 10.1002/mrm.22912.

138. Lee JS, Regatte RR, Jerschow A. Isolating chemical exchange saturation transfer contrast from magnetization transfer asymmetry under two-frequency rf irradiation. J. Magn. Reson. 2011;215:56–63. doi: 10.1016/j.jmr.2011.12.012.

139. Dixon WT, Ren J, Lubag AJM, Ratnakar J, Vinogradov E, Hancu I, Lenkinski RE, Sherry AD. A concentration-independent method to measure exchange rates in PARACEST agents. Magn. Reson. Med. 2010;63:625–632. doi: 10.1002/mrm.22242.

140. Yang QX, Wang J, Zhang X, Collins CM, Smith MB, Liu H, Zhu XH, Vaughan JT, Ugurbil K, Chen W. Analysis of wave behavior in lossy dielectric samples at high field. Magn. Reson. Med. 2002;47:982–989. doi: 10.1002/mrm.10137.

141. Collins CM, Smith MB, Turner R. Model of local temperature changes in brain upon functional activation. J. Appl. Physiol. [Internet] 2004;97:2051–5. doi: 10.1152/japplphysiol.00626.2004.

142. Wolff SD, Balaban RS. Assessing contrast on MR images. Radiology 1997;202:25–9. doi: 10.1148/radiology.202.1.8988186.

143. Levesque IR, Giacomini PS, Narayanan S, Ribeiro LT, Sled JG, Arnold DL, Pike GB. Quantitative magnetization transfer and myelin water imaging of the evolution of acute multiple sclerosis lesions. Magn. Reson. Med. 2010;63:633–640. doi: 10.1002/mrm.22244.

144. Love S. Demyelinating diseases. J. Clin. Pathol. 2006;59:1151–1159. doi: 10.1136/jcp.2005.031195.

145. Alizadeh A, Dyck SM, Karimi-Abdolrezaee S. Myelin damage and repair in pathologic CNS: challenges and prospects. Front. Mol. Neurosci. [Internet] 2015;8:35. doi: 10.3389/fnmol.2015.00035.

146. Popescu BF, Lucchinetti CF. Pathology of demyelinating diseases. Annu Rev Pathol [Internet] 2012;7:185–217. doi: 10.1146/annurev-pathol-011811-132443.

147. Van Zijl PCM, Zhou J, Mori N, Payen JF, Wilson D, Mori S. Mechanism of magnetization transfer during on-resonance water saturation. A new approach to detect mobile proteins, peptides, and lipids. Magn. Reson. Med. 2003;49:440–449. doi: 10.1002/mrm.10398.

148. Chen JH, Sambol EB, DeCarolis P, O'Connor R, Geha RC, Wu Y V., Singer S. High-resolution MAS NMR spectroscopy detection of the spin magnetization exchange by cross-relaxation and chemical exchange in intact cell lines and human tissue specimens. Magn. Reson. Med. 2006;55:1246–1256. doi: 10.1002/mrm.20889.

149. Liepinsh E, Otting G. Proton exchange rates from amino acid side chains-- implications for image contrast. Magn. Reson. Med. 1996;35:30–42. doi: 10.1002/mrm.1910350106.

150. Zhou J, Zijl PCM van. Chemical exchange saturation transfer imaging and spectroscopy. Prog. Nucl. Magn. Reson. Spectrosc. 2006;48:109–136. doi: 10.1016/j.pnmrs.2006.01.001.

151. Kim M, Gillen J, Landman BA, Zhou J, Van Zijl PCM. Water saturation shift referencing (WASSR) for chemical exchange saturation transfer (CEST) experiments.

Magn. Reson. Med. 2009;61:1441–1450. doi: 10.1002/mrm.21873.

152. Charvolin J, Rigny P. Pulsed NMR in dynamically heterogeneous systems. J. Magn. Reson. 1971;4:40–46. doi: 10.1016/0022-2364(71)90022-9.

153. Wennerstrom H. Proton nuclear magnetic resonance lineshapes in lamellar liquid crystals. Chem. Phys. Lett. 1973;18:41–44. doi: 10.1016/0009-2614(73)80333-1.

154. Yadav NN, Chan KWY, Jones CK, McMahon MT, Van Zijl PCM. Time domain removal of irrelevant magnetization in chemical exchange saturation transfer Z-spectra. Magn. Reson. Med. 2013;70:547–555. doi: 10.1002/mrm.24812.

155. Zaiss M, Schmitt B, Bachert P. Quantitative separation of CEST effect from magnetization transfer and spillover effects by Lorentzian-line-fit analysis of z-spectra. J. Magn. Reson. 2011;211:149–155. doi: 10.1016/j.jmr.2011.05.001.

156. Yang QX, Wang J, Collins CM, Smith MB, Zhang X, Ugurbil K, Chen W. Phantom design method for high-field MRI human systems. Magn. Reson. Med. 2004;52:1016–1020. doi: 10.1002/mrm.20245.

157. Gelman N, Gorell JM, Barker PB, Savage RM, Spickler EM, Windham JP, Knight R a. MR imaging of human brain at 3.0 T: preliminary report on transverse relaxation rates and relation to estimated iron content. Radiology [Internet] 1999;210:759–767. doi: 10.1148/radiology.210.3.r99fe41759.

158. Martin WRW, Wieler M, Gee M. Midbrain iron content in early Parkinson disease: A potential biomarker of disease status. Neurology 2008;70:1411–1417. doi: 10.1212/01.wnl.0000286384.31050.b5.

159. Langkammer C, Krebs N, Goessler W, Scheurer E, Ebner F, Yen K, Fazekas F, Ropele S. Quantitative MR Imaging of Brain Iron : A Postmortem Validation Study. Radiology [Internet] 2010;257:455–462. doi: 10.1148/radiol.10100495.

160. Ward RJ, Zucca FA, Duyn JH, Crichton RR, Zecca L. The role of iron in brain ageing and neurodegenerative disorders. Lancet Neurol. 2014;13:1045–1060. doi: 10.1016/S1474-4422(14)70117-6.

Appendix: Curriculum Vitae

EDUCATION
- **B.S.** in Applied Physics   2005.08–2009.06
  - ➤ **Huazhong University of Science and Technology**
- **M.S.** in Physics   2010.08–2012.05
  - ➤ **University of Maryland-College Park**
- **Ph.D.** in Physics   2010.08–2016.12
  - ➤ **University of Maryland-College Park**
  - ➤ **Advanced MRI Section, LFMI, NINDS, NIH**

PUBLICATIONS
- van Gelderen, P., Jiang, X., Duyn, J.H., 2015. Effects of magnetization transfer on T_1 contrast in human brain white matter. Neuroimage 128, 85–95. doi:10.1016/j.neuroimage.2015.12.032
- van Gelderen, P., Jiang, X., Duyn, J.H., 2016. Rapid measurement of brain macromolecular proton fraction with transient saturation transfer MRI. Magn. Reson. Med. n/a--n/a. doi:10.1002/mrm.26304
- Jiang, X., van Gelderen, P., Duyn, J.H., Spectral characteristics of semi-solid protons in human brain white matter at 7 T, accepted for publication in Magn. Reson. Med.

CONFERENCE ABSTRACTS
- Jiang, X., van Gelderen, P., de Zwart, J. A, Duyn, J.H., 2014. Indirect MRI Detection of Myelin Water Based on Water Exchange Properties, in: ISMRM 22nd Annual Meeting. p. 3208.
- Jiang, X., van Gelderen, P., de Zwart, J. A, Duyn, J.H., 2014. Selective Myelin Water Suppression by Direct Saturation, in: ISMRM 22nd Annual Meeting. p. 3374.
- van Gelderen, P., Jiang, X., de Zwart, J. A, Duyn, J.H., 2014. T_1 Measurement of the Myelin Water Fraction, in: ISMRM 22nd Annual Meeting. p. 367.
- Jiang, X., van Gelderen, P., Li, X., Leibovitch, E., Sati, P., Silva, A.C., Duyn, J.H., 2015. Study of Bound Proton T_2 and Magnetization Transfer using Pulsed MT, in: ISMRM 23rd Annual Meeting. p. 5530.
- van Gelderen, P., Jiang, X., Duyn, J.H., 2015. Dependence of the apparent T_1 on Magnetization Transfer, in: ISMRM 23rd Annual Meeting. p. 15.
- van Gelderen, P., Jiang, X., Duyn, J.H., 2015. Exploring a Flexible Pulse Design for Studying Magnetization Transfer, in: ISMRM 23rd Annual Meeting. p. 996.
- Jiang, X., van Gelderen, P., Duyn, J.H., 2016. Measurement of the Resonance Frequency of Macromolecular Protons in Brain, in: ISMRM 24th Annual Meeting. p. 1502.

RESEARCH EXPERIENCE
- **Predoctoral visiting fellow, AMRI, LFMI, NINDS, NIH**   2013.07-2016.12
  - Advisor: Jeff Duyn, Peter van Gelderen
- **Visiting Student, Prof. Nicholas Fang Research Group, ME, MIT**   2012.08-2012.12
  - Advisor: Nicholas Fang

TEACHING EXPERIENCE
Teaching Assistant, PHYS410 Classical Mechanics, UMCP   2013.01-2013.05
Teaching Assistant, PHYS141 Principles of Physics, UMCP   2013.05-2013.07